Quantitative MRI of the human brain: magnetisation transfer and magnetic field mapping

Mara Cercignani

A thesis submitted to the University College London for the degree of

Doctor of Philosophy

July 2006

NMR Research Unit
Department of Neuroinflammation
Institute of Neurology
University College London
Queen Square
London WC1N 3BG
United Kingdom

ProQuest LLC
789 East Eisenhower Parkway
P.O. Box 1346
Ann Arbor, MI 48106-1346

Abstract

The ultimate goal of this thesis was to identify ways of combining the parametric maps produced by the use of multiple quantitative Magnetic Resonance Imaging (MRI) techniques. As a first stage towards this goal, this thesis focuses on magnetisation transfer (MT) imaging, and on the use of field mapping techniques to improve the reliability of other quantitative techniques such as functional MRI (fMRI) and diffusion tensor (DT) MRI.

After summarising the basic principles of MRI, the MT phenomenon is described and a quantitative MT model is reviewed.

A set of experiments is then described aiming at optimising the acquisition parameters for the measurement of the MT ratio (MTR). The interaction between T_1 and MT is investigated, confirming that MTR acquisition protocols should be designed to minimize T_1-weighting. Next, the quantitative model of MT is used to optimise the white-to-grey matter contrast to noise ratio of a pulse sequence for MTR measurement, at both 1.5 T and 3.0 T.

The following chapter is focused on the optimisation of quantitative MT for *in vivo* applications. First, the sensitivity to noise of the technique is investigated using simulations. Second, the implementation of a 3D pulse sequence for quantitative MT is described. The sequence is used at 1.5 T and at 3.0 T to collect data from healthy volunteers, providing normative values. Finally, the set of sampling points used to measure MT parameters is optimised using the Cramer-Rao lower bound, showing dramatic improvements in both precision and accuracy.

Next, after a review of static field inhomogeneities and field mapping, the consequences of field inhomogeneities on quantitative MT are evaluated. The use of novel acquisition sequences for field mapping is investigated, the application of field-map based correction for fMRI and DT MRI data is considered, and its effects are discussed.

Finally, an attempt to combine different parameters through multivariate analysis is presented, by using principal component analysis to identify patterns of association between MT parameters.

Acknowledgements

First and foremost, I have to thank Maria Ron, who has been a wonderful boss and has always supported me, and given me her precious advice in several occasions. My subsidiary supervisor, Mark Symms, not only gave me an invaluable help, but also volunteered for most of the experiments described in this thesis.

The person who convinced me to come to the IoN, to whom I will be forever grateful, is Gareth Barker. I am not sure he realised what he was doing when he talked to me about this job, at a wedding reception in Norfolk. Since then, he has always helped and supported me, even after I convinced him to take up rollerblading.

I would like to thank also all the physicists at the IoN, for the useful discussion and for the trips to the pub: Claudia Wheeler-Kingshott, Phil Boulby, Dan Tozer, Mary McLean, and Paul Tofts.

Thanks also to Danny Alexander, for his help with the quantitative MT optimisation, described in Chapter 4.

A special thank you goes to Gary and Stefania, who never complained when I neglected their projects to concentrate on this thesis.

Thanks to all the radiographers and the clinical fellows at the NMR Research Unit, and at Chalfont, for their help and for their spirit.

Finally, I am grateful to the Wellcome Trust for funding.

Publications associated with this thesis

Full papers

Cercignani M, Symms MR, Schmierer K, Boulby PA, Tozer DJ, Ron M, Tofts PS, Barker GJ. Three-dimensional quantitative magnetisation transfer imaging of the human brain. *Neuroimage* 2005; 27: 436-41.

Cercignani M, Symms MR, Ron M, Barker GJ. 3D MTR measurement: From 1.5 T to 3.0 T. *Neuroimage* 2006; 31: 181-186.

Cercignani M, Alexander DC. Optimal Acquisition Schemes for In-vivo Quantitative Magnetization Transfer MRI. *Magn Reson Med* 2006; 56: 803-810.

Conference abstracts

Cercignani M, Boulby P, Barker G, Symms M. An evaluation of the use of U-FLARE for rapid acquisition of B0 field maps for undistortion of EPI. Proc Intl Soc Mag Reson Med 2004; 2176.

Cercignani M, Symms M, Boulby P, Tozer D, Tofts P, Barker G. Three-dimensional quantitative magnetizion transfer imaging of the human brain. Proc Intl Soc Mag Reson Med 2004; 2332.

Cercignani M, Symms M, Boulby P, Barker G. Errors in diffusion tensor data following B0 field map correction. Proc 10th Annual Meeting of the British Chapter of ISMRM; 2004; P4.

Cercignani M, Symms M, Barker G. Quantification of MT Parameters in Vivo and Optimization of MTR Acquisition at 3.0 T. Proc Intl Soc Mag Reson Med 2005; 2226.

Cercignani M, Alexander DC. Optimal sampling for quantitative magnetisation transfer. Proc Intl Soc Mag Reson Med 2006; 3498.

Cercignani M, Symms MR, Boubly PA, Barker GJ. Quantification of B_0 and B_1 effects on the estimation of MT parameters at 3.0 T. Proc Intl Soc Mag Reson Med 2006; 3500.

List of Contents

List of Tables

List of Figures

Page

Chapter 1

Chapter 2

Chapter 3

Chapter 5

Chapter 6

Appendix B

Introduction

Magnetic resonance imaging (MRI) has become one of the most common methods of imaging the brain. This is mainly due to the exquisite contrast it provides without the use of radiation between different tissue compartments, such as white and grey matter, as well as between healthy and pathological tissue. Another characteristic of MRI is the possibility of manipulating nuclear spins in order to produce a large number of different image contrasts. This property not only allows the collection of several different qualitative images of the brain, but also constitutes the basis for quantitative MRI. Typically, quantitative MRI techniques fit a model of the dependence of the MR signal on a physical process to a number of MRI measurements obtained at different settings of the acquisition pulse sequence, which is sensitized to the physical process of interest. Examples include T_1 and T_2 imaging, which map the longitudinal and transverse relaxation constants by fitting exponential decay models in each voxel (e.g. Crawley and Henkelman, 1988; Whittal et al., 1997); diffusion MRI which can map the apparent diffusion coefficient (Le Bihan et al., 1986) or diffusion tensor (Basser et al., 1994); magnetisation transfer (MT) (Henkelman et al., 1993) which maps indices of the molecular chemical environment. Beyond typically "structural" measures, MRI is also able to measure physiological information (such as hemodynamics (Boxerman et al., 1995)) and functional activity of the brain (Ogawa et al., 1990). Different quantitative MRI parameters can provide information about different characteristics of tissue, and, combined with clinical variables, may improve our understanding of some pathological conditions.

The possibility of non-invasively measuring many different physical quantities has clearly an enormous potential for characterizing biological changes in tissue: diagnosis and prognosis of neurological and psychiatric disease could perhaps one day be based on the appropriate combination of quantitative MRI parameters and clinical data. Two main limitations have prevented achieving this goal so far: on one hand, all the components of an MRI experiment which can degrade quantification, such as static and radio-frequency field inhomogeneity, image noise, and gradient

imperfections; on the other, the difficulty in optimising the combination of different parameters reflecting different properties.

In this context, every effort should be made to improve the reliability of quantitative MRI techniques, and to investigate the relationship between different MRI parameters.

This thesis is mainly focused on the improvement of one specific quantitative technique, namely MT, a contrast mechanism based on cross-relaxation and chemical exchange between protons in free water (protons in the 'liquid' pool) and those bound to macromolecules. Measures derived from MT-weighted MRI are interesting biological markers. In particular, evidence suggests that molecules associated with myelin dominate this exchange process in white matter (Kucharczyk et al., 1994; Koenig et al., 1990). MT-derived measures thus reflect the degree of myelination in white matter and can highlight demyelination from white-matter diseases such as multiple sclerosis.

The first attempts to extract quantitative information from MT imaging led to the introduction of the MT ratio (MTR) (Dousset et al., 1992), which is the percentage difference between the MRI signal measured in the absence and in the presence of MT saturation. Attempts to give a quantitative interpretation of the phenomenon led to the introduction of a number of MT models (Henkelman et al., 1993; Graham and Henkelman, 1997; Sled and Pike, 2000; Yarnykh, 2002; Ramani et al., 2002). The use of quantitative models of MT can be helpful in several ways. A model of signal behaviour as a function of the acquisition parameters can be used to optimise the pulse sequence used to measure the MTR, as described in Chapter 3 of this thesis. Alternatively, the model can be fitted to data collected with variable degrees of MT–weighting in order to estimate one or more physical parameters instead of a single MTR value. This approach (quantitative MT) is very promising, although the application of this technique *in vivo* still suffers from a number of limitations. Some of these problems are discussed in Chapter 4, where a series of experiments designed at improving the robustness of quantitative MT measurement *in vivo* are described. Directly related to the reliability of quantitative MT measurement is the measurement of the static (B_0) and of the radio-frequency (B_1) magnetic fields. Any deviation from their nominal values causes spatially varying error in the computed MT parameters (Sled and Pike, 2000). The measurement of B_1

is also important for other quantitative MRI measurements, such as T_1, while the measurement of B_0 is useful to correct geometric distortions in all echo-planar based MRI techniques. The *k*-space trajectory used to collect data in echo-planar experiments makes the geometric properties of such images incompatible with those of "conventional" MRI images. These differences cannot be removed by linear image registration techniques. This observation has clearly important consequences in the context of multi-modal MRI; a first step towards multi-parametric studies must be to achieve a good registration between quantitative maps. The subject of field mapping is discussed in more detail in Chapter 5. Finally, some preliminary results using multivariate analysis to combine several quantitative maps are presented in Chapter 6, providing some basis for the interpretation of multi-parametric measurements.

Chapter 1

Physics of NMR

Introduction and brief overview of NMR history

Nuclear magnetic resonance (NMR) was independently discovered by Felix Bloch and Edward Purcell in 1946 (Bloch et al., Purcell et al.); and since then it has been used as a tool for chemical analysis to probe the chemical environment of nuclear magnetism. The first images, obtained by using spatially-varying magnetic fields to encode the spatial information into the signal, were produced in 1973 (Lauterbur), thus initiating Magnetic Resonance Imaging (MRI). The word nuclear was in fact discarded in the 1980's in order to avoid the erroneous association with the use of nuclear fission, and thus with the connected danger. The first commercial MRI scanners began to appear in 1979 and the technique has quickly become widely used for its ability to safely and non invasevily image soft tissue. Unlike other radiological techniques, MRI, which is based on the interaction of small, rapidly varying magnetic fields with hydrogen nuclei in the soft tissues of the body, does not require ionizing radiation absorption.

Excellent books (e.g. Haacke et al., 1999; Gadian, 1995; and http://www.cis.rit.edu/htbooks/mri/) describe in details the physics of NMR. Here I include only a brief overview of the basic principles, as an introduction to the following chapters in which the specific MRI techniques relevant to this thesis are reviewed in more detail.

1.1 Basic Principles of NMR

NMR is based on the interactions between a nuclear spin and an external magnetic field. For several reasons, particularly its abundance in the human body and its sensitivity, the most relevant nucleus in NMR studies is hydrogen.

1.1.1 Nuclear magnetism

The hydrogen nucleus placed in a static magnetic field $\mathbf{B_0}$ is a single, positively charged proton spinning about its axis, i.e. it has an intrinsic angular momentum $\mathbf{J}$. since $\mathbf{J}$ is non-zero and the nucleus is charged, it also exhibits a magnetic moment μ. The component of $\mathbf{J}$ measured along one axis (say z) is

$$J_z = m_j \hbar, \qquad [1.1]$$

where, $\hbar = h/2\pi$ (with h= Plank's constant), and m_j is called the magnetic quantum number. m_j can assume $2j+1$ values ($-j$, $-j+1$, ...$j-1$,j), with j (quantum number) being a positive integer or half integer. The quantum number is related to the angular momentum as explained below. The orbital motion (**L**) and the intrinsic spin (**S**) both contribute to the total atomic angular momentum giving

$$\mathbf{J} = \mathbf{L} + \mathbf{S} \qquad [1.2]$$

Each of these vectors have quantum numbers, l and s, respectively, satisfying the relationships

$$L^2 = l(l+1)\hbar^2 \qquad [1.3]$$

$$S^2 = s(s+1)\hbar^2, \qquad [1.4]$$

where L and S represent the magnitude of the corresponding vectors. While l can only have integer values, s can also assume half integer values.

The magnitude of the total angular momentum, J, is also associated to a quantum number j, according to the relationship

$$J^2 = j(j+1)\hbar^2. \qquad [1.5]$$

The range of j values is found from

$$j = |l-s|, |l-s|+1, \ldots, l+s. \qquad [1.6]$$

Experiments following the discovery of the spin of the electron showed the proton to have also a spin of ½. The number of proton energy levels is therefore two,

$$m_j = \pm\frac{1}{2}, \qquad [1.7]$$

also referred to as 'spin up' and 'spin down'. These two energy states correspond to opposite orientations of the nucleus with respect to the applied magnetic field.

All nuclei containing an odd number of protons are characterized by the presence of an unpaired proton, and consequently exhibit a magnetic moment.

Nuclear magnetism is a form of *paramagnetism*, meaning that the individual nuclear spins are randomly oriented in the absence of an external field, resulting in zero net moment. However, when placed in a static magnetic field, they tend to align parallel or antiparallel to the field. The distribution of the two populations is given by the Maxwell-Boltzman distribution:

$$\frac{N_\beta}{N_\alpha} = \exp\left\{-\frac{\Delta E}{kT}\right\}, \qquad [1.8]$$

where N_α is the number of spins in the first state (parallel to the field) and N_β is the number of spins in the second state (antiparallel); ΔE is the energy difference between the states, k is the Boltzmann constant and T is the absolute temperature. The difference in the two populations creates a net magnetization aligned with the external field.

In Eq [1.8], the energy required to excite transitions from one state to the other is found to be

$$\Delta E = \gamma\hbar B_0 = \hbar\omega_0, \qquad [1.9]$$

where ω_0 is the Larmor frequency.

Due to the quantum nature of the proton spin, this subject can only be treated appropriately by quantum mechanics; however, when considering isolated spins (no coupling), most of the NMR theory can be understood using classical physics.

1.1.2 Classical view of NMR: Precession

The interaction of the magnetic moment $\boldsymbol{\mu}$ and the applied static magnetic field, $\mathbf{B_0}$, results in a *torque*, $\boldsymbol{\Gamma}$, acting on the spin, given by

$$\boldsymbol{\Gamma} = \boldsymbol{\mu} \times \mathbf{B_0}, \qquad [1.10]$$

where the symbol '×' indicates the vector product. The torque is related to the angular momentum, **J**, by:

$$\boldsymbol{\Gamma} = \frac{d\mathbf{J}}{dt} \qquad [1.11]$$

The constant of proportionality between the magnetic moment and the angular momentum, γ, is specific to each type of magnetic nucleus, and can be experimentally determined:

$$\boldsymbol{\mu} = \gamma\mathbf{J}\ . \qquad [1.12]$$

γ is called the gyromagnetic ratio, and it is often expressed in units HzT^{-1}. For the hydrogen proton, γ=42.6x10^6 HzT^{-1} (267 x10^6 rad s^{-1} T^{-1}).

Exploiting this relationship, Eq [1.11] can be rewritten as

$$\boldsymbol{\Gamma} = \frac{1}{\gamma}\cdot\frac{d\boldsymbol{\mu}}{dt}. \qquad [1.13]$$

Combining Eq [1.10] and Eq [1.13], we obtain a differential equation whose solution describes the motion of the spin under a static magnetic field:

$$\frac{d\boldsymbol{\mu}}{dt} = \gamma\boldsymbol{\mu} \times \mathbf{B}_0 . \qquad [1.14]$$

Solving Eq [1.14] gives

$$\boldsymbol{\mu} = |\mu| \sin\vartheta\left[\cos(\gamma B_0 t)\hat{i} - \sin(\gamma B_0 t)\hat{j}\right] + |\mu|\cos\vartheta\hat{k} , \qquad [1.15]$$

where ϑ is the angle formed by $\mathbf{B_0}$ and $\boldsymbol{\mu}$, and $\hat{i}$, $\hat{j}$ and $\hat{k}$ are the unit vectors parallel to the x, y, and z axes, respectively.

Eq [1.15] defines a precession about the z axis, at the so-called Larmor (angular) frequency

$$\omega_0 = \gamma B_0 . \qquad [1.16]$$

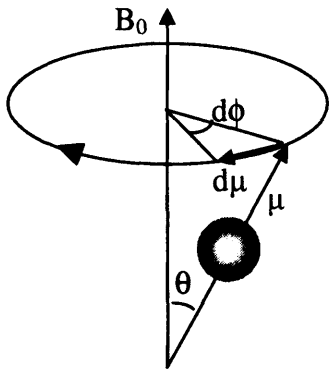

Fig 1.1. *Precession of a proton's spin about the magnetic field B_0. The Larmor frequency (ω) is given by $d\phi/dt$.*

1.1.3 Classical view of NMR: Magnetic Resonance

Magnetic Resonance occurs when the nucleus is exposed to a perturbation in the magnetic field, such as an electromagnetic wave, oscillating at the Larmor frequency. In practice this is obtained by applying a driving radio-frequency (RF) voltage to an LC circuit tuned to the Larmor frequency. The sample is placed in a coil which forms part of the inductance of the tuned circuit. From Eq [1.15], it can be seen that an RF magnetic field, B_1, able to tip the magnetization from the z axis must have components x and y, i.e., must have transverse components. The oscillating field generated by a constant ('square') RF pulse is of the form

$\mathbf{B}_1 = |B_1|[\cos(\omega_0 t)\hat{i} - \sin(\omega_0 t)\hat{j}]$. Its effect is to give a non-equilibrium orientation to the macroscopic magnetic moment, previously aligned with the static magnetic field along z, that is, to tilt it toward the x-y plane by a flip angle α, proportional to the B_1 field and to the duration of the pulse:

$$\alpha = \gamma \int_0^t B_1(t')dt' . \qquad [1.17]$$

This tilt is caused by the precession of the spins about the resultant magnetic field; the superimposition of the two precession processes results in a nutation.

A phenomenological description of NMR can be given by the Bloch equation (of which Eq [1.14] is a simplified version):

$$\frac{d\mathbf{M}}{dt} = \gamma \mathbf{M} \times \mathbf{B} - \frac{\left(M_x \hat{i} + M_y \hat{j}\right)}{T_2} - \frac{(M_z - M_0)}{T_1}\hat{k}, \qquad [1.18]$$

where **M** is the magnetization vector, i.e. the local sum of the magnetic field of protons, and M_0 is its longitudinal component at the equilibrium. The sum is taken over a volume V containing a large number of protons, but small enough that external fields can be considered constant over V. The ensemble of spins in V is called *isochromat*. The time constants, T_1 and T_2, represent the effect of the relaxation processes occurring after the RF pulse has been turned off, due to the interaction with the surrounding magnetic entities. The T_1 relaxation time governs the dissipation of energy from the nuclei to the molecular environment, which enables the transition that brings the spins back into alignment with B_0 (spin-lattice relaxation). The T_2 relaxation time accounts for the interactions between neighbouring magnetic entities which cause the orientation within the transverse plane of individual spins to become randomized, and thus the reduction in transverse magnetization. Both constants are related to the frequencies of magnetic field fluctuations in the sample.

1.1.4 Classical view of NMR: Relaxation

The coordinate system used so far is the laboratory frame: $\hat{i}$ and $\hat{j}$ define the transverse plane, while $\hat{k}$ is the longitudinal direction. At the end of the RF pulse, relaxation (and diffusion) processes begin to diminish the magnitude of the precessing magnetization vector, as the spins return to thermal equilibrium. The

signal seen during this return to equilibrium is called the free induction decay (FID), and the solution of Eq [1.18] is in this case

$$\mathbf{M}(t)=\begin{bmatrix} M_x(t) \\ M_y(t) \\ M_z(t) \end{bmatrix} \qquad [1.19]$$

with

$$\begin{aligned} M_x(t) &= e^{-t/T_2}\left(M_x^0 \cos\omega_0 t + M_y^0 \sin\omega_0 t\right) \\ M_y(t) &= e^{-t/T_2}\left(M_x^0 \sin\omega_0 t - M_y^0 \cos\omega_0 t\right) \\ M_z(t) &= M_z^0 e^{-t/T_1} + M_0\left(1-e^{-t/T_1}\right) \end{aligned} \qquad [1.20]$$

It can be seen from Eq [1.20] that the equilibrium (or steady-state) solution for $t\rightarrow\infty$ is

$$M_x(\infty)=0, M_y(\infty)=0, M_z(\infty)=M_0 . \qquad [1.21]$$

The description of free induction effects is simplified by transforming to a coordinate system $x'y'z$, in which the $x'y'$ plane is rotating at the Larmor frequency (the so-called *rotating frame*). In the rotating frame, the solution to the Bloch equation in the case of a 90° pulse (which converts completely the longitudinal magnetization into transverse magnetization) is

$$\begin{aligned} M_{x'y'}(t) &= M_0 e^{-t/T_2} \\ M_z(t) &= M_0\left(1-e^{-t/T_1}\right) \end{aligned} \qquad [1.22]$$

The description of precession and relaxation obtained by solving the phenomenological Bloch equations is sufficient for most imaging applications. The description of NMR on a more fundamental level can only be understood in the framework of quantum mechanics. In most cases, the solutions predicted by quantum mechanics for the same phenomena coincide with those obtained from the Bloch equations.

1.3 Signal detection

1.3.1 The NMR signal

The presence of a transverse component of magnetization after RF excitation results in a magnetic flux that produces an electromotive force (*emf*) in the coil. For the Faraday's law of induction

$$emf = -\frac{d\Phi}{dt}, \qquad [1.23]$$

where Φ, the magnetic flux, is given by

$$\Phi = \int_{coil} \mathbf{B} \cdot d\mathbf{S}, \qquad [1.24]$$

and the magnetic field **B** is integrated over the coil area.

From the reciprocity theorem (Hoult and Richards, 1976), the flux through the coil due to a magnetization source is equivalent to the flux due to the same coil that would pass through the source, and therefore, it can be written as

$$\Phi = \int_{sample} \mathbf{B}_c^{rec}(\mathbf{r}) \cdot \mathbf{M}(\mathbf{r},t) d^3 r, \qquad [1.25]$$

where $\mathbf{B}_c^{rec}(\mathbf{r})$ is the magnetic field per unit current, and $\mathbf{M}(\mathbf{r},t)$ represents the magnetization, the solution to the Bloch equations ([1.19]).

Combining Eqs [1.23], [1.24], and [1.25], we obtain

$$emf = -\frac{d\Phi}{dt} = -\frac{d}{dt} \int_{sample} d^3 r \mathbf{M}(\mathbf{r},t) \cdot \mathbf{B}_c^{rec}(\mathbf{r}) \qquad [1.26]$$

The magnetization vector is therefore measured by the voltage induced in the coil. The signal is then amplified, and shifted in frequency (demodulation). This is obtained by multiplying the signal by a sinusoid (in practice both a sinusoid and a cosinusoid are used to obtain to channel signals in quadrature) with a frequency $\Omega = \omega_0 + \delta\omega$, with $\delta\omega$ being the 'offset frequency', assumed to be much smaller than ω_0. Once centred at zero, the complex signal is digitised by an Analogue-to-Digital Converter (ADC). Some scanner have receivers fast enough to capture the original Larmor frequency without the need for demodulation.

Chapter 2

Pulse Sequences and Image Formation

Introduction

The signal detected after an NMR experiment is dependent not only on the properties of the sample, but also on the combination of RF pulses used to excite the magnetization. The specific combination of pulses, which is typically repeated several times, determines the type of *pulse sequence*. The signal produced by the whole sample, however, cannot be used to produce an *image*. Spatial encoding is needed to distinguish the signal coming from different positions. In MRI, this is achieved by imposing a magnetic field gradient over the static field B_0, and therefore making the Larmor frequency vary with the position.

As for NMR physiscs in Chapter 1, this chapter is intended as a brief overview of MRI concepts. The interested reader is referred to specialised books (e.g. Haacke et al., 1999) and to references therein for more details in this subject.

2.1 FID and Spin Echo

2.1.1 The FID sequence

It was shown in the previous chapter that the signal induced in the RF coil by an FID experiment is of the form

$$s(t) \propto M_{xy}(t) = M_0 e^{-t/T_2}. \qquad [2.1]$$

In a typical MR experiment, however, the signal is repetitively excited and measured. Therefore if we consider a pulse sequence consisting of a repeated FID experiment, i.e. of a series of 90° pulses, separated by an interval *TR* (repetition time), during which time spins partially relax (saturation recovery), the longitudinal magnetization available after the first cycle is given by the integral of the Bloch equations over *TR*:

$$\int_{M_z(0)}^{M_z(TR)} \frac{dM_z}{M_z - M_0} = -\frac{1}{T_1}\int_0^{TR} dt, \qquad [2.2].$$

i.e.:

$$M_z(TR) = M_0\left(1 - \exp\{-TR/T_1\}\right) \qquad [2.3]$$

As a consequence, the amount of magnetization converted to the *x-y* plane by the second pulse will be $M_z(TR)$, as given by Eq [2.3] (assuming $TR>>T_2$).

At the end of the second cycle, the amplitude of the signal induced in the coil, i.e., of the measured signal, will be proportional to the transverse component of the magnetization vector predicted by the Bloch equations:

$$s(t,t>TR) \propto M_{xy}(t) = M_z(TR)\exp\{-t/T_2\} = M_0(1-\exp\{-TR/T_1\})\exp\{-t/T_2\}. \quad [2.4]$$

Eq [2.4] shows how the amount of T_1-weighting can be controlled via the selection of an appropriate *TR*. Since different biological tissues are characterised by differing T_1 values, this provides an excellent contrast mechanism for MRI.

2.1.2 Transverse relaxation and T_2*

The dephasing that takes place after the 90° pulse is turned off is caused by two different phenomena:

1) interactions between individual magnetic moments and with other magnetic particles, governed by the time constant T_2;

2) the effect of the external magnetic field inhomogeneities (which affect in a slightly different way the precession frequency of different protons), governed by the time constant T_2'.

Because of these two phenomena, spins lose coherence over time according to the time constant T_2* with:

$$\frac{1}{T_2^*} = \frac{1}{T_2} + \frac{1}{T_2'}. \quad [2.5]$$

For the FID sequence described above, the NMR signal is measured during a given sampling interval after the 90° pulse. The amount of attenuation is related to the time from the 90° pulse. From Eq [2.4] we obtain:

$$s(TE) \propto M_{xy}(TE) = M_0(1-\exp\{-TR/T_1\})\exp\{-t/T_2^*\} \quad [2.6]$$

A simple representation of the repeated FID experiment is given by the pulse sequence diagram, in Fig 2.1.

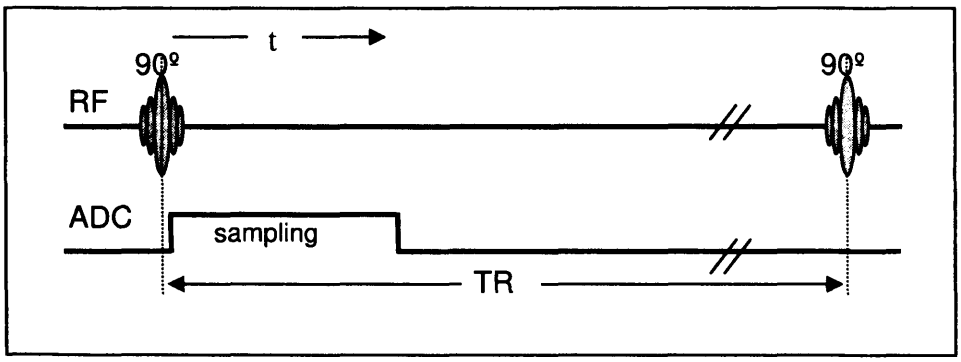

Fig 2.1. Repeated FID experiment. Conventionally, only one TR is shown.

The quantity T_2' is both machine and sample dependent. In general T_2' is much smaller than T_2, causing the spins to loose coherence very quickly, but the T_2' signal loss is reversible (Hahn, 1950). As soon as the RF pulse is switched off, all the spins precess in phase. Their precession rate is, however, proportional to the magnetic field they are sitting in, which is affected by local differences due to both interaction with other particles and main field inhomogeneities. As a consequence, they start to lose phase coherence. Refocusing can be achieved by positioning a refocusing RF pulse after a time t=*TE*/2 from the 90° pulse. If the refocusing pulse is a 180° pulse, its effect is to reverse the total phase accumulated so that, after a further period of *TE*/2, the spins end up in phase again, increasing the signal intensity. The amplitude of the *spin echo* (as the refocused signal is called) is lower than the starting value, but its attenuation is only due to interactions between spins (an irreversible loss of coherence). For this reason the interval *TE* is called 'echo' time. By varying *TE* it is possible to control the amount of T_2-weighting. A diagram of a spin echo pulse sequence is represented in Fig 2.2.

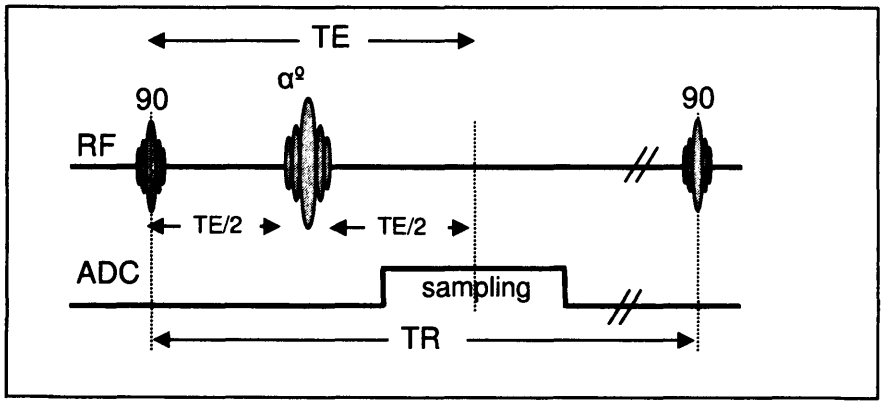

Fig 2.2. Spin echo diagram.

Any flip angle α can be used to form an echo, although the use of angle different from 180° produces more than one *coherence pathway* (Hennig, 1998). This is the consequence of an α pulse behaving partly like a 180° pulse (refocusing), partly like a 90° pulse (interconverting transverse and longitudinal magnetization), and partly like 0° pulse. This topic is further discussed in Chapter 5.

2.2 Spatial encoding

In order to obtain an MR image, it is necessary to impose some space dependence on the measured signal. This is typically obtained by the use of linear magnetic field gradients. The manipulation of these gradients can be exploited to obtain various type of imaging techniques.

2.2.1 Frequency encoding

The Larmor frequency of a spin is proportional to the magnetic field (see Chapter 1), and therefore is linearly proportional to its position ($\omega=\omega(r)$) if the field is linearly varying along the direction r:

$$\omega(r) = \gamma B_0 + \gamma \frac{\partial B}{\partial r} r = \gamma B_0 + \gamma G_r \cdot r . \qquad [2.7]$$

The frequency encoding gradient is switched on during signal acquisition. The phase accumulated during a time t, due to a gradient $G_r(t)$, is

$$\phi(r,t) = -\gamma r \int_0 G_r(t)dt' = -r \cdot k_r(t) \qquad [2.8]$$

where

$$k_r(t) = -\gamma \int_0 G_r(t)dt' \qquad [2.9]$$

If we assume a uniform receive sensitivity and we neglect relaxation effects, the measured NMR signal (in the rotating frame) is given by

$$s(t) \propto \int \rho(r) e^{i\phi(t)} dr , \qquad [2.10]$$

where ρ(r) is the spin density and the integral is calculated over the whole volume of the sample. Eq [2.10] can be derived quantum mechanically (see for example Slichter, 1990), and shows that the signal induced in the coil is proportional to the density of spins in the sample.

If we consider a one-dimensional problem, by substituting [2.8] into [2.10], we obtain

$$s(k_r) \propto \int \rho(r) e^{ik_r(t)r} dr, \qquad [2.11]$$

i.e., the measured signal is the Fourier transform (FT) of the spin density in *k-space*, which represents the conjugate domain of the spatial coordinate *r*.

The gradient strength is related to the image width in the spatial domain (field of view, or *FOV*). The NMR signal is sampled discretely at an interval Δt (dwell time), which must fulfill the Nyquist sampling formula

$$\Delta t \leq \frac{1}{\Delta f} = \frac{2\pi}{\gamma G FOV}. \qquad [2.12]$$

2.2.2 Phase encoding and slice-selection

In order to encode information in more than one dimension, spatially varying magnetic field gradients must be generated in different directions. In *spin-warp* imaging (Edelstein et al., 1980), the second direction (conventionally labeled *y*) is encoded by imposing a gradient of constant amplitude and duration, G_{pe}, prior to sampling. The measurement is then repeated a certain number of times varying the gradient amplitude. G_{pe} is called phase-encoding gradient. The most typical encoding scheme is Cartesian: in this case the increments are steps of constant area. Coverage of *k*-space can be achieved also with other geometries, for example radial.

Typically, 2D spatial encoding follows slice selection, i.e. the excitation of a single slice of chosen thickness. Slice selection is achieved by turning on a constant gradient in the direction orthogonal to the frequency-encoding and phase-encoding ones, while an RF pulse is applied (Sutherland and Hutchinson, 1978). Only the protons whose Larmor frequencies are within the range of frequencies ('bandwidth') of the pulse undergo transitions, while the rest of the sample gives no signal. The slice thickness is proportional to the bandwidth of the RF pulse and inversely proportional to the applied gradient strength (at least in the case of a small flip angle). In order to get a uniform flip angle across the slice, the analytic form of the RF excitation profile, in the frequency domain, must be proportional to a boxcar function, of bandwidth Δf. This implies that the temporal envelope of the pulse should have infinite duration, while realistic RF profiles have finite duration. This truncation in time leads to Gibbs ringing, and the artefact is worse near sharp

boundaries. For this reason an additional apodizing function is used to bring the profile smoothly to zero.

A typical pulse sequence for a 2D spin-warp spin-echo imaging sequence is shown in Fig 2.3, where the corresponding k-space filling is also shown.

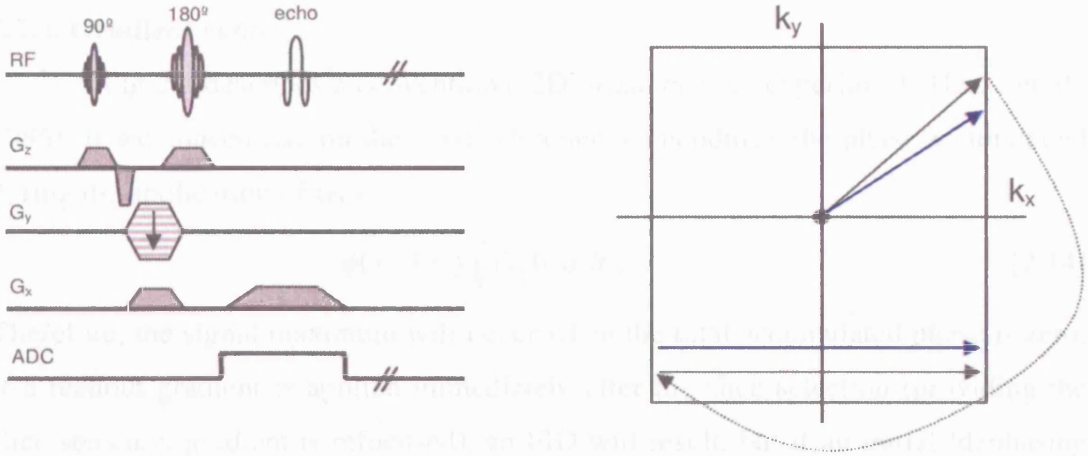

Fig 2.3. Basic pulse sequence diagram of a spin-echo sequence with spatial encoding (left), and corresponding k-space filling (right).

G_z selects the slice to be imaged; G_y and the first G_x move from the centre of k-space towards the right top edge (black arrow), the 180º pulse reverses the phase, effectively reversing k_x and k_y, while the second G_x, applied while the signal is sampled, makes k_x vary linearly with time. On the second repetition, G_y is decreased, causing a different line of k-space to be sampled (blue arrow).

If we assume x to be the frequency-encoding (or readout) direction, and y to be the phase-encoding direction, Eq [2.11] can be re-written for the two-dimensional case as:

$$s(k_x,k_y) \propto \int_{FOV_y}\int_{FOV_x} \rho(x,y) e^{i(k_x(t)x+k_y(t)y)} dxdy \qquad [2.13]$$

where FOV_x and FOV_y defines a region that fully contains the sample, or field of view. In practice k-space is sampled discretely and thus Eq [2.13] assumes a discrete form, with summations instead of integrals. Two dimensional Fourier Transform of $s(k_x,k_y)$ gives an image of $\rho(x,y)$, as a function of the spatial coordinates. Although $\rho(x,y)$ is real, the result of Fourier transforming k-space data is a complex image for each slice. Even in ideal conditions, the phase of the image would be zero only at the centre of the acquisition window for spin-echo acquisitions, due to the combination

of the quadrature channels (see Chapter 1). Moreover, phase terms can originate from imperfect sampling, unbalanced gradients or demodulation; for simplicity, usually only the magnitude is retained and displayed, unless interested in particular aspects of the phase (see for example Chapter 5 and B_0 field mapping).

2.2.3. Gradient echo

Fig 2.4 describes a conventional 2D *gradient echo* experiment (Haase et al., 1986). If we concentrate on the *x* axis (frequency encoding), the phase accumulated during the application of G_x is

$$\phi(x,t) = \gamma \int_0^t G_x(t')x dt' . \qquad [2.14]$$

Therefore, the signal maximum will occur when the total accumulated phase is zero. If a readout gradient is applied immediately after the slice selection (providing the slice selection gradient is refocused), an FID will result, but if an initial 'dephasing gradient' is applied (as in the figure), the signal maximum will fall at a later (specified by the dephasing gradient's area) time, with an echo occurring when the area of the positive lobe of the gradient equals the area of the negative lobe.

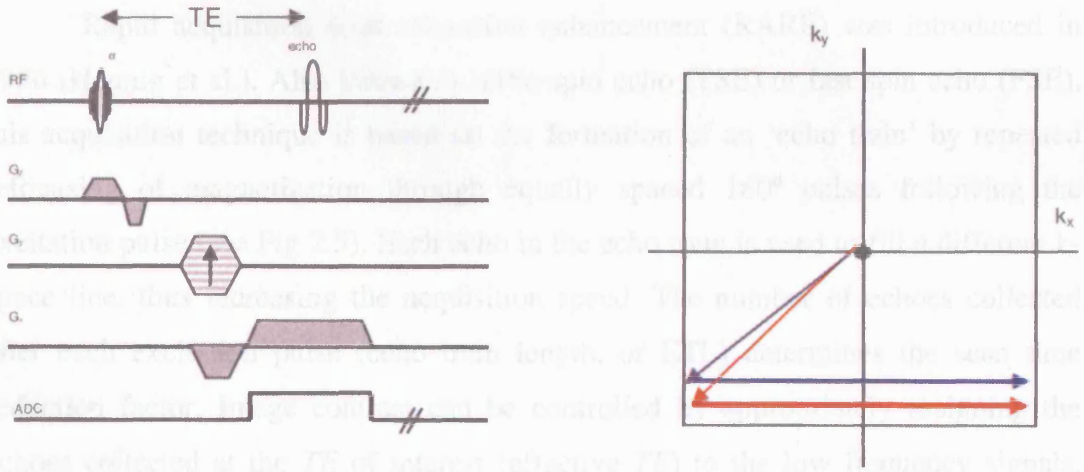

Fig 2.4. A basic gradient–echo pulse sequence diagram (left) and corresponding k-space filling (right).

Slice selection and phase encoding are used in the same way as in the spin-echo in Fig 2.3. In gradient-echo experiments, typically flip angles $\alpha<90^\circ$ are used, so that a shorter *TR* can be employed. The use of small flip angles is not practical in

spin-echo experiments, where the magnetization vector is inverted by the refocusing pulse and therefore long *TR*s are needed anyway to allow the recovery of its longitudinal component.

In a gradient echo sequence, the contrast depends on the choice of flip angle as well as the *TR* and *TE*. The equation describing signal dependency on acquisition parameters can be obtained by solving the Bloch equations with the relevant boundary conditions. Assuming that any residual transverse magnetization is spoilt before excitation (by the use of either RF pulses or crusher gradients-see Crawley et al., 1988) it can be shown that the measured signal intensity (*SI*) is given by:

$$SI = M_0 \frac{\left(1-\exp\left\{-TR/T_1\right\}\right)}{1-\cos\alpha\exp\left\{-TR/T_1\right\}}\exp\left\{-TE/T_2\right\}\sin\alpha\,. \qquad [2.15]$$

The maximum signal occurs at the flip angle $\alpha=\arccos(\exp\{-TR/T_1\})$, known as the Ernst angle, which nulls the derivative of Eq [2.15] with respect to α (Ernst and Anderson, 1966).

Other, more complex, relationships apply if the magnetization is not spoiled (Hawkes and Patz, 1989). These steady state free precession (SSFP) sequences are of interest for the imaging of tissues with large T_2/T_1 ratio.

2.2.4 Rapid acquisition with relaxation enhancement

Rapid acquisition with relaxation enhancement (RARE) was introduced in 1986 (Hennig et al.). Also known as turbo spin echo (TSE) or fast spin echo (FSE), this acquisition technique is based on the formation of an 'echo train' by repeated refocusing of magnetization through equally spaced 180° pulses following the excitation pulse (see Fig 2.5). Each echo in the echo train is used to fill a different k-space line, thus increasing the acquisition speed. The number of echoes collected after each excitation pulse (echo train length, or ETL) determines the scan time reduction factor. Image contrast can be controlled by appropriately assigning the echoes collected at the *TE* of interest (effective *TE*) to the low frequency signals, while confining those collected at different *TE*s to the edges of *k*-space. The use of large ETL can result in edge artifacts, whose appearance depends on the T_2 of tissues. Blurring (i.e. loss of high spatial frequency information) is greatest for tissues with a short T_2, and minimal for those with long T_2, and mainly affects images with a short effective echo time, for which large amounts of k space are being

collected at relatively long TEs. Conversely, in images with a long effective echo time, for which large amounts of k space are being collected at relatively short echo times, edge enhancement (ie enhancement of high frequency information) may occur in tissues with a short T_2. The interaction of these effects can lead to an overlap of signal from different tissues at the tissue edges that is more complex than the simple 'partial volume' effect seen in other MR images. Because in RARE refocusing RF pulses occur more rapidly than in conventional spin-echoes, the modulation of the echo train induced by *J*-coupling (i.e. the interaction between different chemical shift resonances) is reduced, thus reducing the signal loss normally observed in lipids with conventional spin echo sequences (Henkelman et al., 1992). Thus, lipids appear brighter on RARE than on corresponding conventional spin-echoes.

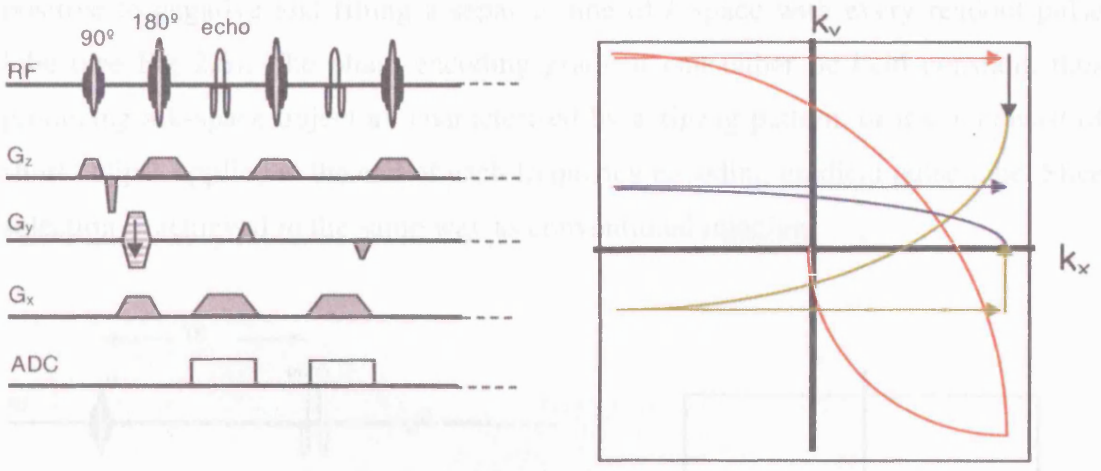

Fig 2.5. Basic pulse sequence diagram of a RARE sequence (left), and corresponding k-space filling (right).

G_z selects the slice to be imaged; the first G_x and G_y move from the centre of k-space towards the right bottom edge (red arrow), the 180º pulse reverses the phase, effectively reversing k_x and k_y, while the second G_x, applied while the signal is sampled, makes k_x vary linearly with time. The second G_y decreases ky (black arrow), and the 180º pulse again reverses k_x and k_y, causing a different line of k-space to be sampled (green line).

The main practical disadvantage of RARE (particularly at high field) is the increased specific absorption rate (SAR) imposed by the high density of 180º pulses,

which limits its use as a single-shot technique. This subject is further discussed in Chapter 5, where ultra-fast low angle RARE is introduced. It should also be noted that in RARE each refocusing radio pulse targeted to a particular image slice has the added effect of partially saturating macromolecular protons in the other imaging planes, thus giving a magnetization transfer effect (Dixon et al., 1990). The magnetization transfer phenomenon is described in much more detail in Chapters 3 and 4.

2.2.5 Echo-planar imaging

The idea behind single-shot echo-planar imaging (EPI) is the acquisition of enough data to reconstruct an image using the train of echoes after a single RF excitation (Mansfield, 1977). This is achieved by switching the readout gradient from positive to negative and filling a separate line of *k*-space with every readout pulse lobe (see Fig 2.6). The phase-encoding gradient can either be held constant, thus producing a k-space trajectory characterised by a zigzag pattern, or it can consist of short "blips" applied at the end of each frequency encoding gradient pulse lobe. Slice selection is achieved in the same way as conventional imaging.

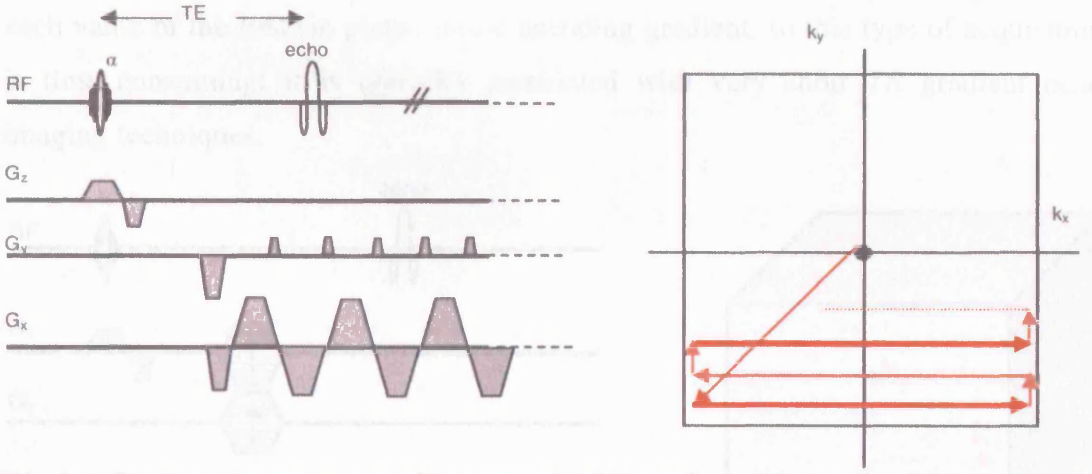

Fig 2.6. Basic pulse sequence diagram of a blipped gradient-echo EPI (left), and corresponding k-space filling (right).

G_z selects the slice to be imaged; at each G_y "blip", k_y is increased by a fixed amount, while the shape of G_x causes every other line of k-space to be sampled backwards.

The simplest EPI experiment is based on a gradient-echo acquisition (selective RF pulse, followed by EPI readout). Spin-echo excitation (a 90° pulse followed by a refocusing 180° pulse) can also be used to mitigate T_2* decay. EPI is more sensitive to image artefacts than conventional spin-warp imaging, due to the long read-out period, and to the reversal of every other line of *k*-space. Some of these artefacts are discussed in more detail in Chapter 5. More detailed reviews can be found in Schmitt et al. (1998). Multi-shot EPI, where only a portion of *k*-space is collected after each RF excitation, is less prone to off-resonance artifacts, and can be used to obtain images with higher resolution, at the price of an increase in imaging time.

2.2.6 3D Fourier encoding

2.2.6.1 Theory

A conventional 3D imaging sequence is obtained by adding an additional phase encoding gradient in the same direction as the slice selection gradients in order to phase encode the third dimension as well. Slice-selection is used to excite a *slab*, with a given number of phase encodings per slab. The resulting slice thickness is equal to the slab thickness divided by the number of phase-encodings. The second (through plane) phase encoding gradient must be stepped through all its values for each value of the first (in plane) phase encoding gradient, so this type of acquisition is time consuming; it is typically associated with very short *TR* gradient echo imaging techniques.

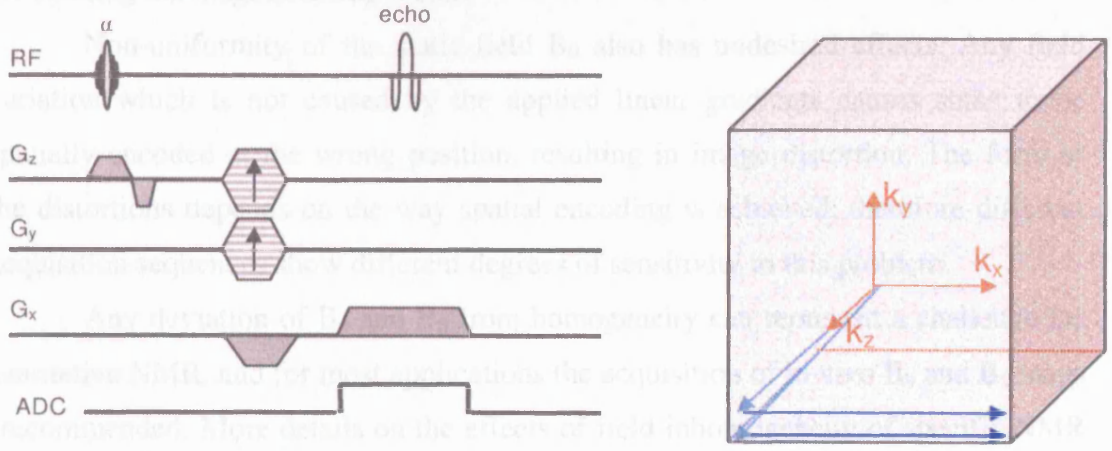

Fig 2.6. *A* **3D gradient echo imaging sequence (left) and a 3D k-space filling (right).**

2.3.6.2 3D vs 2D imaging

The use of phase encoding along two dimensions lengthens the scan time, effectively limiting the use of 'pure' 3D acquisition to short *TR* sequences. However, a number of advantages of this acquisition scheme over a multi-slice approach make it attractive for some applications.

The partition thickness can be reduced by simply increasing the number of partitions per slab, without any limitations on RF amplitude. All the artifacts related to imperfect RF pulses, such as inhomogenous slice-profile, or cross-talk between adjacent slices (Kuchaeczyk et al., 1988) are not present in 3D imaging. Finally the SNR in a 3D acquisition is increased by a factor $\sqrt{N_z}$ when keeping all other parameters the same.

2.3 B_0 and B_1 inhomogeneities

If the transmit and/or receive RF coils do not produce a uniform field over the imaging volume, this will affect the signal intensity. The dependency on the receiver field is one of proportionality, and, therefore, the image will appear darker where the receiver field is lower and brighter where it is higher. Non-uniformity in the transmit field has more complex effects, as it will modulate the flip angle of the pulses used for exciting the magnetization vector.

Non-uniformity of the static field B_0 also has undesired effects. Any field variation which is not caused by the applied linear gradients causes spins to be spatially encoded at the wrong position, resulting in image distortion. The form of the distortions depends on the way spatial encoding is achieved; therefore different acquisition sequences show different degrees of sensitivity to this problem.

Any deviation of B_1 and B_0 from homogeneity can represent a challenge for quantitative NMR, and for most applications the acquisition of in vivo B_0 and B_1 maps is recommended. More details on the effects of field inhomogeneity of specific NMR techniques will be given in the following chapters.

Chapter 3

Magnetization Transfer

Introduction

Magnetization Transfer (MT) is a contrast mechanism based on cross-relaxation and chemical exchange, first demonstrated in vivo by Wolff and Balaban (1988). Due to the selective saturation of the hydrogen protons associated with macromolecules, MT produces a source of contrast alternative to T_1 and T_2, which has become widely used in clinical imaging to improve the suppression of static tissue in MR angiography, and to increase lesion visibility on conventional MRI when Gadolinium (Gd) based contrast agents are used. Another useful application of MT is the so-called MT ratio (MTR). An MTR measurement is derived from two images, one with MT saturation and one without. An MTR map is computed as the percentage difference of the two. Every pixel in such a map represents the efficiency of magnetization transfer in that anatomical location. MTR is a quantitative measurement, that appears to be sensitive to subtle abnormalities not detectable on conventional MRI, and it proved able to identify diffuse changes in normal appearing brain tissue of patients with multiple sclerosis (Filippi et al., 1998) and of patients with epilepsy and no macroscopic abnormalities detected on conventional MRI (Rugg-Gunn et al., 2001). More recently, MTR has been applied to the study of major psychiatric illnesses, namely schizophrenia and bipolar disorder (Foong et al., 2001; Bagary et al., 2003; Bruno et al., 2004). Significant cortical MTR reductions, unrelated to tissue volume changes, have been reported predominantly in bilateral fronto-temporal regions in patients with chronic schizophrenia (Foong et al., 2001) and in the medial prefrontal and insular areas in first episode schizophrenic patients (Bagary et al., 2003) indicating that this technique is sensitive to subtle neuropathological abnormalities in these patients.

In this chapter the basic principles of MT (section 3.1) will be reviewed and the following experiments addressing MTR measurement and optimisation will be described: a) investigation of the effects of T_1-weighting on MTR (section 3.2); b) maximisation of the white-to-grey matter contrast-to-noise ratio (CNR) at a given

field strength, as a function of the amplitude and the offset frequency of the MT pulses used to achieve saturation (section 3.3). Quantitative magnetization transfer, an extension of the basic MT procedure aiming at measuring more fundamental physical quantities, is discussed in Chapter 4.

3.1 Basic Principles

The MT effect can be modelled using two or more compartments (or "pools"). The relaxation rates and the relative populations of the compartments can be estimated by collecting data at a range of saturation powers and frequencies. This general description has been referred to as quantitative MT (Henkelman, 1993; Sled and Pike, 2000; Ramani et al., 2002), cross-relaxation imaging (Yarnyck, 2002), or Z-spectrum imaging (Grad and Bryant, 1990) by different authors. The results presented in this chapter and in the next one are based on a two-pool model (Henkelman et al., 1993), which is briefly described in this section.

3.1.1 The two-pool model

The Magnetization Transfer (MT) effect is based on the exchange of magnetization occurring between groups of spins characterised by different molecular environments. In biological tissues, two or more "pools" of protons can be identified: those in free water (the free, or liquid pool) and those bound to large molecules (the macromolecular, or semisolid pool). The latter protons are characterised by a very short transverse relaxation time and therefore do not directly contribute to image contrast in conventional MRI. Nevertheless, since an exchange of magnetization occurs between the two pools via cross-relaxation and chemical exchange (Wolff and Balaban, 1988), it is possible to sensitise an MR experiment to the magnetic resonance characteristics of bound protons and to indirectly measure them.

The macromolecular spins have a broader absorption lineshape than the liquid spins, making them much more (about 10^6 times) sensitive to off-resonance irradiation (see Fig 3.1). Selective saturation can thus be achieved by applying radio-frequency (RF) energy several kilohertz off resonance from the Larmor frequency. (the natural linewidth of free water is of the order of 10-20 Hz at 1.5 T). This

preferential saturation is transferred to the liquid pool spins, and hence detected by MRI.

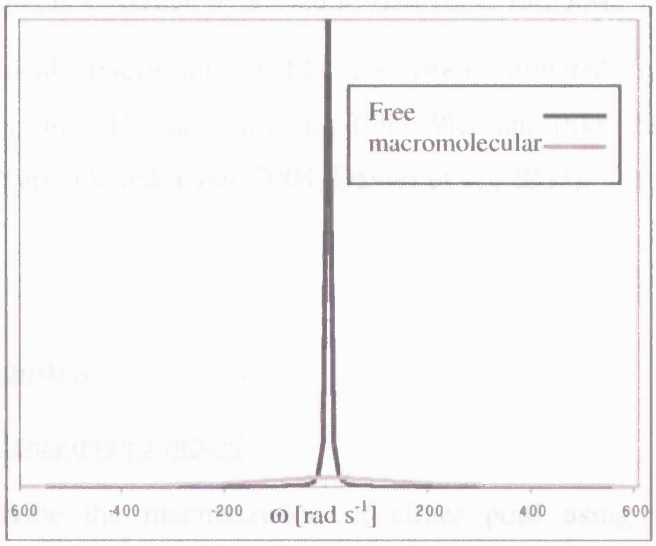

Fig 3.1. Schematic representation of the absorption lineshapes of the pools (not in scale).

Quantitatively, MT can be understood using the two-pool model, developed by Henkelman et al. (1993) for the continuous wave (CW) case, in which RF pulses of several seconds with a given amplitude are used to saturate the macromolecular

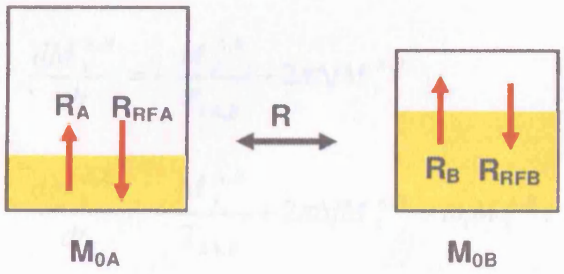

Fig 3.2. Henkelman's two pool model.

The model is schematically represented in Fig 3.2. "A" labels the free, or liquid pool, while "B" is the semisolid, or macromolecular pool. The yellow areas represent the saturated spins. M_0^A and M_0^B are the fully relaxed values of magnetization associated with the two pools. Each pool is characterised by its own longitudinal relaxation rates (R_A and R_B), and by its rate of loss of longitudinal magnetization due to the RF irradiation (R_{RFA} and R_{RFB}). The exchange rate between the two pools, R, is assumed to be symmetrical. In a steady state, the rate of

exchange in each direction is proportional to the relative populations (i.e the exchange from A to B is governed by a pseudo-first-order rate RM_0^B, while the exchange from B to A is governed by a pseudo-first-order rate RM_0^A).

The theoretical description of MT has been validated by a number of experiments both *in vitro* (Henkelman et al., 1993; Sled and Pike, 2000) and *in vivo* (Sled et al., 2004; Yarnyck and Yuan, 2004, Davies et al., 2004).

3.1.2 Analytical solution

3.1.2.1 CW case: Henkelman's model

If we describe the magnetization of either pool using its longitudinal components (M_z^A, M_z^B) and its transverse components (M_x^A, M_y^A, M_x^B, M_y^B), the coupled Bloch equations for the system illustrated in Fig 3.2 can be written as follows (Henkelman et al., 1993).

$$\frac{dM_z^A}{dt} = R_A\left(M_0^A - M_Z^A\right) - RM_0^B M_Z^A + RM_0^A M_Z^B + \omega_1 M_y^A \qquad [3.1]$$

$$\frac{dM_z^B}{dt} = R_B\left(M_0^B - M_Z^B\right) - RM_0^A M_Z^B + RM_0^B M_Z^A + \omega_1 M_y^B \qquad [3.2]$$

$$\frac{dM_x^{A,B}}{dt} = -\frac{M_x^{A,B}}{T_{2A,B}} - 2\pi\Delta f M_y^{A,B} \qquad [3.3, 3.4]$$

$$\frac{dM_y^{A,B}}{dt} = -\frac{M_y^{A,B}}{T_{2A,B}} + 2\pi\Delta f M_x^{A,B} - \omega_1 M_z^{A,B}. \qquad [3.5, 3.6]$$

In Eqs [3.1] to [3.6], $T_{2A,B}$ represent the transverse relaxation time of the corresponding pool, Δf represents the frequency offset of the MT pulse, ω_1 is the amplitude of the pulse expressed in rad/s (i.e. the angular frequency of precession induced by the off-resonance pulse), and all the other symbols are as defined above.

This system of 6 equations can be solved with respect to M_Z^A for the steady state condition (i.e. when all derivatives are equal to zero), leading to (Henkelman et al., 1993):

$$M_z^A = \frac{R_B R M_0^B + R_{RFB} R_A + R_B R_A + R_A R}{(R_A + R_{RFA} + R M_0^B)(R_B + R_{RFB} + R) - R R M_0^B} \quad [3.7]$$

where $M_0{}^A$ has been assumed equal to 1 and

$$R_{RFA} = \frac{\omega_1^2 T_{2A}}{1 + (2\pi\Delta f T_{2A})^2}, R_{RFB} = \frac{\omega_1^2 T_{2B}}{1 + (2\pi\Delta f T_{2B})^2} \quad [3.8, 3.9]$$

By dividing both its numerator and denominator by R_A, Eq [3.7] can be seen to include only five independent parameters (R, $RM_0{}^B/R_A$, $1/R_A T_2{}^A$, R_B, and $T_2{}^B$):

$$M_z = \frac{R_B\left[\frac{RM_0^B}{R_A}\right] + R_{RFB} + R_B + R}{\left[\frac{RM_0^B}{R_A}\right](R_B + R_{RFB}) + \left(1 + \left[\frac{\omega_1}{2\pi\Delta f}\right]^2\left[\frac{1}{R_A T_2^A}\right]\right)(R_{RFB} + R_B + R)} \quad [3.10]$$

where $1 << (2\pi\Delta f T_{2A})^2$ was assumed.

In the Bloch equations, the RF absorption lineshape is assumed to be Lorentzian for both pools, hence Eqs [3.8, 3.9]. Such a description, however, is not adequate for the semisolid component, where R_{RFB} is in general modeled with alternative lineshapes. In gels, excellent agreement with experimental data was found when using a Gaussian lineshape (Henkelman et al., 1993; Sled and Pike, 2000):

$$R_{RFB} = \omega_1^2 \sqrt{2\pi} T_2^B \exp\left(-\frac{(2\pi\Delta f T_2^B)^2}{2}\right) \quad [3.11]$$

In biological tissue, some investigators have attempted to extract the absorption lineshape from experimental data without a priori hypothesis of its analytical description (Li et al., 1997). The lineshapes for gray and white matter were found to be the same, and well described by a super-Lorentzian. In this case the expression for R_{RFB} is:

$$R_{RFB} = \omega_1^2 \pi\left[T_2^B \int_0^1 \frac{1}{|3u^2 - 1|} \exp\left(-2\left(\frac{2\pi\Delta f T_2^B}{3u^2 - 1}\right)^2\right) du\right]. \quad [3.12]$$

It should be noted that such lineshapes are not a solution of the Bloch equations, as a single T_2 rate can only give rise to a Lorentzian lineshape (Henkelman

et al., 1993) so substituting them into Eq [3.7] gives expressions which do not satisfy Eqs [3.1 - 3.6], but nevertheless appear to fit the experimental data.

3.1.2.2. Pulsed MT

The model is exact only when water protons are fully saturated via CW irradiation, a condition impractical to achieve during an *in-vivo* imaging experiment. Nevertheless, the model has successively been extended to include saturation pulses of short duration compared to T_1^A (of the order of 10-20 ms), the so-called pulsed MT acquisition (Graham and Henkelman, 1997). In this case, equations [3.1] and [3.3]-[3.6] must be modified by making ω_1 explicitly dependent on time ($\omega_1 = \omega_1(t)$), while Eq [3.2] is replaced by

$$\frac{dM_z^B}{dt} = R_A\left(M_0^B - M_Z^B\right) - \left(R_{RFB}(2\pi\Delta f, t) + R\right)M_z^B + RM_0^B M_Z^A \qquad [3.2']$$

where $R_{RFB}(2\pi\Delta f,t) = \pi\omega_1^2(t)g(2\pi\Delta f)$ is the rate of saturation of longitudinal magnetization in pool B, with absorption lineshape $g(2\pi\Delta f)$.

Typically, Gaussian RF pulses are used for MT saturation, giving

$$\omega_1(t) = \gamma B_{1MAX} \exp\left\{-\frac{\left(t - \tau_{SAT}/2\right)^2}{2\sigma^2} + i2\pi\Delta f t\right\}, \qquad [3.13]$$

where B_{1MAX} is the maximum amplitude of the time varying magnetic field, σ is the standard deviation of the Gaussian envelope, and τ_{SAT} is the duration of the pulse.

The effect of the MT pulse on the two pools must be considered separately. The *excitation* of the liquid pool can be modelled by numerically solving the time-dependent Bloch equations, while a similar concept does not apply to the semisolid pool (whose transverse relaxation time is too short). *Absorption* of RF energy by both pools can be modelled by two different lineshapes, as discussed above. Absorption results in *saturation* of the longitudinal magnetization of the semisolid pool only. Finally, when the MT pulse is turned off, the magnetization in both pools *evolves* governed first by the exchange rate R, and later by the longitudinal relaxation rate R_A driving the system back into equilibrium.

In the absence of RF excitation, the solution can be found analytically (Edzes and Samulski, 1977) giving

$$M_z^A = c_1 e^{-\lambda_- t} + c_2 e^{-\lambda_+ t} + 1 \qquad [3.14]$$

$$M_z^B = c_1\left(M_0^B + \frac{R_A}{R} - \frac{\lambda_-}{R}\right)e^{-\lambda_- t} + c_2\left(M_0^B + \frac{R_A}{R} - \frac{\lambda_+}{R}\right)e^{-\lambda_+ t} + M_0^B, \qquad [3.15]$$

with

$$\lambda_{+,-} = \frac{1}{2}\left\{\left[R(1+M_0^B) + R_A + R_B\right] \mp \sqrt{\left(RM_0^B - R + R_A - R_B\right)^2 + 4R^2 M_0^B}\right\}$$

$$c_1 = M_z^A(t_n) - 1 - c_2 \qquad [3.16]$$

$$c_2 = \frac{R\left\{\left[M_z^A(t_n) - 1\right]\left(M_0^B + \frac{R_A}{R} - \frac{\lambda_-}{R}\right) - M_z^B(t_n) + M_0^B\right\}}{\lambda_+ - \lambda_-},$$

where $M_Z^A(t_n)$ and $M_Z^B(t_n)$ represent the magnetization in each pool produced by the n^{th} pulse in a train of RF saturation pulses. The rates $\lambda_{+,-}$ are the eigenvalues in the absence of RF irradiation and are independent of $M_Z^A(t_n)$ and $M_Z^B(t_n)$. In Eqs [3.14]-[3.16], no MT exchange is assumed to occur between the pools associated with the transverse components of magnetization, as this exchange is assumed to be small compared to that associated with the longitudinal components.

Equations [3.14]-[3.16] require numerical evaluation for a given train of MT pulses.

A similar model has been developed by Bruce Pike (Pike, 1996) and John Sled (Sled and Pike, 2000). Approximating a pulse sequence as a series of periods of free precession, CW irradiation, and instantaneous saturation of the free pool, they proposed an equation which can be fitted directly to the measured signal. The expression can be found in Sled and Pike (2000). This exact solution has the advantage of incorporating the effect of the excitation RF pulses as well, and therefore to make it possible to account for T_1-weighting. However, it requires the numerical evaluation of ordinary differential equations at least for the estimation of the effect of the MT pulse on the free pool.

3.1.2.3 CW power equivalent approximation

A simpler way of dealing with pulsed MT is the use of a continuous wave power equivalent approximation (Ramani et al., 2002), where the pulse is simply replaced by a CW irradiation with the same mean square amplitude. The equivalent CW precession frequency (ω_{1CWPE}) is defined as

$$\omega_{1CWPE} = \gamma\sqrt{P_{SAT}} = \gamma B_{1CWPE}, \qquad [3.17]$$

where γ is the gyromagnetic ratio and P_{SAT} is the mean square saturating field.

With knowledge of the shape of the pulse, of its duration (τ_{SAT}), and of its equivalent on-resonance flip angle (θ), B_{MAX} can be calculated by assuming:

$$\theta = \left[\frac{180}{\pi}\right]\gamma p_1 B_{MAX}\tau_{SAT} \qquad [3.18]$$

where p_1 is the ratio of the mean amplitude of the saturation pulse to that of a rectangular pulse of the same amplitude. P_{SAT} can then be determined (Berry et al., 1999) from

$$P_{SAT} = p_2 B_{MAX}{}^2 \frac{\tau_{SAT}}{TR'} \qquad [3.19]$$

(where p_2 is the ratio of the mean square amplitude of the saturation pulses to that of a rectangular pulse of the same amplitude) and substituted in Eq [3.17]. This approximation is believed to give accurate results, providing that the interval between subsequent pulses is short enough.

3.1.3 Direct Saturation

Although MT MRI aims at measuring the signal decrease indirectly induced by the interaction between the two pools, saturation is never perfectly selective with the typical values of ω_1 and Δf (<10kHz) used in in vivo. Therefore, direct saturation of the free pool (or "RF bleedover") cannot generally be avoided, and the use of sufficiently large (typically more than few hundred Hz) offset frequencies is recommended. The measured MTR can be expressed as (Henkelman et al., 2001)

$$MTR = \frac{M_0 - M_{SAT}}{M_0} = 1 - \left[\frac{M_{DIR}}{M_0} + \frac{M_{MT}}{M_0}\right], \qquad [3.20]$$

where M_{DIR} is the direct effect contribution and M_{MT} is the true MT contribution. Spoiling gradients can be used in order to suppress the transverse magnetisation which might be generated by off-resonance irradiation.

The direct effect of RF irradiation on the liquid pool can be estimated by solving Eqs [3.1]-[3.6] in the absence of exchange (by setting R=0, M_0^B=0) (Henkelman et al., 1993).

3.1.4 Interaction between T_1 relaxation and MT saturation

While the semisolid pool (B) is held in partial or full saturation, the longitudinal relaxation of the system appears to be governed by a shorter time constant (T_1^S) than the T_1 measured in the absence of MT saturation (T_1^U) (Hajnal et al., 1992, Wolff and Balaban, 1988).

In conditions of full saturation of the pool B, with no direct saturation of pool A, the measured relaxation rate is

$$\frac{1}{T_1^S} = \frac{1}{T_1^U} + RM_0^B, \qquad [3.21]$$

where RM_0^B represents the pseudo-first-order A-to-B exchange rate constant (Henkelman et al., 1993) (often also termed k_f, or k).

MTR calculation typically requires the collection of two images, with (M_S) and without (M_U) MT saturation:

$$MTR = \frac{M_U - M_S}{M_U} \qquad [3.22]$$

If any residual T_1 or T_2 weighting is present, the M_U value in Eq [3.22] must not be confused with the equilibrium magnetization, and it simply represents the partially recovered magnetization available prior to the application of an excitation RF pulse. Under these circumstances, the different value of T_1 will differentially affect the saturated and unsaturated images used to calculate the MTR. In particular, the calculated MTR will decrease as the amount of T_1 weighting (which is dependent upon the acquisition parameters) increases, and the decrease will be faster for tissues with longer T_1 (e.g. grey matter *vs* white matter). Pathological changes are likely to affect both T_1 and the MTR, and the interpretation of images reflecting a complicated

interaction between these effects can be difficult. This effect is well understood and has been reported previously (Finelli et al., 1998), however, it is often overlooked in clinical protocols.

3.2 Experiment A: Evaluation of the effects of T_1-weighting on MTR calculation

3.2.1 Theory

When measuring MTR, the resulting MTR images should ideally be mainly dependent on the MT process, and the effect of other weightings minimized. It is particularly important to remove all those effects which differ between saturated and unsaturated acquisitions, such as T_1-weighting (see Section 3.1.4, above). This condition is generally met when using a sufficiently long TR, such as those typical of a 2D multi-slice 'spin warp' acquisition. On the other hand, 3D gradient-echo (GRE) has other advantages that make it attractive for MT imaging, such as better SNR per unit time, higher resolution, and less incidental MT effect from neighboring slices (Dixon et al., 1990), which have led to 3D imaging being often applied to MTR measurement (Dousset et al., 1992; Finelli et al., 1996, Tanabe et al., 1998). 3D imaging can only be accomplished efficiently when using short TRs (typically a few tens of milliseconds), and therefore T_1-weighting must be mitigated by using small excitation flip angles (α), albeit at the price of lower SNR.

By integrating the Bloch equations, it is possible to derive the values of the longitudinal (M_z) magnetization component immediately before the excitation RF pulse (TR^-) in a (spoiled) GRE experiment using an excitation flip angle of amplitude α (Ernst and Anderson, 1966):

$$M_z(TR^-) = \frac{M_{0U}\left(1-e^{-TR/T1U}\right)}{\left(1-e^{-TR/T1U}\cos\alpha\right)}, \qquad [3.23]$$

where M_{0U} represents the equilibrium magnetization.

Eq [3.23] can be used to estimate the amount of T_1 attenuation for a given GRE protocol. Assuming a T_1 of approximately 1 s for grey matter at 1.5 T, for a sequence with a TR=20 ms, a signal attenuation of approximately 16% is expected even for values of α as small as 5°.

Since the measured signal intensity is proportional to the transverse magnetization (M_{xy}) at the echo time, in the steady state:

$$SI \propto M_{xy}(TE) = M_z(TR^-)e^{-TE/T_2^*}\sin\alpha, \qquad [3.24]$$

Giving (neglecting T_2* decay, for sufficiently short TEs):

$$SI \propto \frac{M_{0U}\left(1-e^{-TR/T1U}\right)}{\left(1-e^{-TR/T1U}\cos\alpha\right)}\sin\alpha. \qquad [3.25]$$

During CW off-resonance irradiation, the signal intensity has a similar dependence on acquisition parameters:

$$SI \propto \frac{M_{0S}\left(1-e^{-TR/T1S}\right)}{\left(1-e^{-TR/T1S}\cos\alpha\right)}\sin\alpha, \qquad [3.26]$$

where $M_{0S}<M_{0U}$ represents the equilibrium magnetization in the presence of MT saturation, and $T_1^S<T_1^U$(Hajnal et al., 1992).

Eq [3.26] is not strictly valid when pulsed MT is used; in such circumstances more accurate models have been developed (Pike, 1996). However no simple expression can be derived to describe the behaviour of the system, and to estimate the effects of this phenomenon on MTR. If the duration of the MT pulse is a significant proportion of *TR*, Eq [3.26] can be considered a good approximation, and attempts to measure T_1^S have been made based on it (Finelli et al., 1998), showing good agreement between the model and the data. Here I adopt Eq. [3.26] as a valid model to evaluate the effects of T_1-weighting on MTR calculation in vivo and in a gelatine phantom.

3.2.2 Methods

3.2.2.1 MRI acquisition

A 3D fast spoiled GRE pulse sequence was used for collecting data on a 1.5 T system (General Electric, Milwaukee, WI) on a healthy subject (male, age: 32 years) and in a phantom consisting of three identical plastic vials, one containing water, and two containing a 20% gelatine solution (300 g gelatine+1.5 g sodium azide + 1.5 L water) (Silver, 2001). The vials were fixed within a polystyrene disc,

designed to fit into the 8 channel receiver coil used for the experiment. The pulse sequence collects serially a volume with MT saturation (Gaussian 7.3 ms wide pulses, FWHM = 1.76 ms, offset frequency = 2 kHz) and a volume without saturation. The amplitude of the saturating field can be specified in terms of its equivalent on-resonance flip angle (see section 3.1.2.3). In this case, a flip angle of 700° was used. The maximum B_1 amplitude achievable on the scanner is 0.146 G, or 0.0146 mT.

The acquisition parameters were as follows: TE=5.1 ms, TR=21.6 ms (in vivo) and TR=25.2 ms (phantom). The use of larger imaging flip angles in the phantom (see below) resulted in the use of longer TR in order to maintain the experiment within the SAR limits imposed by the manufacturer. A matrix of 256x128x32 over a FoV of 24x18x16 cm^3 was used in vivo. The raw data were used to reconstruct twenty-eight 5 mm thick axial slices with an in plane resolution of 256^2 over 24^2 cm^2. For the phantom, only 16 slice locations were used (12 reconstructed slices) with the same slice thickness and identical in plane parameters as the *in vivo* acquisition.

The acquisition was repeated several times varying the excitation flip angle (but keeping constant transmitter and receiver gain). *In vivo*, it was repeated 13 times (flip angles: 5°, 8°, 10°, 12°, 14°, 16°, 18°, 20°, 22°, 24°, 26°, 30°, 35°), while in the phantom it was repeated 21 times (flip angles: 2°, 5°, 8°, 10°, 12°, 14°, 16°, 18°, 20°, 22°, 24°, 26°, 28°, 31°, 34°, 37°, 40°, 45°, 50°, 55°, 60°).

3.2.2.2 Image post-processing

The images obtained *in vivo* were co-registered to correct for involuntary between-scan motion, using a modified (Symms et al., 2003) version of AIR (Automated Image Registration, available at http://air.bmap.ucla.edu:16080/AIR) (Woods et al., 1998).

Two regions of interest (ROIs) were positioned in the splenium of the corpus callosum (representative of white matter) and in the caudate nucleus (representative of grey matter), and the average signal intensity was obtained for all the 13 unsaturated images (MTOFF) and the 13 saturated images (MTON).

An elliptical ROI was drawn in the middle slice of the series obtained from the phantom, centred within one of the vials containing gelatine, and the signal intensity was obtained for the 21 MTOFF images and the 21 MTON images.

Eq [3.25] was linearly fitted to the set of measurements obtained from the MTOFF images, after dividing both sides by sin(α) (Ernst and Anderson, 1966), leading to estimates of M_{0U} (multiplied by an arbitrary gain factor, k) and T_1^U for gelatine, white matter and grey matter. Eq [3.26] was fitted in the same fashion to the set of measurements obtained from the MTON images, providing M_{0S} (multiplied by the same gain factor k) and T_1^S for the 3 samples.

3.2.3 Results

3.2.3.1 Phantom data

Table 3.1 summarises the parameters estimated in gelatine.

Table 3.1. Model parameters estimated in the phantom.

MTOFF	MTON
$kM_{0U} = 5595.4$	$kM_{0S} = 3289.5$
$T_1^U = 875.1$ ms	$T_1^S = 535.2$ ms

The values were obtained by fitting Eq [3.25] and Eq [3.26] to the data, as explained in the text. k is a constant instrumental gain factor.

Fig 3.3 represents the measured signal intensity on saturated (circles) and unsaturated (squares) images, together with the fitting curves. Fig 3.4 represents the MTR calculated from the measured data, and from the fitting curves. Consistent with previous observations (Finelli et al., 1998), the MTR decreases as the imaging flip angle increases.

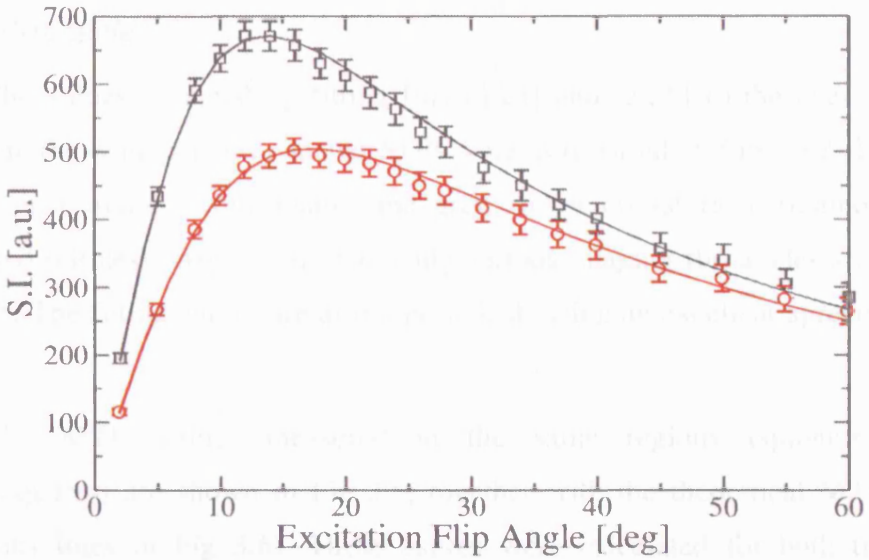

Fig 3.3. Mean MT-weighted (red circles) and MT-unweighted (black squares) signal measured in gelatine together with fitting curves.

The error bars represent the standard deviation of signal intensity within the region of interest.

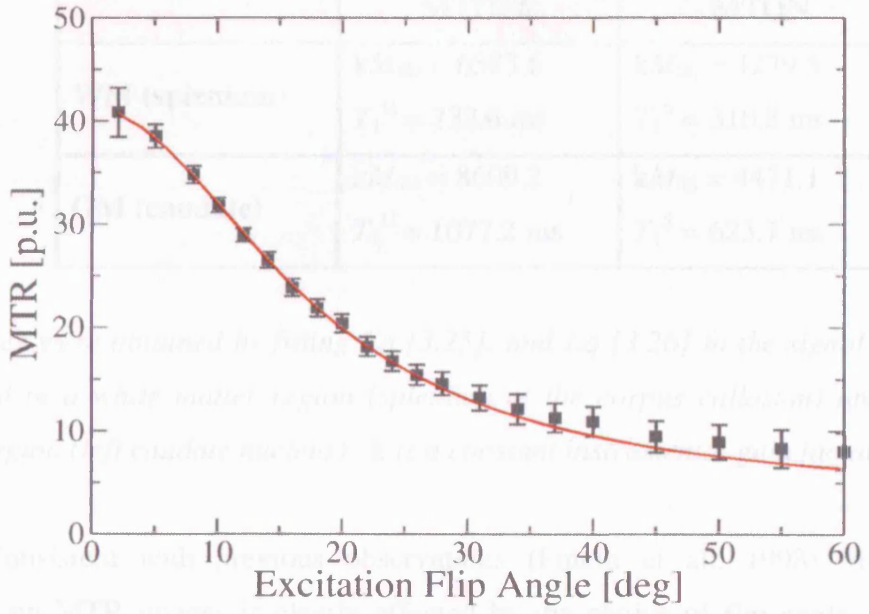

Fig 3.4 Mean MTR as a function of the excitation flip angle in gelatine

The error bars represent the standard deviation within the region of interest. The fitting line (red) was obtained by substituting the values reported in Table 3.1 into Eqs [3.25] and [3.26], and then calculating the MTR as a percentage ($MTR=100\times(M_{0U}-M_{0S})/M_{0U}$).

3.2.3.2 In vivo data

The values obtained by fitting Eqs [3.25] and [3.26] to the average signal intensity in the white and grey matter ROIs were as reported in Table 3.2. The signal intensity measured in white matter and grey matter on saturated (diamonds) and unsaturated (circles) images collected using various imaging flip angles are reported in Fig 3.5. The fitting curves are also reported, showing an excellent agreement with the data.

The MTR values measured in the same regions (splenium=circles, caudate=squares) are shown in Fig 3.6, together with the theoretical MTR curves (continuous lines in Fig 3.6). These curves were calculated for both tissues by substituting in the MTR equation (Eq [3.22]) the values obtained from Eq [3.25] and Eq [3.26] over values of α ranging from 2° to 40°.

Table 3.2. Model parameters estimated in white matter and grey matter.

	MTOFF	MTON
WM (splenium)	$kM_{0U} = 6583.6$ $T_1^U = 732.6$ ms	$kM_{0S} = 4279.5$ $T_1^S = 310.8$ ms
GM (caudate)	$kM_{0U} = 8609.2$ $T_1^U = 1077.2$ ms	$kM_{0S} = 4471.1$ $T_1^S = 623.7$ ms

The values were obtained by fitting Eq [3.25], and Eq [3.26] to the signal intensity measured in a white matter region (splenium of the corpus callosum) and a grey matter region (left caudate nucleus). k *is a constant instrumental gain factor.*

Consistent with previous observations (Finelli et al., 1998), the signal intensity on MTR images is clearly affected by the choice of flip angle, as is the white-to-grey matter contrast, estimated as the difference between the MTR in white matter and the MTR in grey matter (Fig 3.7). In particular, MTR decreases as the imaging flip angle increases, while the grey-to-white matter contrast achieves a maximum at around 15-25°, followed by a decrease.

The implications of these results on MTR maps can be appreciated qualitatively on the images shown in Fig 3.8. These images were obtained by processing 6 pairs of saturated and unsaturated images obtained with flip angles 2°, 5°, 12°, 20°, 26°, 35°, respectively.

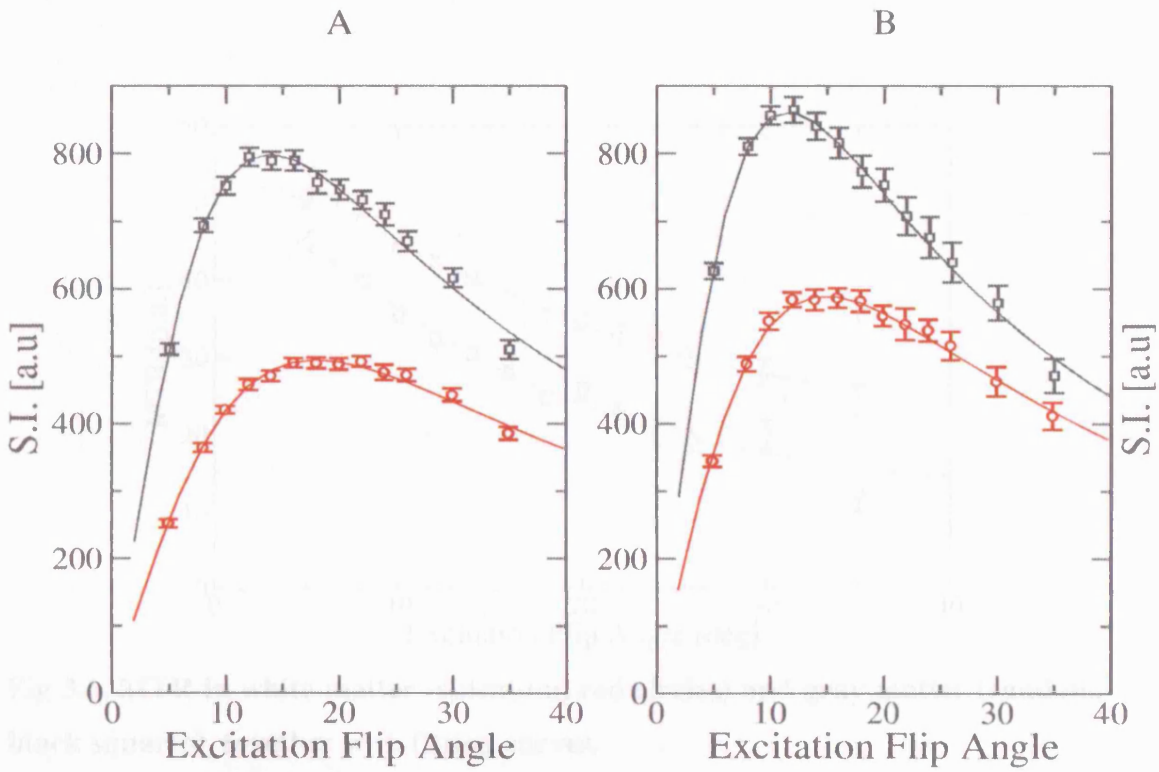

Fig 3.5. Mean signal measured on unsaturated images (black squares) and on saturated images (red circles) in white matter (A) and grey matter (B), on images obtained using different imaging flip angles.

The fitting curves were obtained by substituting the values reported in Table 3.2 into Eqs [3.25]-[3.26]. The error bars indicate the standard deviation within the region of interest.

Quantitatively, it is relevant to compare the expected change in MTR due to reduced competition with T_1 recovery (genuine MT effect) with the apparent change in MTR due solely to T_1-weighting when T_1 increases by, say, 1%. For the acquisition parameters described above and typical white matter parameters at 1.5 T (see section 3.3), the Henkelman model predicts that a 1% increase in T_1^U (and consequent change in T_1^S) should result in approximately a 0.5% genuine change in MTR. For an imaging flip angle of 10°, assuming the same 1% change and using the

T_1^U and T_1^S values estimated above for white matter, Eq. [3.25] and [3.26] predict a change of approximately 0.25% in the measured MTR (Eq. [3.22]) due solely to the change in T_1-weighting of the underlying images. This change (up to half of the genuine change) is reduced to 0.07% (less than one sixth of the genuine effect) at an imaging flip angle of 5°.

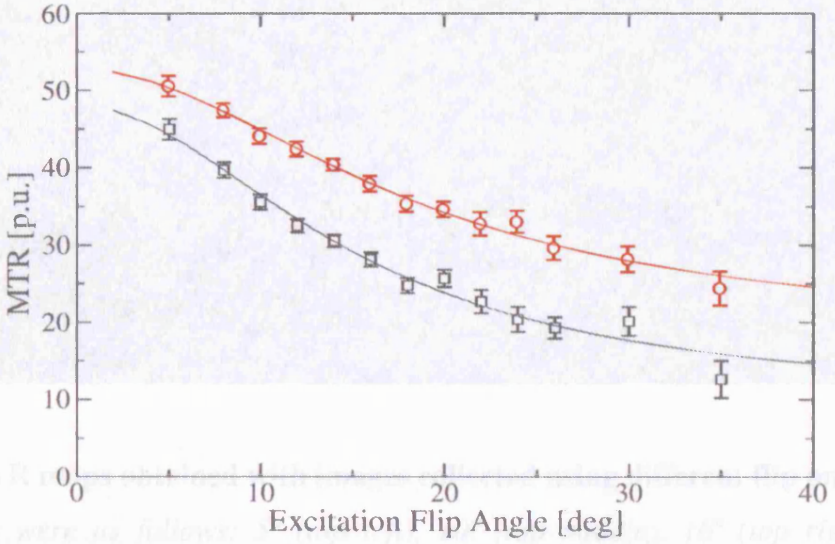

Fig 3.6. MTR in white matter (splenium, red circles) and gray matter (caudate, black squares), together with fitting curves.

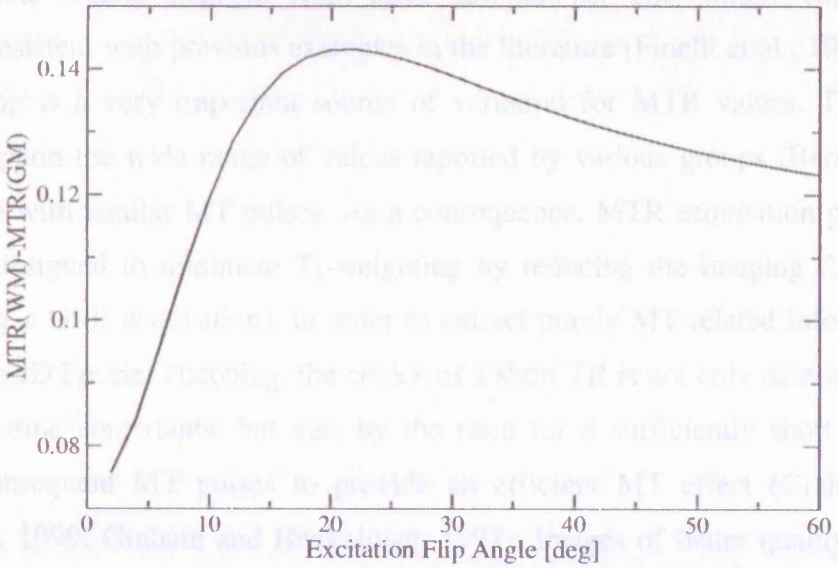

Fig 3.7 Theoretical white-to-grey matter contrast as a function of the imaging flip angle.

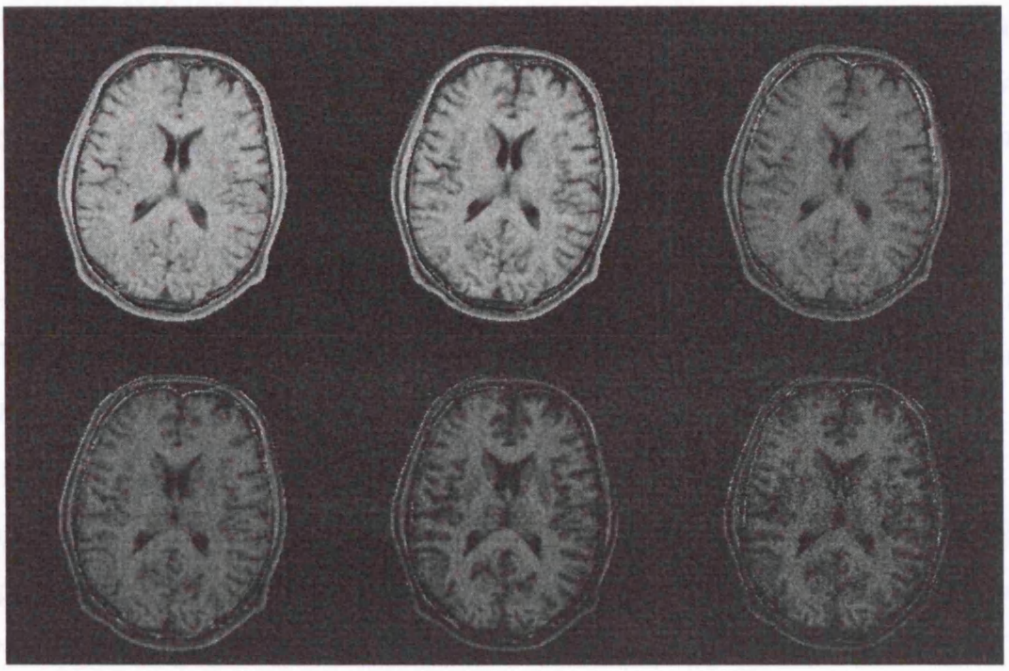

Fig 3.8. MTR maps obtained with images collected using different flip angles. *Flip angles were as follows: 5° (top left), 10° (top middle), 16° (top right), 20° (bottom left), 26° (bottom middle), 35° (bottom right).*

3.2.4 Discussion

Several results emerged from these simulations. This simple experiment showed, consistent with previous examples in the literature (Finelli et al., 1998), that T_1 weighting is a very important source of variation for MTR values. This may partially explain the wide range of values reported by various groups (Berry et al., 1999), even with similar MT pulses. As a consequence, MTR acquisition protocols should be designed to minimize T_1-weighting by reducing the imaging flip angle (when using a GRE acquisition), in order to extract purely MT-related information. When using 3D Fourier encoding, the choice of a short TR is not only determined by acquisition time constraints, but also by the need for a sufficiently short interval between subsequent MT pulses to provide an efficient MT effect (Graham and Henkelman, 1999; Graham and Henkelman, 1997). Images of better quality can be obtained when using higher imaging flip angles. However, in such images the contrast is the result of a complex interaction between MT saturation and T_1

recovery, with T_1-weighting having an undefined contribution (which is not accounted for in Eq [3.10]) to any observed change. It could be argued that an "optimal" choice of imaging flip angle should maximize both contrast and signal by exploiting this effect, rather than minimizing it, and if this is the desired endpoint then Figure 3.7 (or its equivalent for other field strengths) can be used to determine this value. This is likely to result in improved sensitivity to white matter changes, but would make the interpretation of MTR abnormalities much more complex. It has already been observed (Henkelman et al., 2001) that correlations between T_1 and MTR often observed in pathological tissues might be merely the result of direct saturation and T_1-weighted acquisitions.

Equation [3.26] is strictly valid only during CW irradiation, and therefore the values of T_1^S obtained by fitting Eq [3.26] to the data do not have a direct biological or physical meaning. Nevertheless, the equation proved to be a sufficiently good approximation of T_1-weighting effect on the apparent MTR, as demonstrated by the quality of the fitting (Figs 3.3-3.6).

3.3 Experiment B: Optimization of MTR acquisition at 1.5 T and at 3.0 T

3.3.1 Background

The MTR value observed *in vivo* in most clinical MT sequences is the result of the combination of several more fundamental quantities, and it is highly dependent on the acquisition parameters. For this reason a wide range of MTR values has been reported in the literature, and there is a need for standardisation (Berry et al., 1999). Furthermore, while the use of increased field strength would provide benefits for MT imaging in terms of signal to noise ratio (SNR), safety issues associated with the deposition of radio-frequency energy into the patient, measured by the specific absorption rate (SAR), have so far limited the use of MTR at field strengths greater than 1.5 T. Preliminary reports suggest that the grey-to-white matter contrast on MTR maps increases with field strength (Duvurri et al., 1990). It would therefore be desirable to design a suitable protocol for MTR acquisition at high field. Assuming that the MT effect can be characterized using a two-pool model (Henkelman et al., 1993), signal behaviour can be predicted as a function of a set of parameters, which

can be optimized for a given application (Graham and Henkelman, 1999). Here I analyze quantitatively the white-to-grey matter contrast to noise ratio (CNR) and compare its dependency on the characteristics of the saturating pulse at 1.5 T and 3.0 T. The two parameters that mainly affect the resulting MTR are the amplitude of the saturating pulse (ω_1), i.e. the angular frequency of precession induced by the pulse, and its offset frequency (Δf), which are constrained by scanner and subject related considerations. These two parameters must be chosen under these constraints, and that of minimal direct effect (i.e. the direct saturation of the liquid pool in the absence of exchange due to off-resonance irradiation). As the values of the parameters of the two-pool model at both field strengths are needed for the optimisation, a series of measurements was first performed to estimate these quantities. Next, I used these quantities to estimate the values of ω_1 and Δf that maximize the CNR. The optimal values are chosen under safety constraints and used to set up an acquisition protocol for clinical MTR acquisition at 3.0 T. The images obtained at 3.0 T are compared to those obtained at 1.5 T, and the advantages and limitations of the use of higher field strengths are discussed.

3.3.2 Theory

For the following analysis, Henkelman's two-pool model was used (Eq [3.10]), R_{RFB} was modeled with a super-Lorentzian lineshape, and Ramani's CW approximation was used to allow for the use of pulsed MT (Ramani et al., 2002).

When fitting this model directly to the measured signal intensity, a factor gM_0 must be explicitly taken into account to keep the correct dimensionality (Ramani et al., 2002), giving:

$$SI_{MT} = gM_0 \frac{R_B\left[\frac{RM_0^B}{R_A}\right] + R_{RFB} + R_B + RM_0^A}{\left[\frac{RM_0^B}{R_A}\right](R_B + R_{RFB}) + \left(1 + \left[\frac{\omega_1}{2\pi\Delta f}\right]^2\left[\frac{1}{R_A T_2^A}\right]\right)(R_{RFB} + R_B + RM_0^A)} \quad [3.27]$$

Out of the 8 fundamental quantities appearing in Eq [3.27], only 6 parameters (RM_0^A, RM_0^B/R_A, gM_0, $1/R_A T_2^A$, R_B, and T_2^B) can be estimated independently by non-

linear fitting. R_B is generally kept fixed (Henkelman et al., 1993; Ramani et al., 2002; Sled and Pike, 2001; Tozer et al., 2003), mainly due to its tendency to vary widely during the fitting procedure, leading to physically meaningless estimates. This choice is justified by the observation that the estimates of the other parameters are largely insensitive to the value of R_B. Knowledge of the model parameters allows the signal intensity to be estimated for any given combination of ω_1 and Δf. The reader is referred to Chapter 4 for more details on quantitative MT.

3.3.3 Methods

3.3.3.1 MR image acquisition

Three healthy subjects (2 male, 1 female, mean age 34.3 years, range 32-38 years) took part in the study after giving written informed consent.

Every subject was scanned on two different scanners from the same manufacturer (General Electric, Milwaukee, WI) - one 1.5 T and one 3.0 T (software versions 11x and G3M4 respectively) - using a 3D MT-weighted spoiled GRE pulse sequence. The parameters used on the two systems were chosen to be as similar as possible, and are reported in Table 3.3. At 3.0 T, a larger bandwidth/pixel (resulting in both a shorter echo time and a slightly shorter repetition time) was used to minimize susceptibility effects. An excitation flip angle of 5° was used in order to minimize the degree of T_1-weighting (which is not accounted for by Eq [3.27]). The same Gaussian MT pulses used for the experiments described in section 3.2 were used (τ_{SAT}=7.3 ms). On both scanners, the manufacturer's body coil was used for transmission, and their 8 channel head coil was used for reception. Two MT pulse flip angles were used on each scanner (150° and 450°), with 5 offset frequencies per flip angle (1, 2, 4, 7, and 15 kHz), giving ten datasets with different combinations of MT pulse amplitude and offset frequencies in total. For all datasets forty-eight 3 mm thick axial slices were reconstructed with an in-plane matrix of 256x256 over a 24x24cm FoV.

The SAR was estimated during scan setup, using the manufacturer's standard calculation routines, assuming a 'worst case scenario' of MT pulses with the maximum flip angle for all measurements; in no cases were the SAR limits reached or exceeded. (Runtime hardware SAR monitoring is also provided as standard, for all sequences, by both scanners).

Table 3.3. Acquisition parameters for MTR on the two MRI scanners.

	1.5 T system	3.0 T system
TE	5.2 ms	3.2 ms
TR	20.7 ms	20.0 ms
Imaging flip angle	5°	5°
matrix	256x144x52	256x144x52
FoV	24x18x14.4cm^3	24x18x14.4cm^3
MT pulse flip angles	150°, 450°	150°, 450°
CWPE	259 rads^{-1}, 777 rad s^{-1}	264 rads^{-1}, 790 rad s^{-1}

A total of 10 combinations of MT powers and offset frequencies were employed, using 2 MT pulse flip angles (whose equivalent continuous wave amplitude, CWPE, is also reported in the table), and 5 offset frequency values per flip angle (see text).

3.3.3.2 MR image post-processing

The analysis of the 3.0 T and 1.5 T data was performed using the same procedure. After image co-registration (Symms et al., 2003; Woods et al., 1998), four white matter regions (genu and splenium of the corpus callosum, left and right anterior perventricular areas) and four grey matter regions (caudate nucleus and putamen, bilaterally) were outlined on the unsaturated images, as shown in Fig 3.9, and their average values measured on each image.

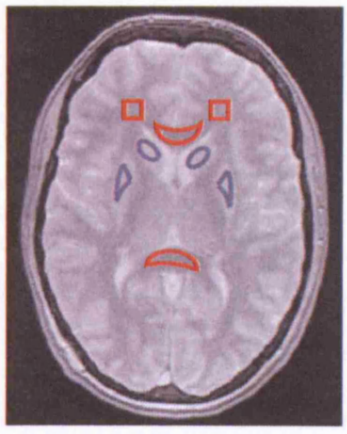

Fig 3.9. Position of the grey matter (blue) and white matter (red) ROIs.

Model parameters were estimated by fitting Eq. [3.27] to the data, using the Levenberg-Marquardt method (Press et al., 1992). R_B was set arbitrarily to 1 s^{-1} (Henkelman et al., 1993; Ramani et al., 2002; Sled and Pike, 2001; Tozer et al., 2003). The average MT parameters across subjects were estimated and are reported in Table 3.4. For the purpose of optimizing white-to-grey matter contrast, a set of representative parameters were obtained for each tissue class by averaging the parameters obtained for the different ROIs (see Table 3.4).

3.3.3.3 Optimisation of white-to-grey matter contrast

The white-to-grey matter contrast ($C_{wm\text{-}gm}$) was calculated as the difference in white matter and grey matter MTR value estimated according to Eq [3.22], using the mean parameters obtained for each tissue with the previous analysis.

Since the choice of ω_1 and Δf also affects the signal-to-noise ratio of the calculated MTR maps, the propagation of error equation (Bevington and Robinson, 1969) was used to estimate the variance of signal on MTR maps, relative to the variance of the collected images:

$$\mathrm{var}_{MTR} = \sigma^2\left[\left(\frac{\partial MTR}{\partial M_0}\right)^2 + \left(\frac{\partial MTR}{\partial M_s}\right)^2\right] = \sigma^2\left[\left(-\frac{1}{M_0}\right)^2 + \left(\frac{M_s}{M_0^{\,2}}\right)^2\right] \qquad [3.28]$$

In Eq [3.28] σ is the SD of noise in the acquired data, which I assume to be independent of ω_1 and Δf, and depends only on other (fixed) parameters such as voxel size and receive bandwidth. Assuming the same (minimal) amount of T_1-weighting in the two images, and g=1, I can set $M_s = SI_{MT}$, and substitute Eq [3.27] into Eq [3.28], giving:

$$\mathrm{var}_{MTR} = \sigma^2\left[\left(-\frac{1}{M_0}\right)^2 + \right.$$

$$\left. + \left(\frac{1}{M_0}\,\frac{R_B\left[\frac{RM_0^B}{R_A}\right] + R_{RFB} + R_B + RM_0^A}{\left[\frac{RM_0^B}{R_A}\right](R_B + R_{RFB}) + \left(1 + \left[\frac{\omega_1}{2\pi\Delta f}\right]^2\left[\frac{1}{R_A T_2^A}\right]\right)(R_{RFB} + R_B + RM_0^A)}\right)^2\right] \qquad [3.29]$$

If the parameters of the Henkelman's model are known, the variance of the MTR measurement can be expressed as a function of ω_1 and Δf.

The contrast-to-noise ratio (CNR) can then be calculated as

$$CNR(\omega,\Delta f)=\frac{C_{wm-gm}(\omega_1,\Delta f)}{\frac{1}{2}\sqrt{\mathrm{var}_{MTR}(\omega_1,\Delta f)}\Big|_{gm}+\frac{1}{2}\sqrt{\mathrm{var}_{MTR}(\omega_1,\Delta f)}\Big|_{wm}}, \qquad [3.30]$$

where the denominator represents the standard deviation (SD) of the measurement estimated as the average of white matter and grey matter SDs. Eq [3.30] was plotted for various values of ω_1 and Δf (setting the arbitrary multiplicative scaling factor, $\frac{\sigma}{\sqrt{M_0}}=\sigma_n$, representing the protocol dependant actual SNR of the acquired images, to 1) in order to extrapolate the values maximising the grey-to-white matter CNR.

In order to minimise the direct effect (Henkelman et al., 1993), i.e. direct saturation of the free pool in the absence of exchange, I imposed an arbitrary threshold (15% of total signal) on the amount of direct effect allowed. R_A was approximated using the observed R_1 ($=1/T_1^U$), calculated from the 1.5 T data described above (R_A=1.37 s^{-1} in white matter and R_A=0.92 s^{-1} in grey matter), and measured by others (Clare and Jezzard, 2001) for the 3.0 T data (R_A=1.1 s^{-1} in white matter and R_A=0.83 s^{-1} in grey matter).

An additional requirement for the selection of the optimal combination of power and frequency was that its use did not violate SAR limitations. As the procedures for estimating SAR are not easily invertible, the maximum safe amplitude at both field strengths was empirically determined by entering a range of possible values of the MT flip angle into the manufacturer provided SAR calculation software and noting when SAR limits would be approached. This happened at an amplitude corresponding to approximately 940 $rads^{-1}$ (flip angle = 550°) at 1.5 T, and at approximately 790 $rads^{-1}$ (flip angle = 450°) at 3.0 T, assuming a (minimum) subject weight of 50 Kg. The small difference between the two values was surprising, as the SAR is expected to scale approximately with the square of the field strength. However, the models used to calculate the effects of RF power deposition and dissipation are constantly being refined, and the scanners' calculated SAR limits are therefore dependent on the specific software release being run.

3.3.4 Results

3.3.4.1 MT parameters at 1.5 T and 3.0 T

The mean MT parameters and their standard error calculated over the ROIs are reported in Table 3.4.

3.3.4.2 Optimal acquisition parameters at 1.5 T

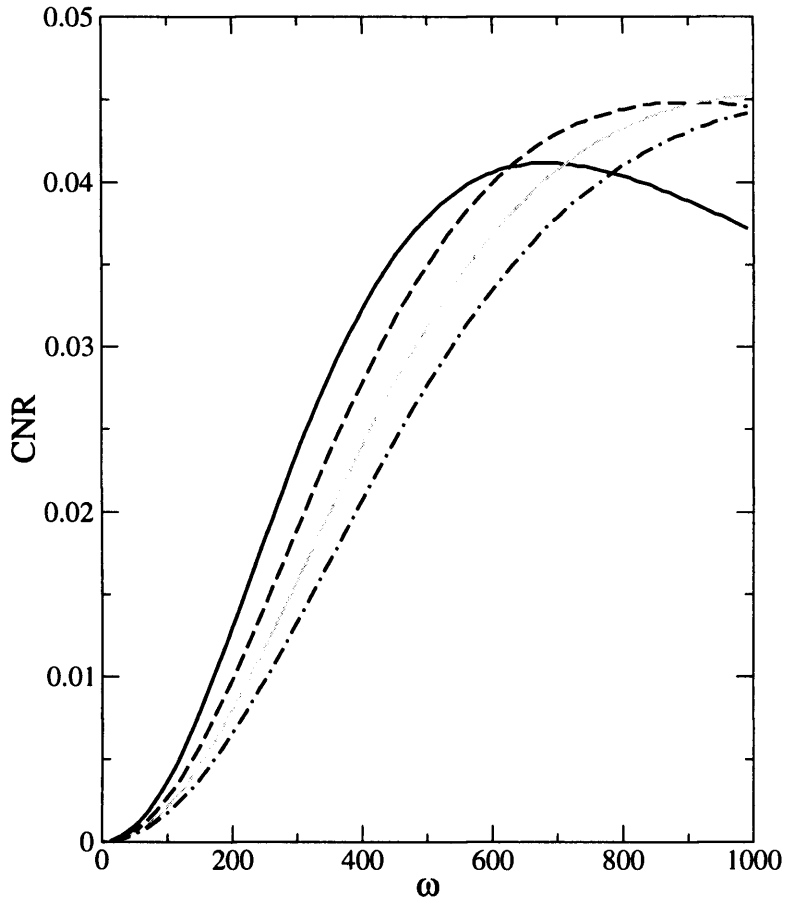

Fig 3.10. White-to-grey matter CNR vs. MT continuous wave power equivalent, at 1.5 T.

The curves are for Δf=1 kHz (black continuous line), Δf=2 kHz (dashed line), Δ=3 kHz (grey line), and Δf=4 kHz (dashed-dotted line).

Fig 3.10 shows the estimated CNR at 1.5 T as a function of ω_1, for 4 values of Δf. I only considered the range [0, 1000 rads^{-1}] as higher amplitudes would be unsafe *in vivo*.

Within this range, the absolute maximum (CNR=0.0452/σ_n) occurs at ω_1=990 rad/sec, for Δf=3 kHz. A pulse with such amplitude is unfortunately above the limit imposed by safety considerations (see 3.3.2) and therefore I considered the next CNR maximum (CNR = 0.0448/σ_n), obtained at ω_1=900 rad/sec, for Δf=2 kHz. With these parameters, the direct effect is approximately MT_{dir} =0.9 for both tissues, giving an attenuation of 10%. Using the MT pulse and TR described above, ω_1=900 rads^{-1} corresponds to an equivalent on-resonance flip angle of approximately 530°.

Within this range, the absolute maximum (CNR=0.0452/σ_n) occurs at ω_1=990 rad/sec, for Δf=3 kHz. A pulse with such amplitude is unfortunately above the limit imposed by safety considerations (see 3.3.2) and therefore I considered the next CNR maximum (CNR = 0.0448/σ_n), obtained at ω_1=900 rad/sec, for Δf=2 kHz. With these parameters, the direct effect is approximately MT_{dir} =0.9 for both tissues, giving an attenuation of 10%. Using the MT pulse and TR described above, ω_1=900 rads^{-1} corresponds to an equivalent on-resonance flip angle of approximately 530°.

Table 3.4. The mean (standard error) values obtained in white matter and grey matter.

	1.5 T					3.0 T				
Region	**RM_0^A**	**RM_0^B/R_A**	**T_2^B**	**$1/(R_AT_2^A)$**	**$M_0^{A(*)}$**	**RM_0^A**	**RM_0^B/R_A**	**T_2^B**	**$1/(R_AT_2^A)$**	**$M_0^{A(*)}$**
CC spl	25.49 (0.13)	2.03 (0.13)	8.70 (0.34)	24.87 (2.19)	0.87 (0.04)	15.18 (0.17)	2.26 (0.08)	9.23 (0.16)	45.90 (3.52)	1.01 (0.04)
CCge	38.17 (11.6)	2.75 (0.66)	8.12 (0.34)	21.21 (3.94)	0.93 (0.01)	20.02 (1.44)	2.40 (0.09)	8.24 (0.09)	47.32 (2.54)	0.97 (0.04)
Ant PVL	41.32 (12.91)	2.63 (0.63)	8.48 (0.24)	20.96 (4.52)	1.07 (0.05)	24.12 (2.05)	2.28 (0.12)	9.15 (0.19)	40.33 (2.46)	1.02 (0.04)
Ant PVR	33.37 (8.4)	2.22 (0.42)	8.55 (0.36)	24.53 (3.65)	(0.07)	23.95 (1.23)	2.25 (0.08)	8.68 (0.04)	39.87 (2.49)	0.99 (0.03)
putL	33.54 (6.2)	1.91 (0.21)	7.92 (0.14)	20.94 (2.93)	1.03 (0.03)	22.68 (3.14)	1.78 (0.15)	8.25 (0.04)	38.95 (2.05)	1.10 (0.05)
putR	33.06 (4.5)	1.85 (0.21)	8.18 (0.38)	22.54 (1.92)	1.06 (0.01)	19.55 (1.79)	1.63 (0.04)	8.64 (0.24)	36.67 (2.44)	1.10 (0.05)
cauL	35.14 (7.42)	2.21 (0.46)	7.73 (0.34)	21.34 (2.16)	1.13 (0.02)	22.17 (0.70)	1.67 (0.11)	7.84 (0.08)	37.23 (0.83)	1.09 (0.05)
cauR	43.65 (11.55)	2.21 (0.47)	7.86 (0.31)	19.94 (3.03)	1.09 (0.03)	23.22 (2.12)	1.66 (0.11)	7.75 (0.20)	37.10 (1.00)	1.09 (0.05)
WM	**34.59 (4.30)**	**2.41 (0.22)**	**8.46 (0.15)**	**22.89 (1.59)**	**1.0 (0.03)**	**20.82 (1.25)**	**2.30 (0.04)**	**8.83 (0.13)**	**43.35 (1.55)**	**1.0 (0.02)**
GM	**36.35 (3.44)**	**2.02 (0.15)**	**7.93 (0.13)**	**21.19 (1.07)**	**1.08 (0.01)**	**21.9 (1.00)**	**1.69 (0.05)**	**8.12 (0.13)**	**37.49 (0.78)**	**1.09 (0.02)**

These values were obtained by averaging across 3 subjects in 4 white matter regions (CCspl=splenium of corpus callosum, CCge = genu of corpus callosum, antPVL = left anterior periventricular areas, antPVR = right anterior periventricular areas) and 4 grey matter regions (putL = left putamen, putR = right putamen, cauL = left caudate, cauR = right caudate). The mean white matter (WM) and grey matter (GM) values were obtained by averaging regional parameters.

RM_0^A is expressed in units of sec^{-1}, T_2^B is expressed in units of μsec, all other parameters are dimensionless.

See text for further details.

(*) M_0^A is normalized with respect to the average white matter value.

3.3.4.3 Optimal acquisition parameters at 3.0 T

Fig 3.11 shows the estimated CNR at 3.0 T as a function of ω_1. The CNR appears higher than at 1.5 T, with three curves having similar maxima ($\approx 0.07/\sigma_n$) at, respectively, [ω_1 =780 rads^{-1}, Δf = 2 kHz], [ω_1 =940 rads^{-1}, Δf = 3 kHz] and [ω_1 =1080 rads^{-1}, Δf = 4 kHz]. According to my empirical estimates, short pulses with ω_1 > 790 rads^{-1} violate the SAR limitations. As a consequence, I determined the "best-and-safe" combination of power and offset frequency to be ω_1=780 rads^{-1} (corresponding to an equivalent on-resonance flip angle of 430°), Δf = 2 kHz.

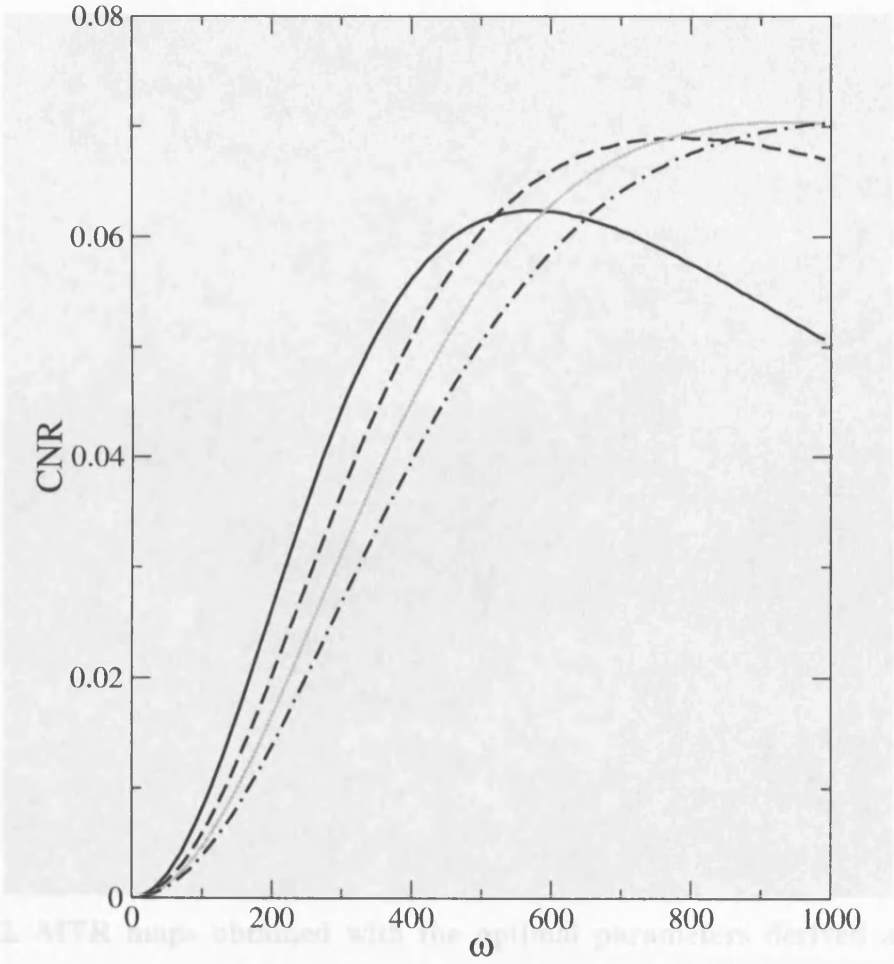

Fig 3.11. White-to-grey matter CNR vs. MT continuous wave power equivalent, at 3.0 T.

The same values of Δf used at 1.5 T were considered: 1 kHz (black continuous), 2 kHz (dashed black), 3 kHz (grey) and 4kHz (dashed-dotted). A) The maximum CNR is reached at different powers for each offset frequency.

The direct effect for these parameter based on the values in Table 3.4 was approximately 0.86 in white matter and 0.87 in grey matter, giving a worst-case signal attenuation of 14%.

3.3.4.4 CNR-optimised MTR maps

Fig 3.12 shows MTR maps obtained from the same subject at 1.5 T (bottom row) and at 3.0 T (top row), using the optimal parameters (and other acquisition parameters as in Table 1). Both the SNR and the white-to-grey matter CNR appeared greatly increased in 3.0 T data throughout the brain.

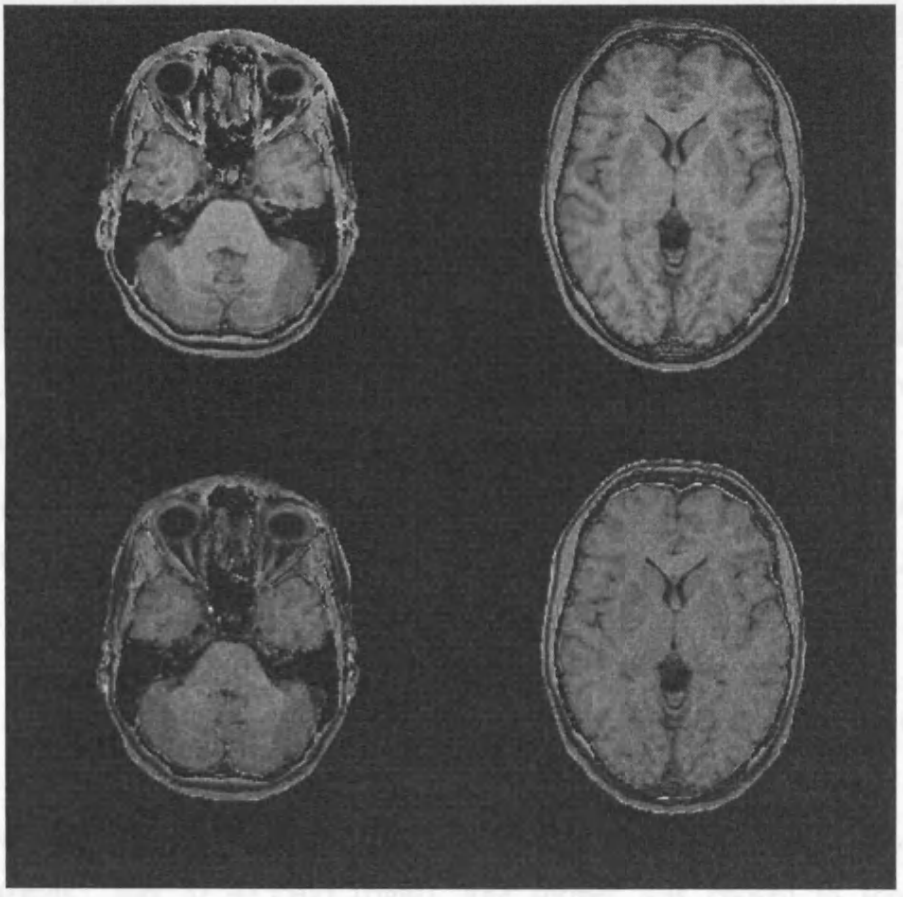

Fig 3.12. MTR maps obtained with the optimal parameters derived at 1.5 T (bottom) and 3.0 T (top).

Acquisition parameters were ω_1=900 rads^{-1} and Δf =2 kHz at 1.5 T; and ω_1=780 rads^{-1} and Δf =2 kHz at 3.0 T. Both the SNR and the grey-to-white matter contrast are increased at 3.0 T. See Table 3.3 for other acquisition parameters.

The mean white matter and grey matter MTR were obtained by averaging the signal measured on these maps in the same ROIs used to estimate the MT parameters. For the 1.5 T data, the average WM MTR was 0.48, and the average GM MTR was 0.43, giving a $C_{WM\text{-}GM} \approx 0.05$. For the 3.0 T data, the average WM MTR was 0.54, and the average GM MTR was 0.46 giving a $C_{WM\text{-}GM} \approx 0.08$. In order to calculate the CNR, an estimate of the standard deviation is needed. Such estimate is difficult to obtain from a single image. Nevertheless, as from Eq [3.29] I obtain $\sigma_n \leq SD_{MTR} \leq 2\sigma_n$, i.e. $(C_{WM\text{-}GM} / 2\sigma_n) \leq CNR \leq (C_{WM\text{-}GM} / \sigma_n)$, I can conclude that experimental results are in excellent agreement with those predicted by theory.

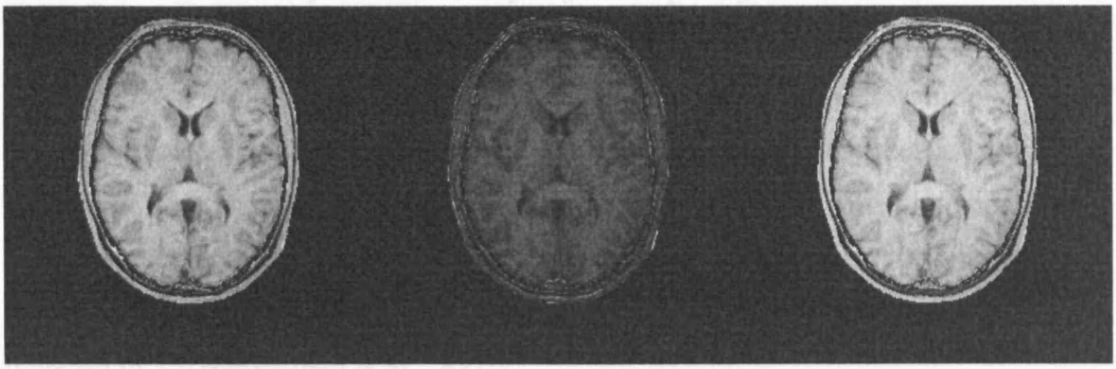

Fig 3.13. MTR maps obtained at 3.0 T from the same subject using different combinations of ω_1 and Δf.

The optimal combination (left) is compared to [ω_1=350 rads^{-1} and Δf =4 kHz] (centre), which gives poor SNR, and to [ω_1=780 rads^{-1} and Δf =1 kHz] (right), where the contrast is reduced due to direct effect.

For comparison purposes, a number of maps obtained at 3.0 T with sub-optimal combinations of parameters are also shown (Fig 3.13). The optimal combination (left) is compared to [ω_1=350 rads^{-1} and Δf =4 kHz] (centre), and to [ω_1=780 rads^{-1} and Δf =1 kHz] (right). The former was chosen to show how maximizing contrast without accounting for the effects of noise propagation results in MTR maps of poor quality, while the latter shows how the contrast is reduced by direct effect when the offset frequency is small. Quantitatively, for [ω_1=350 rads^{-1} and Δf =4 kHz] the average white matter and grey matter MTR were0.2 and 0.15, respectively, giving a white-to-grey matter contrast of 0.05; for [ω_1=780 rads^{-1} and

Δf =1 kHz], the average white and grey MTR were 0.63 and 0.57, respectively, resulting in a white-to-grey matter contrast of 0.06.

3.3.5 Discussion

I have shown that *in vivo* MTR is feasible at 3.0 T, leading to improved SNR and CNR, as demonstrated by Fig 3.12.

Several results emerged from these simulations. In order to simulate the CNR as a function of the MT pulse characteristics, I first estimated the parameters of Henkelman's model in white and grey matter. The average values obtained at 1.5 T are consistent with previously reported measurements (Ramani et al., 2002; Sled et al., 2004). Previous experiments on agar gel comparing measurements obtained at 0.6 T and 1.5 T (Henkelman et al., 1993) suggested that the exchange rate (R) is independent of field strength, and that the increased absolute MTR value with B_0 is due to diminished competition from T_1 recovery. This is a consequence of the fact that while the loss of longitudinal magnetization due to exchange is governed by the same pseudo-first order exchange rate (RM_0^B) at all field strengths, the rate of recovery of longitudinal magnetization decreases with field strength due to the increase in T_1 (Henkelman et al., 2001).

Against this background, the results obtained here might appear puzzling at first. Table 3.4 suggests a reduction of both RM_0^B/R_A and RM_0^A at 3.0 T. However, the more physically meaningful $RM_0^B/(RM_0^A R_A)$ ratio (RM_0^B/RM_0^A is often referred to as the size of the restricted pool (Sled and Pike, 2001)) obtained from the values estimated in my experiment are in keeping with previous observations, i.e. consistent with changes in R_A only. The measured signal is quite insensitive to variation in RM_0^A (Graham and Henkelman, 1997) and this parameter is therefore highly susceptible to noise. The change between the values measured at different field strength can be interpreted as a result of the increased SNR at 3.0 T and therefore of the improved accuracy at higher field strength.

The contrast between grey and white matter is also increased at 3.0 T, despite MT parameters being very similar at the 2 field strengths. The increase in MTR and the improved contrast obtained at 3.0 T compared to 1.5 T are consistent with previous results at high field (Duvurri et al., 1999) and can be understood considering again the interaction between MT effect and T_1 recovery: the increased

contrast is expected given the increased difference at higher field strength between the RM_0^B/R_A ratios (Henkelman et al., 2001) measured in white and grey matter. The quality of the MTR maps obtained at 3.0 T suggests that the implementation of MTR acquisitions at high field may prove useful for the study of white matter disease. These observations also explain the disappointing results obtained in terms of CNR at 1.5 T, implying that the typical values of R_A of grey and white matter at 1.5 T limit the sensitivity of MTR at this field strength. Alternative MT-related measures, which isolate MT effects from T_1 effects, have been proposed to overcome this problem (Portnoy and Stanistz, 2005).

Several limitations prevent the generalization of the MT parameters obtained from this study. Firstly, the parameters were measured from a small number of subjects. Secondly, no attempt was made to correct the nominal flip angle of the MT pulses for B_1 inhomogeneity (although the use of the body coil for transmission should provide a fairly uniform B_1 distribution over the field of view of interest). Despite these limitations, the values of the MT parameters obtained here should be sufficiently accurate for optimizing the CNR of MTR maps. Clearly, averaging the parameters measured at different brain locations is not ideal, as the standard errors reported for white and grey matter parameters in Table 3.4 reflect both measurement errors and the genuine variation of these parameters within the brain (Sled et al., 2004). Nevertheless, the goal was maximizing the overall contrast between 'bulk' grey and white matter for which I believe the choice of using the mean values to be most appropriate.

As stated previously, the MT model adopted for this paper is only an approximation when dealing with pulsed MT. More appropriate models have been developed (Graham and Henkelman, 1997; Pike, 1996), and it would be interesting to compare the results of these simulations with those obtained when using such models. Despite the use of a simplified model, however, the results of the simulations are in keeping with the white-to-grey matter contrast measured on experimental data. A further confirmation of the validity of the curves shown in Fig 3.11 is provided by the comparison of absolute MTR and white-to-grey matter contrast between the images in Fig 3.13. The combinations of ω_1 and Δf used to produce the central and right image were chosen to be suboptimal in two different

ways: the use of large Δf and small ω_1 results in poor SNR, while the use of small Δf and large ω_1 results in suboptimal contrast.

Figures 3.10 and 3.11 suggest that the CNR could be further increased by using larger values of ω_1 (not feasible for safety reasons), providing that Δf is also increased. This is likely to reflect the rapid increase of direct effect with MT pulse power. Since direct effect is virtually unavoidable, its presence must be tolerated to some degree. Recognizing the importance of distinguishing between "true" MT and direct saturation, I set an upper threshold for this contamination corresponding to an attenuation of 15% of the total signal. This is clearly an arbitrary criterion, and more elegant approaches can be adopted (Graham and Henkelman, 1997).

Here I have considered the optimization of white-to-grey matter CNR, in order to sensitize the acquisition to myelin content, but the dependency of MT on the acquisition parameters can be similarly exploited to maximize any desired contrast effect (Graham and Henkelman, 1999). When interested in specific pathological changes, the contrast between normal and pathological tissue could be maximized, after estimating the MT parameters of interest.

Although the results presented here are specific to the pulse sequence used for these experiments, the methodology is general and the same simulations can be applied to any acquisition sequence.

3.4 Summary

- T_1-weighting must be minimised by reducing the imaging flip angle (when using a GRE acquisition), in order to extract purely MT-related information. Images of better quality can be obtained with larger flip angles; however, in such images the contrast is the result of a complex interaction between MT saturation and T_1 recovery, with T_1-weighting having an undefined contribution to any observed change.
- Eq [3.25] is only an approximation when using pulsed-MT acquisition. Nevertheless, it proved to be a sufficiently good approximation of T_1-weighting effect on the apparent MTR, as demonstrated by the quality of the fitting.

- In vivo MTR is feasible at 3.0 T within safety limits. The contrast between grey and white matter is increased at 3.0 T, despite MT parameters being very similar at the two field strengths. The increase in MTR and the improved contrast obtained at 3.0 T compared to 1.5 T data are consistent with previous results at high field.
- The dependency of MT on the acquisition parameters can be exploited to maximize the CNR, or any desired effect. Although the results here presented are specific to the pulse sequence used for these experiments, the methodology is general and the same simulations can be used with any acquisition sequence.

Chapter 4

Quantitative Magnetization Transfer

Introduction

Quantitative magnetization transfer analysis is based on a two-pool model of magnetization transfer and allows important physical properties of the two proton pools to be assessed. Indices derived from quantitative MT (qMT) are believed to reflect the degree of myelination in white matter, and the application of qMT *in vivo* has been pursued by several authors (Ramani et al., 2002; Sled and Pike, 2001; Tozer et al., 2003, Sled et al., 2004; Yarnyck, 2002) in healthy subjects (Sled et al., 2004), in patients with multiple sclerosis (Davies et al., 2004), and in patients with tumours (Yarnyck, 2002).

In this chapter, I first summarize the theory behind the model of MT used for the experiments here described (4.1.1). Next, I use Monte Carlo simulations to measure the error in the MT parameters estimated at various noise levels (4.1.2-4.1.4), demonstrating the need for high SNR in the acquired data. I then describe clinically feasible protocols for measuring MT parameters at 1.5 T (4.2) and 3.0 T (4.3) providing normative data at both field strengths. Finally, I investigate the use of the Cramer-Rao lower bound (CRLB) theory to optimise sampling strategies for quantitative MT (4.4). Further possible improvements to image acquisition and post-processing are discussed (4.5).

4.1 The effect of noise on quantitative MT

Most quantitative MT models require the collection of a series of MT-weighted images and the estimation of a number of parameters by non-linear fitting. It is generally assumed that a high SNR in the acquired data will improve the quality of calculated maps, but the sensitivity of MT parameters to background noise has never been investigated. Here, by using synthetic data and simulating the effects of different levels of noise on the fit, I explore how the uncertainty on the acquired data propagates to the estimated parameters, and I attempt to demonstrate that a good

SNR for the measured signal is essential in order to reliably estimate the parameters from a small number of data points, thus keeping the acquisition time to a minimum.

4.1.1 The Henkelman-Ramani model

All the work presented in this chapter is based on a modified version of the Henkelman model (Henkelman et al., 1993; see Chapter 3), proposed by Ramani et al. (Ramani et al., 2002).

In brief, the Henkelman model was modified by introducing f, the bound proton fraction, as:

$$f = \frac{M_0^B}{M_0^B + M_0^A}, \qquad [4.1]$$

where M_0^A and M_0^B are the fully relaxed values of magnetisation associated with the two pools (A=liquid, B=semisolid).

Using f, the MT-weighted signal intensity (Eq [3.27]) can be written as:

$$S = gM_0 \left(\frac{R_B\left[\frac{RM_0^A f}{R_A(1-f)}\right] + R_{RFB} + R_B + RM_0^A}{\left[\frac{RM_0^A f}{R_A(1-f)}\right](R_B + R_{RFB}) + \left(1 + \left[\frac{\omega_1}{2\pi\Delta f}\right]^2 \left[\frac{1}{R_A T_2^A}\right]\right)(R_{RFB} + R_B + RM_0^A)} \right), \qquad [4.2]$$

where g is a scanner dependent scaling factor, M_0 is the equilibrium magnetization, R is the MT rate between the two pools (assumed symmetrical in the two directions), R_A ($=1/T_{1A}$) and R_B are the longitudinal relaxation rates of the free and semi-solid pools respectively, and T_2^A and T_2^B are their transverse relaxation times. T_2^B does not appear explicitly in the model, but enters it via R_{RFB}, the rate of loss of longitudinal magnetization due to the irradiation of amplitude ω_1, expressed in rads^{-1}, and offset frequency Δf. For *in vivo* applications, ω_1 is estimated as the continuous wave power equivalent (ω_{CWPE}) and it is set to be the root mean square value of the saturating field (see Chapter 3). In brain tissue, R_{RFB} can be modelled assuming a super-Lorentzian lineshape (Li et al., 1997; see Chapter 3).

From the eight fundamental quantities present in the Eq. [4.2], only six independent parameters can be determined: RM_0^A, gM_0^A, R_B, $f/R_A(1\text{-}f)$, $1/R_A T_2^A$ and T_2^B. In order to extract the bound fraction, f, from the fitted $f/R_A(1\text{-}f)$, knowledge of

R_A is also required. This can be achieved by independently measuring the observed longitudinal relaxation rate of the sample, R_{Aobs} (=$1/T_{1obs}$) (Henkelman et al., 1993). R_A can then be estimated according to the following relationship (Ramani et al., 2002):

$$R_A = \frac{R_{Aobs}}{1 + \frac{\frac{RM_0{}^A f}{R_A(1-f)}(R_B - R_{Aobs})}{R_B - R_{Aobs} + RM_0{}^A}}, \qquad [4.3]$$

and used to calculate f from the estimated $f/R_A(1\text{-}f)$.

4.1.2 Simulations of the effect of noise

Monte Carlo simulations of the effect of noise were obtained on a Unix workstation (Sun Microsystems, Mountain View, CA, USA) by creating a synthetic data set using MT parameter values typically measured in white matter (Davies et al., 2004; Sled et al., 2004) as input into Eq [4.2]. By using two RF amplitudes (250 $rads^{-1}$ and 850 $rads^{-1}$, of the same order as those in many published protocols) and five offset frequencies (ranging from 0.4 to 20 kHz, homogeneously spaced on a logarithmic scale), a noise-free synthetic set of 10 MT-weighted signal intensities was generated according to Ramani's model. The values of the MT parameters used are reported in Table 4.1.

Table 4.1. Values of MT parameters used to create a synthetic dataset.

$RM_0{}^A$	$f/[R_A(1\text{-}f)]$	$T_2{}^B$	$1/(R_AT_2{}^A)$	gM_0 (arbitrary)	R_B (fixed)
25 s^{-1}	0.08 s^{-1}	10 μs	10	1.0	1.0 s^{-1}

These values were obtained based on the MT parameters published by Davies et al. (2004) and Sled et al. (2004).

Complex noise, with Gaussian real and imaginary parts, was added to the synthetic data, and noisy datasets were created by taking the magnitude of this complex number. The added noise had zero mean and standard deviation equal to S_0/Σ, where Σ was the desired SNR in the unweighted image, which varied over the interval [20, 300]. This range was chosen to bracket the SNR values typically seen

in SPGR scans from our systems (with acquisition parameters similar to those detailed in Chapter 3), which vary between 50 and 120 depending on the coil used, field strength, etc. This approach has previously been used to characterise the effect of noise on anisotropy indices estimated from diffusion-tensor-MRI (Pierpaoli and Basser, 1996). For each level of noise, 10000 independent samples were generated, and Eq [4.2] was fitted to every synthetic dataset, using the Levenberg-Marquardt method (Press et al., 1992). R_B was set arbitrarily to 1 s^{-1} and kept fixed during the fitting, as described by others (Henkelman et al., 1993; Ramani et al., 2002; Sled and Pike, 2001). Look-up-tables were used for the super-Lorentzian lineshape and its derivative, in order to increase the speed of the computation.

4.1.3 Results

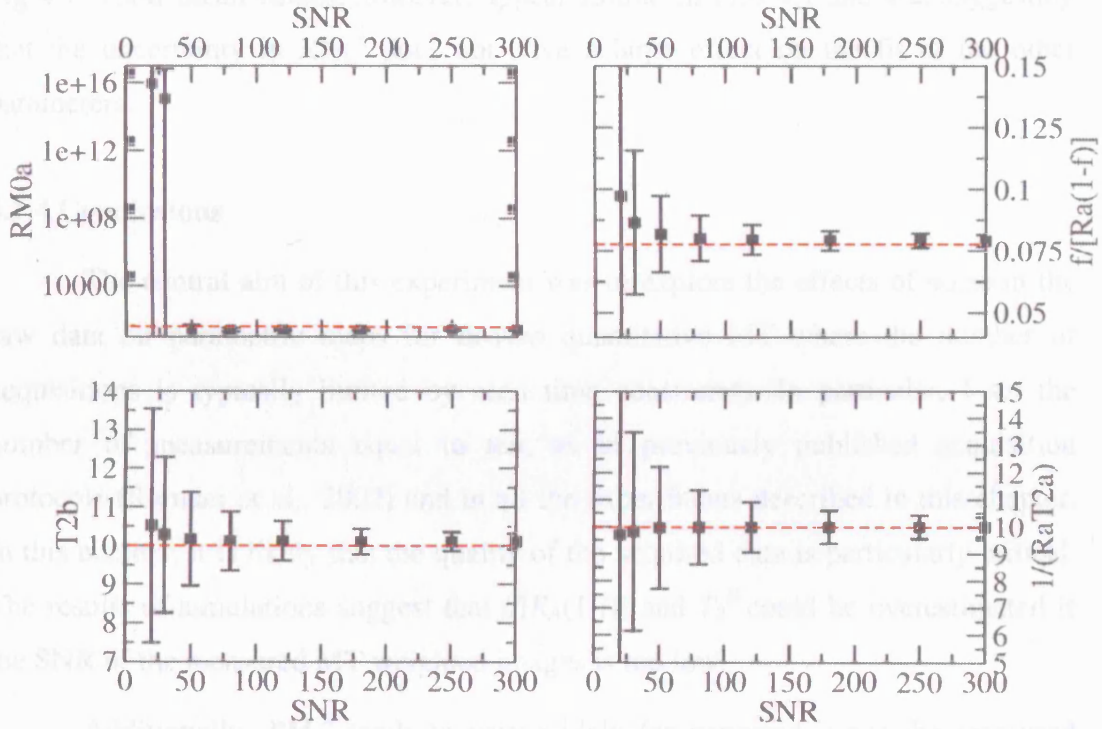

Fig 4.1. Results of simulations.

The squares represent the mean MT parameters estimated from 10000 noisy datasets at each different level of SNR. The bars represent the standard deviation of the estimated parameter across the 10000 randomisations. The red lines indicate the actual value used to produce the noise-free data. Top left: RM_0^A [s^{-1}]; top right: $f/R_A(1-f)$ [s^{-1}]; bottom left T_2^B [μsec]; bottom right: $1/R_A T_2^A$.

Fig 4.1 shows the results of simulations for RM_0^A, $f/R_A(1-f)$, T_2^B, and $1/R_AT_{2A}$. The most obvious effect is that RM_0^A tends to vary widely at low SNR, leading to physically meaningless results. Out of the 10000 randomisations for SNR=20, RM_0^A was larger than 500 s^{-1} (i.e. 20 times its true value) 702 times, at SNR=30, this happened 149 times, at SNR = 50, this happened once. (For SNR>50, however, the highest value seen was 77.9 s^{-1}).

In order to establish the degree of bias introduced into the estimation of other parameters by clearly meaningless values of RM_0^A, Fig 4.2 shows the mean (± standard deviation) MT parameters obtained when removing the results of randomizations for which RM_0^A was larger than 500 s^{-1} (i.e. 20 times its true value). At low SNR, the standard deviation of the other parameters is reduced compared to Fig 4.1. Their mean values, however, appear similar in Figs 4.1 and 4.2, suggesting that the uncertainty in RM_0^A does not have a large effect on the fit of the other parameters.

4.1.4 Conclusions

The central aim of this experiment was to explore the effects of noise in the raw data on parametric maps for *in-vivo* quantitative MT where the number of acquisitions is typically limited by scan time constraints. In particular, I set the number of measurements equal to ten, as in previously published acquisition protocols (Ramani et al., 2002) and in all the experiments described in this chapter. In this context, it is likely that the quality of the acquired data is particularly critical. The results of simulations suggest that $f/[R_A(1-f)]$ and T_2^B could be overestimated if the SNR of the measured MT weighted images is too low.

Additionally, RM_0^A tends to vary widely (as expected, since the measured signal is quite insensitive to variation in RM_0^A). Although the remaining parameters are relatively robust over the range of SNR typical of clinical MT-weighted scans, this analysis confirms that a good SNR (greater than 50) is essential in order to reliably estimate MT parameters from a small number of samples, prompting the use of an acquisition sequence with high SNR per unit time, such as a 3D spoiled gradient echo.

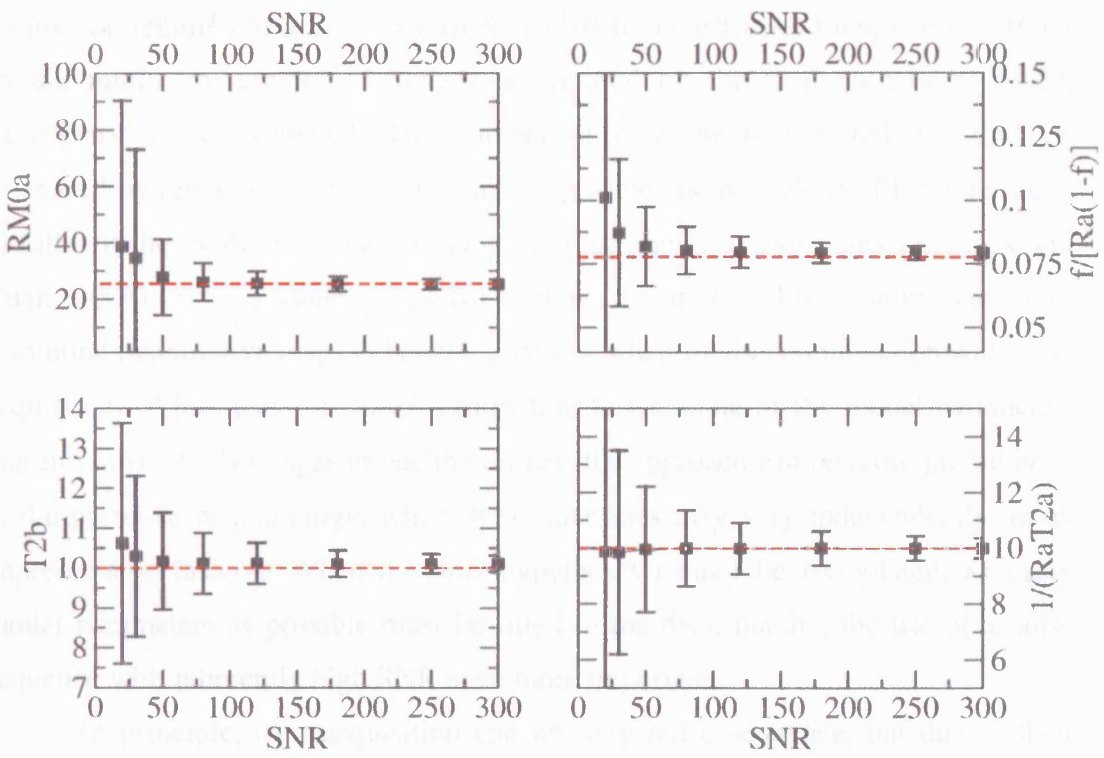

Fig 4.2. Results of simulations after removing outliers (cases when RM_0^A >500 s^{-1}).

Squares represent the mean value, bars represent the standard deviation.

A major limitation of this analysis is the fact that the precision and accuracy of the estimated parameters depend not only on the SNR of raw data, but also on the set of points sampled. The set of points used here was selected following Sled and Pike (2000), who explored different sampling schemes with 60 sample points and reported little benefits in using more than two values of ω_1 each with a range of Δf. This is, however, a heuristic result, and they did not perform a formal analysis. This subject will be further explored in section 4.4.

4.2 Implementation of a three-dimensional acquisition for quantitative MT imaging of the human brain

4.2.1 Background

Clinical applications of quantitative MT are limited due to the long acquisition times and the partial brain coverage achievable. The acquisition time is predominantly affected by the number of data points and/or SNR of the underlying

acquisition required to achieve a sufficient SNR in the calculated maps. A constraint on the minimum number of images is imposed by the total number of model parameters to be estimated. The number of data points required can thus be decreased by reducing the number of model parameters to a subset of those required to fully fit the model by imposing physically meaningful constraints (Yarnyck and Yuan, 2004). Such a strategy has been shown to produce high-quality and high-resolution quantitative maps in healthy controls, when used in combination with a 3D acquisition. While using *a priori* information to fix some of the model parameters presents several advantages in healthy tissues, the approach can be more problematic in the presence of pathology, when these quantities may vary independently, in an unpredictable fashion. When *a priori* hypotheses cannot be formulated, as many model parameters as possible must be fitted to the data, making the use of a pulse sequence with inherently high SNR even more important.

In principle, data acquisition can use any pulse sequence, but due to their short scan times and low T_1 and T_2 contrast on unsaturated images, interest has mainly focussed on gradient echo (GE) sequences. Both single slice (Sled et al., 2004) and multi-slice (Tozer et al., 2003; Davies et al., 2004) 2D sequences have been investigated. Three-dimensional acquisitions, on the other hand, have received less attention, but they overcome some of the limitations of multi-slice 2D GE acquisitions, such as the interference between adjacent slices (Kucharczyk et al., 1988) and the incidental MT effect from the slice selective pulses used (Dixon et al., 1990). These advantages, the ability to provide whole brain coverage, and better SNR for a given scan time (Edelstein et al., 1990), have already led to 3D imaging being applied to (non quantitative) MT imaging and MTR measurement (Dousset et al., 1992; Finelli et al., 1996, Tanabe et al., 1998). A 3D pulse sequence was also used by Yarnykh and Yuan for their reduced quantitative MT model (Yarnyck and Yuan, 2004), allowing high-resolution maps to be produced.

Here, I undertake a more complete investigation of 3D qMT imaging by implementing a time efficient 3D spoiled gradient recalled echo (SPGR) sequence, which provides whole brain coverage, and requires short acquisition time. By allowing the acquisition of more data for the MT model and by permitting a more robust and complete fitting procedure, this sequence is suitable for clinical applications. The sequence was used to collect data from a group of healthy

individuals, producing estimates of quantitative MT parameters in various brain locations.

4.2.2 Pulse sequence and fitting routine

The protocol was implemented on a 1.5 T clinical scanner (SIGNA Horizon Echospeed, General Electric, Milwaukee, WI, USA).

The pulse sequence consists of a MT-weighted 3D fast SPGR acquisition with a TR of 30.7 ms, and a TE of 5.3 ms. In order to minimise the degree of T_1-weighting, an excitation flip angle of 5° was used. MT saturation was achieved using Gaussian RF pulses (standard deviation=2.98 ms, duration=14.6 ms), applied once every TR, prior to RF excitation. The flip angle and offset frequency of the pulses were varied; ten MT points were collected in total, as described below, using only two MT pulse powers, described by their equivalent on-resonance flip angles, following the observations of Sled and Pike (2000). For each power, five different frequency offsets, ranging from 400 Hz to 20000 Hz were used. The frequencies were separated by a constant logarithmic step of about 0.4. For all the experiments reported in this chapter, a matrix of 256x96x32 over a FoV of 240x180x160 mm^3 was used, for a total scan time of approximately 15 minutes (unless otherwise specified). Data were reconstructed to an in-plane matrix of 256x256 over a 24x24 cm FoV, while the 32 through-plane phase encode steps were used to reconstruct twenty-eight 5 mm thick slices (with 4 slices, two at each end of the imaging volume, being discarded to minimise wrap around effects, thus effectively covering a FoV of 240x180x140 mm^3). The manufacturer's birdcage head coil was used for both signal transmission and reception. The specific absorption rate (SAR) was estimated during scan setup, using the manufacturer's standard calculation routines, assuming a 'worst case scenario' of MT pulses with the maximum flip angle for all measurements.

All image processing was performed on a Unix workstation (Sun Microsystems, Mountain View, CA, USA). The quantitative MT parameters were obtained as follows. Five of the six independent parameters of Eq. [4.2] (RM_0^A, gM_0^A, $f/R_A(1-f)$, $1/R_AT_2^A$ and T_2^B) were estimated by fitting Ramani's model to the data using the Levenberg-Marquardt method, as implemented in Numerical Recipes (Press et al., 1992). As any imperfection in the B_1 field results in a deviation of the

MT pulse flip angle and therefore of ω_{CWPE} from the nominal value, field inhomogeneities can introduce a spatially varying bias in the estimated parameters (Sled and Pike, 2000). In order to correct the nominal flip angle of the MT pulses, the B_1 field was estimated using a calibration oil-filled phantom (24 cm diameter, 40 cm length), according to the method of Barker et al. (Barker et al., 1998); the MT pulse nominal flip angle was then scaled on a voxel by voxel basis by a factor equal to $B_{1actual}/B_{1nominal}$, where $B_{1nominal}$ is the B_1 field in the centre of the phantom (thus assuming the B_1 field in the centre of the phantom is correct). ω_{CWPE} was then calculated as described by Ramani et al. (Ramani et al., 2002). Look-up-tables were used for the super-Lorentzian lineshape and its derivative, in order to speed up the computation. R_B was set arbitrarily to 1 s^{-1} and kept fixed during the fitting (as explained in 4.1.2), an approach adopted by other authors (Ramani et al., 2002; Sled and Pike, 2001; Tozer et al., 2003) because estimates of the other parameters are largely insensitive to the value of R_B, and R_B tends to vary widely during the fitting procedure, leading to physically meaningless estimates.

4.2.3 Methods

4.2.3.1 MRI acquisition

Six healthy subjects (F/M=2/4, mean age=38.5 years, SD=8.3 years) were scanned using the following protocol: A) the 3D-MTSPGR acquisition described above, collecting 10 MT points using 2 flip angles (212° and 843°), corresponding to ω_{CWPE} = 212 and 845 rad s^{-1}, with 1 NEX for each MT-weighted volume; and B) three 3D SPGR volumes (TR=13.1 ms, TE=4.2 ms) with three different excitation flip angles (α = 25°, 15°, 5°) in order to independently estimate the longitudinal relaxation rate of the system, R_{Aobs}. All images were collected in an axial orientation. The same acquisition matrix and FoV as the MT-SPGR were used for sequence B). The total imaging time was less than 20 minutes.

One subject (female, age 31 years) was scanned twice, the second time acquiring all the images in the coronal plane, with a protocol otherwise identical to the axial acquisition, to allow orientation and slice thickness dependant effects to be investigated.

The study was approved by the Joint Research Ethics Committee of The National Hospital for Neurology and the Institute of Neurology, UCL, and all subjects gave written informed consent before entering the study.

4.2.3.2 Image post-processing

The ten MT-weighted volumes obtained with sequence A) and the three volumes obtained with sequence B) were co-registered with the first MT-weighted volume using a modified (Symms et al., 2003) version of Automated Image Registration (AIR, available at http://air.bmap.ucla.edu:16080/AIR) (Woods et al., 1998). T_{1obs} was estimated on a pixel by pixel basis by fitting the theoretical SPGR signal equation as a function of the flip angle (Venkatesan et al., 1998) to the SPGR signal (sequence B). The nominal flip angle was corrected for B_1 inhomogeneities using the same method as for quantitative MT parameters (Barker et al., 1998). Quantitative MT parameters were then estimated on a pixel-by-pixel basis as described in section 4.2.2. Once the parameters had been estimated, R_A was computed using Eq [4.3], f was extracted from the estimate of $f/R_A(1-f)$, and T_2^A was derived from the estimate of $1/R_A T_2^A$. Values of RM_0^A, T_{1obs}, f, T_2^A, T_1^A and T_2^B were measured by placing regions of interest (ROIs) on the coregistered T_1-weighted (flip angle = 25°) scans obtained from sequence B) in different areas of white and grey matter (see Table 4.2). ROI outlines (see Fig 4.3 for an example) were then superimposed on the quantitative MT parametric maps and the mean values were computed.

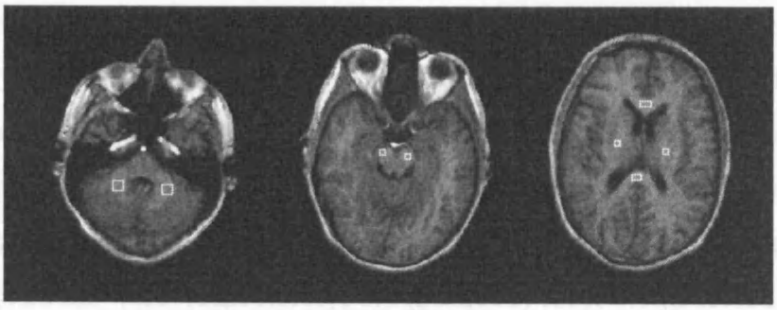

Fig 4.3. Examples of ROI placement in the cerebellum (left), in the cerebral peduncles (centre); in the corpus callosum and the internal capsule (right).

In order to investigate the effects of partial volume on the parameters measured *in vivo*, values obtained from the axial scan were compared pair-wise with those obtained from the coronal scan in several ROIs. Given the different orientation, the coronal and axial ROIs are expected to be only partially overlapping. Anatomical landmarks were used to ensure as close a match as possible.

Statistical correlations were assessed using the Spearman Correlation Coefficient in SPSS (SPSS Inc., Chicago, USA). All reported significances are two-tailed.

4.2.4 Results

All *in vivo* images obtained with the 3D-MTSPGR were of good quality. The average SNR (±standard deviation) on the least saturated image, measured using a ROI positioned in the periventricular white matter and estimating the noise according to Henkelman (1985), was 83±12. Typical parametric maps are shown in Fig. 4.4.

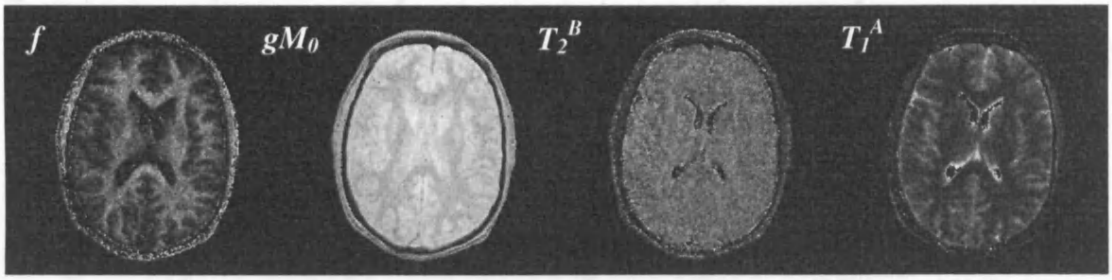

Fig 4.4. Typical quantitative MT parametric maps obtained from a healthy subject using the 3D-MTSPGR acquisition described in this chapter.

Bivariate correlations (Spearman Rank Correlation Coefficient) between parameters established strong inverse correlations between T_1^A and f (R=-0.9, p<0.001) and between T_2^A and f (R=-0.7, p<0.001). T_1^A and T_2^A were also correlated, more strongly in grey matter (R=0.7, p<0.001) than in white matter (R=0.4, p<0.001). Paired samples correlations between parameters measured on axial and coronal acquisitions were, respectively, 0.7 (p<0.001) for f, 0.7 (p<0.001) for T_1^A, 0.6 (p=0.003) for T_2^B, and 0.6 (p=0.003) for T_2^A.

In order to better visualise the shape of the MT spectrum, and the quality of the fit in the above maps, the same model was also fitted to the average signal intensity measured from the raw data for a number of ROIs. Such ROI based fits

benefit from increased SNR, and allow the variance of each raw data point to be visualised, albeit at the potential expense of partial volume effects. Typical examples of such fits are shown in Fig. 4.5 for two ROIs, each comprising 40 voxels. The variance of the fit (calculated as the sum of the squared difference between the data and the model, divided by the number of degrees of freedom) was 1.7 for the internal capsule (Fig 4.5A) and 2.6 for the thalamus (Fig 4.5B). The mean residual errors for these fits were 1.1% and 1.2%, respectively.

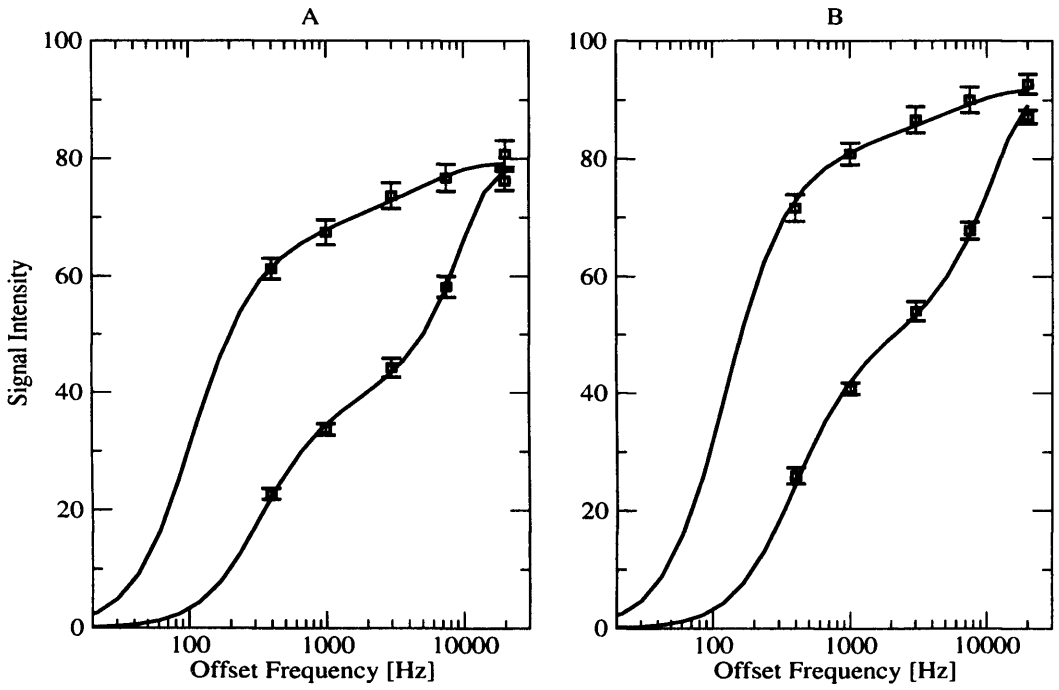

Fig 4.5. Typical curves obtained by fitting the 10 MT-weighted mean signal intensities (squares) measured in two ROIs.

The manually drawn regions were positioned in the posterior limb of the left internal capsule (A) and in the right thalamus (B). The error bars show the standard deviation of signal intensity (arbitrary units) within the region. The residual error was 1.1% for the internal capsule, and 1.2% for the thalamus.

Average values for the estimated RM_0^A, T_{1obs}, f, T_2^A, T_1^A and T_2^B in various brain regions are summarised in Table 4.2.

Table 4.2. Average qMT parameters measured in the brain at 1.5T.

Area			RM_0^A [s^{-1}]	f [%]	T_2^B [μs]	T_1^A [ms]	T_{1obs} [ms]	T_2^A [ms]
Corpus callosum	Genu	Mean	27.5	10.1	11.4	726	728	56.7
		SD	7.5	0.8	0.8	68	68	10.2
	Splenium	Mean	28.2	9.7	11.9	711	713	73.0
		SD	3.9	1.2	0.4	83	83	43.4
	Body	Mean	33.5	8.0	11.4	853	854	58.3
		SD	6.4	0.8	1.0	74	74	18.5
Internal capsule	Genu	Mean	27.1	9.0	12.7	749	751	54.8
		SD	5.8	1.2	1.2	67	67	12.7
	Posterior limb	Mean	26.2	9.3	13.8	734	736	56.7
		SD	4.4	1.1	0.9	47	47	4.9
Corona radiata		Mean	27.7	8.8	13.7	730	732	66.2
		SD	3.0	0.7	0.8	46	46	7.8
Optic radiation		Mean	33.2	9.4	12.3	661	663	61.1
		SD	6.9	0.9	0.8	44	44	7.7
Cerebral peduncles		Mean	28.0	9.2	13.4	745	747	72.5
		SD	5.8	1.3	0.9	61	60	29.9
Cerebellar WM		Mean	35.3	9.4	11.8	718	719	59.0
		SD	7.5	0.8	0.5	51	51	3.8
Pons		Mean	28.2	8.1	11.7	825	827	77.3
		SD	4.9	0.9	1.1	70	70	17.3
Frontal WM		Mean	45.8	9.1	13.4	719	720	53.5
		SD	19.1	0.6	0.8	41	40	5.0
Thalamus		Mean	29.2	6.6	11.8	975	976	69.8
		SD	3.9	0.7	0.8	61	61	8.5
Caudate		Mean	24.6	5.0	11.4	1164	1164	82.8
		SD	1.9	0.6	0.8	117	117	19.0
Putamen		Mean	32.8	5.2	10.9	1092	1092	78.6
		SD	7.5	0.7	0.6	85	85	9.9
Frontal GM		Mean	25.5	4.7	11.8	1279	1279	107.6
		SD	4.6	0.6	1.6	128	128	26.2

These values were obtained from six healthy volunteers. With the exception of the corpus callosum and the pons, the values were measured bilaterally.

RM_0^A = reverse MT exchange rate; f = bound proton fraction; A=free pool; B=restricted pool; SD=standard deviation, GM=grey matter, WM=white matter.

4.2.5 Discussion

A report describing regional variations of quantitative MT parameters within the brain of healthy subjects has recently been published, in which a single 7 mm thick slice was acquired (Sled et al., 2004). Here, the application of a 3D-MTSPGR sequence for quantitative MT acquisition allowed such investigations to be extended to a larger number of anatomical locations, collecting data from 6 healthy subjects and covering the whole brain with a 1×2×5 mm^3 resolution in less than 20 minutes.

Whole-brain coverage can also be achieved using a 2D multislice acquisition (Tozer et al., 2003; Davies et al., 2004). However, a 3D Fourier encoding provides considerable advantages over a 2D multislice method, including improved SNR for comparable resolution, and a reduction of partial volume effects and slice profile artefacts. Moreover, when using a 2D multislice acquisition, the incidental MT effect produced by subsequent slice excitation (Dixon et al., 1990) should be taken into account in modelling the signal intensity, particularly since this effect can vary with slice location.

In vivo, the quantitative MT parametric maps obtained using the 3D-MTSPGR sequence were of good quality; they appeared visually slightly noisier than those published by Sled and Pike (Sled and Pike, 2002), as would be expected given the smaller number of points (10 *vs* 60), and the higher resolution used for the present study. Quantitatively, all estimated parameters were within the range of expected values. The average T_2^B values showed very good agreement with previously published data (Sled et al., 2004; Davies et al., 2004). Interestingly, this parameter is characterised by a significant variability within white matter, which may result from different fibre geometries in different areas of the brain. The highest values were measured in the internal capsule, corona radiata, and cerebral peduncles, and the lowest in the corpus callosum and in the pons. The explanation for this finding is unclear. Since the resolution of the parametric maps was higher in-plane than in the slice-selective direction, the partial volume with either grey matter or CSF could affect T_2^B estimates in white matter fibres running within the axial plane, while preserving those running in the superior-inferior direction. However, the distribution of T_2^B estimated from the coronal dataset showed a similar trend to those obtained from an axial dataset, suggesting that the observed T_2^B variation did not originate solely from a partial volume artefact.

Yarnykh and Yuan (2004) imposed a fixed value to T_2^B, and therefore found no spatial variation of this parameter; however they did note a variation in f-maps with position (using an acquisition with thinner slices than those used in the current experiment). They explained this as resulting from the variable density of myelinated fibres in white matter tracts. The reason why differences in the underlying structure are reflected by two different parameters in the two different studies is unclear, but may be related to the use of different MT models in the two studies. In particular, since Yarnykh and Yuan fitted a reduced model (with fixed T_2^B) to their experimental data, it is conceivable that the variation in T_2^B observed here was reflected in a different parameter in their study. Despite these differences, this result confirms that quantitative MT is sensitive to white matter architecture.

Provided that differences in the model are taken into account, the f values in this study are consistent with those obtained in an earlier study (Sled et al., 2004). (Noting that because of differences in definition, the relation $f=F/(1+F)$, where $F = M_0^B/M_0^A$, must be used when comparing previously published values of the relative size of the restricted pool to f).

For the present proof of concept study, a simplistic approach for correcting the nominal flip angles of the MT pulses was used. Clearly, the use of calibration scans on a phantom to estimate the B_1 field is not ideal, since field homogeneity may vary due to loading or standing wave effects. Nevertheless, such effects are expected to be small at 1.5 T (Hoult, 2000), and there is evidence from the phantom measurements that the birdcage head coil used here gives very high homogeneity over its normal imaging volume. Ideally, a direct measure of B_1 uniformity in the head should be obtained at the acquisition time, particularly at higher field strength. The effects of B_1 inhomogeneities on MT parameters will be discussed in more detail in Chapter 5.

4.3 Implementation of quantitative MT imaging at 3.0 T and comparison with results at 1.5 T

4.3.1 Introduction

As discussed in 4.2.4, a technique like qMT imaging, limited by SNR, could greatly benefit from the improved SNR provided by increasing the static field

strength. However, moving to higher field strengths also involves increased power deposition into the sample, changes in the typical longitudinal and transverse relaxation rates of tissue and larger errors due to RF field inhomogeneity. Since MRI at 3.0 T is becoming more common, the feasibility of quantitative MT imaging at 3.0 T needs to be evaluated. A recent paper (Stanisz et al., 2005) provided an evaluation of MT parameters at 3.0 T in various *in vitro* tissues at body temperature. Comparison of these values with previous literature suggests that MT parameters are field independent, consistent with measurements in gels (Henkelman et al., 1993). To confirm these *in vitro* results, I obtained full brain quantitative MT measurements at 3.0 T from four healthy volunteers providing normative data for different areas of the brain.

I have already reported some preliminary results at 3.0 T in the previous chapter; in the current chapter, a qMT protocol similar to that developed at 1.5 T and discussed in 4.2.4 is described. Although the differences in SNR and in the mean age of the subjects taking part in the two studies prevent a direct statistical comparison, it is appropriate to qualitatively compare these values with those obtained at 1.5 T in the same anatomical areas (see Table 4.2).

4.3.2 Methods

4.3.2.1 In vivo B_1 mapping: Motivation and Implementation

Any deviation of the B_1 field from its nominal value introduces a bias into the flip angle of the RF pulses used during signal preparation. For conventional imaging, this results in spatially variable signal intensity. For quantitative imaging, it can result in substantial errors. In particular, for *in vivo* applications of Ramani's model, the value of ω_1 in Eq [4.2] is obtained by the continuous wave power equivalent approximation, i.e. it is directly proportional to MT pulse flip angle. It is therefore important to estimate the B_1 spatial distribution, and to account for it when attempting to measure the MT parameters. At 1.5 T I used a simplistic correction based on calibration scans obtained in a phantom. This approach was justified by the assumption that the *in vivo* field should deviate only slightly from that measured in oil. At 3.0 T, however, the wavelength of the RF field become comparable or even less than the dimensions of the sample (e.g. the head), and therefore the RF magnetic field inside the sample exhibits prominent wave behaviour. For this reason, additional effects related to tissue conductivity, dielectric resonance and standing

waves, which can be considered negligible at lower field strength should be taken into account.

For the following experiments, the B_1 field was estimated using the double angle method, or DAM (Stollberger and Wach, 1996), briefly summarized below. In a spin-echo pulse sequence, the measured signal intensity (*SI*) is proportional to the product of the sine of the excitation flip angle (α) and the squared sine of half of the refocusing flip angle (β), through a term A_{long} accounting for longitudinal relaxation. A_{long} depends on α, β, T_1, and *TR*, giving:

$$SI \propto A_{long}(\alpha(r),\beta(r),T_1(r),TR)\exp\left\{-\frac{TE}{T_2}\right\}\sin\alpha(r)\cdot\sin^2\frac{\beta(r)}{2}. \qquad [4.4]$$

If two images are acquired with identical *TE*, *TR* and refocusing pulse, but different values of α (α_1, α_2), the ratio of their signal intensity (SI_1/SI_2) is therefore:

$$\frac{SI_1}{SI_2}=\frac{\sin\alpha_1}{\sin\alpha_2}\frac{A_{long,1}(\alpha_1,\beta,T_1,TR)}{A_{long,2}(\alpha_2,\beta,T_1,TR)}. \qquad [4.5]$$

For a sufficiently long *TR*, A_{long} becomes equal to 1. If we set $\alpha_2=2\,\alpha_1$ in Eq [4.5] we obtain:

$$\frac{SI_1}{SI_2}\overset{(T1/TR)\to 0}{=}\frac{\sin\alpha_1}{\sin 2\alpha_1}=\frac{1}{2\cos\alpha_1}. \qquad [4.6]$$

The scaling factor (α_{corr}) to correct the nominal amplitude (α_{nom}) of all flip angles can then be estimated as

$$\alpha_{corr}=\frac{\alpha_{1,actual}}{\alpha_{1,nom}}=\frac{1}{\alpha_{1,nom}}\arccos\frac{SI_2}{2SI_1}. \qquad [4.7]$$

When applied *in vivo*, the main disadvantage of this method is the long scan time required, due to the need for long *TR*s for complete T_1 recovery of CSF. Although the theory was developed for conventional spin-echo acquisitions, other types of readout such as fast spin-echo have been used (Ropele et al., 2005), assuming that Eq [4.6] should hold, at least to a first approximation. Alternative faster readouts include multi-shot EPI and 3D fast recovery FSE (FR-FSE). In FR-FSE, the longitudinal magnetization is forced back into equilibrium by the use of a

pulse of opposite phase to the excitation pulse which follows the train of refocusing pulses.

4.3.2.2 MR image acquisition

Four subjects (1 female, mean age: 34.8 years, standard deviation: 2.9 years) took part in the study after giving written informed consent, and the study was approved by the relevant Research Ethics Committee. Every subject underwent the following protocol: a) MT-weighted fast SPGR pulse sequence (TE=3.2 ms; TR=28.7 ms; excitation flip angle=5°); b) three 3D SPGR volumes (TE=3.1 ms, TR=7.4 ms) with three different excitation flip angles (α=15°, 7°, 3°), in order to independently estimate T_{1obs}. The flip angles were optimized for the typical T_1 values of white matter and grey matter at 3.0 T (Clare and Jezzard, 2001); c) Two 3D FR-FSE pulse sequences (TE=19.5 ms, TR=300 ms, matrix=128x96x24, FoV=240x180x140 mm^3) with excitation flip angles 60° and 120°, respectively, to estimate the B_1 field. All images were acquired in the axial plane. For sequences a) and b) a matrix of 256x96x32 over a FoV of 240x180x160 mm^3 was used, but data were reconstructed to an in-plane matrix of 256x256 over a 24x24 cm^2 FoV, while 32 through-plane phase-encode steps were used to reconstruct only twenty-eight 5 mm thick slices (with 4 slices being discarded to minimise wrap around). MT saturation was achieved using Gaussian pulses (standard deviation=2.98 ms, duration=14.6 ms), applied once every TR, prior to RF excitation. Ten MT points were collected in total, using two MT pulse powers, with equivalent on-resonance flip angles equal to 600° and 200°, respectively. The highest power was determined empirically, by entering a range of possible values of MT flip angle into the manufacturer provided SAR calculation software and noting when SAR limits were approached. For each power, five different frequency offsets, ranging from 400 Hz to 20 kHz (identical to those at 1.5 T) were used. The manufacturer's body coil was used for transmission, and their 8-channel head coil for reception.

4.3.2.3 Image post-processing

All image processing was performed on a Unix workstation (Sun Microsystems, Mountain View, CA, USA). All images were coregistered to the first MT-weighted volume (Symms et al., 2003; Woods et al., 1998). B_1 field maps were obtained by

calculating α_{corr} on a pixel-by-pixel basis according to Eq [4.7]. The maps were then smoothed by fitting a third order polynomial to the resulting images. T_{1obs} maps were calculated as explained in 4.2.3.2, and quantitative MT parameters were estimated as described in 4.2.2. Rectangular ROIs were placed in the same anatomical regions as for the analysis of 1.5 T data (see 4.2.3) and the corresponding average RM_0^A, f, T_{1obs}, T_1^A, T_2^A, and T_2^B values were estimated.

4.3.4 Results

A typical example of *in vivo* B_1 map is shown Fig 4.7. Average values for the estimated RM_0^A, f, T_{1obs}, T_1^A, T_2^A, and T_2^B are reported in Table 4.3.

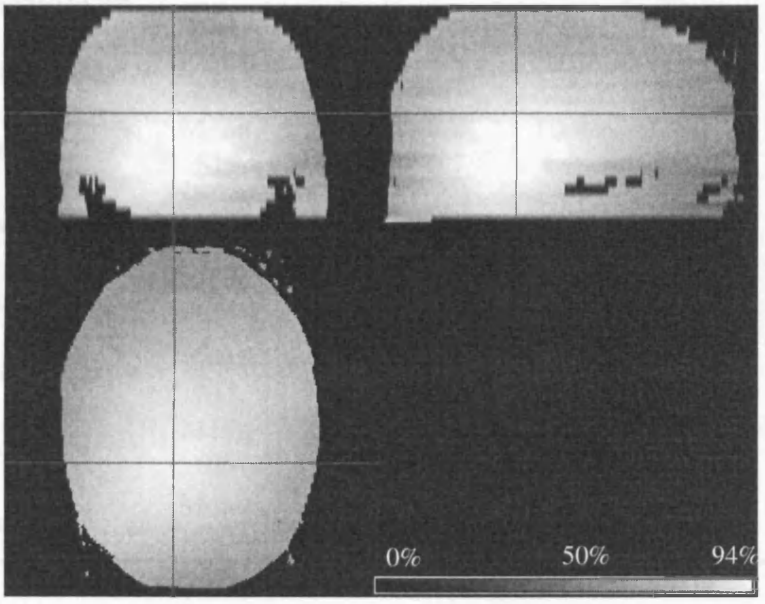

Fig 4.6 *Typical B_1 map at 3.0 T (using the manufacturer's body coil for transmission) obtained as described in section 4.3.2.1. The maximum deviation from the value in the centre of the head is approximately 35%.*

Table 4.3. Average qMT parameters measured in the brain at 3.0 T

Area			RM_0^A s^{-1}	f [%]	T_2^B [μs]	T_1^A [ms]	T_{1obs} [ms]	T_2^A [ms]
Corpus callosum	Genu	Mean	27.5	12.0	8.5	819	838	28.4
		SD	6.5	0.6	0.4	68	62	6.5
	Splenium	Mean	21.2	10.6	9.6	1140	1123	45.1
		SD	6.3	1.2	1.1	132	116	4.2
	Body	Mean	18.4	7.6	10.5	1202	1185	50.2
		SD	6.1	0.4	1.5	78	72	5.5
Internal capsule	Genu	Mean	19.8	9.9	11.4	995	996	38.9
		SD	2.8	0.5	0.8	74	67	3.6
	Posterior limb	Mean	19.3	10.5	11.8	1030	1027	50.7
		SD	4.3	0.3	0.7	98	88	5.7
Corona radiata		Mean	27.4	10.3	11.4	837	852	40.0
		SD	5.9	0.7	0.8	56	52	4.8
Optic radiation		Mean	22.2	10.7	11.2	973	975	43.8
		SD	4.2	0.6	0.9	137	123	2.8
Cerebral peduncles		Mean	17.3	8.4	12.4	1345	1308	60.7
		SD	1.5	0.6	1.3	91	80	4.7
Cerebellar WM		Mean	25.2	9.0	10.4	1235	1209	62.1
		SD	5.0	0.7	0.6	164	144	6.9
Pons		Mean	22.1	8.2	10.4	1395	1352	69.1
		SD	2.6	0.7	1.3	130	115	11.8
Frontal WM		Mean	47.0	10.1	10.1	767	786	31.5
		SD	19.1	0.7	1.0	63	59	42.8
Thalamus		Mean	20.3	6.3	10.3	1524	1477	52.5
		SD	3.6	0.4	0.9	110	98	4.3
Caudate		Mean	28.4	4.7	8.7	1416	1395	47.2
		SD	10.9	0.3	2.1	160	140	10.8
Putamen		Mean	25.4	5.4	8.8	1305	1284	45.9
		SD	5.5	0.1	0.7	100	92	4.2
Frontal GM		Mean	28.23	5.4	7.7	1245	1230	45.0
		SD	13.0	0.8	1.4	182	170	9.7

These values were obtained from four healthy volunteers. With the exception of the corpus callosum and the pons, the values were measured bilaterally.

RM_0^A = reverse MT exchange rate; f = bound proton fraction; A=free pool; B=restricted pool; SD=standard deviation, GM=grey matter, WM=white matter.

Typical parametric maps obtained at 3.0 T are reported in Fig 4.7. The SNR appears greatly increased compared to Fig 4.4. This is due to both the increased field

strength and the use of an 8-channel phased array coil, which provides almost twice the SNR of the birdcage quadrature head coil.

4.3.5 Discussion

To the best of my knowledge the work presented here is the first attempt to provide *in vivo* an estimate of MT parameters from a large number of brain areas at 3.0 T. Theoretical considerations and experiments in vitro suggest that MT parameters are field independent (Henkelman et al., 1993), while the RM_0^A values I obtained at 3.0 T appear consistently slightly lower than those measured at 1.5 T. One possible explanation is the large difference in SNR for the two data sets (due to both higher field strength and the use of multi-channel receiver coil for the 3.0T study). I have shown (section 4.1) that SNR can bias the measurement of this parameter, due to the low sensitivity of the measured signal to its variations. In particular, when using an MT model which does not take into account the timing of the pulse sequence elements, such as Ramani's model, it is difficult to estimate RM_0^A accurately. The sensitivity to noise of this parameter is also apparent from the map in Fig 4.7. An alternative explanation lies in the different type of coil used for signal transmission, and in the different type of correction for B_1 inhomogeneities in the two datasets. Deviations from the nominal B_1 field can affect different MT parameters by different amounts, as shown in more detail in Chapter 5. These data are insufficient to provide a final interpretation of this discrepancy, and further investigations are warranted. A formal comparison between data acquired at different field strength should be performed based on data from the same subjects, minimizing the potential confounding factors, such as the use of different transmit and receive coils, and different post-processing. The SNR difference could also be compensated for, by adding synthetic noise to the 3.0 T data.

The quality of the parametric maps appears greatly improved relative to those obtained previously at 1.5 T. In grey matter, and also in some areas of white matter, T_2^B values appear slightly decreased at 3.0 T. The values measured are consistent with measurements obtained *in vitro* at 3.0 T (Stanisz et al., 2005), and the decrease is likely to be a consequence of a more accurate assessment of this quantity at higher field strength, rather than a genuine difference. The values of T_2^B measured in white matter at 3.0 T confirm previous observations of significant variability, which might be related to white matter architecture.

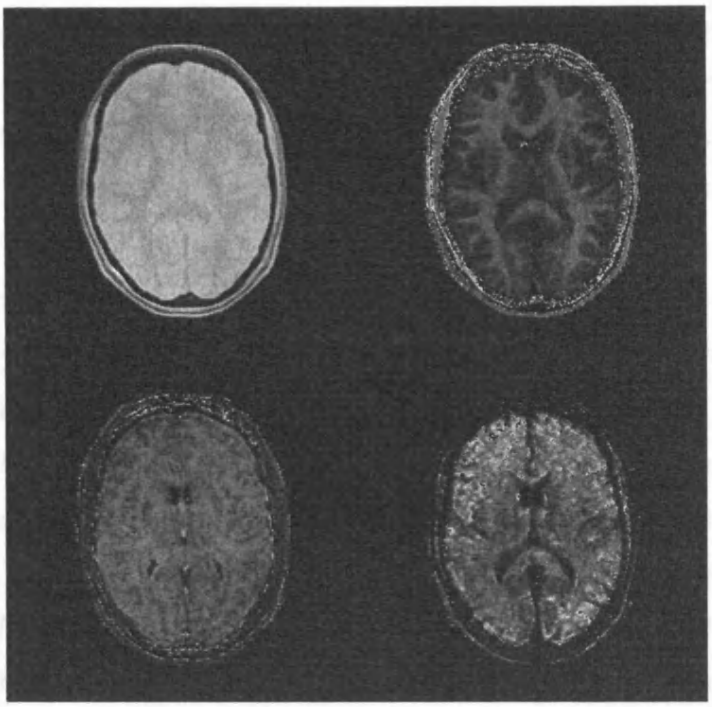

Fig 4.7. Magnetization Transfer parametric maps obtained at 3.0 T.
Proton density image (top left); bound proton fraction (f) map (top right); macromolecular pool T_2 map (bottom left); reverse exchange rate (RM_0^A) map (bottom right).

Anisotropy of T_2 relaxation is known to occur in some tissues (Henkelman et al., 1994), due to decoupling at the magic angle of the dipole-dipole interaction from the main magnetic field. This phenomenon has never been observed in white matter, and Henkelman et al. (1994) were unable to identify angular anisotropy in MT effects. Nevertheless, it is conceivable that some dependency of T_2^B on the orientation of a structure with respect to the direction of the B_0 field might exist, as the MT effect is mediated by dipolar coupling (Ceckler and Balaban, 1990). This sensitivity of quantitative MT parameters to fibre orientation has been suggested by others (Yarnykh and Yuan, 2004) and should be further investigated. One of the factors limiting information on this phenomenon is the use of 5-7 mm thick slices in most quantitative MT protocols, which results in large partial volume effects. The improved SNR at 3.0 T could therefore be exploited to reduce the slice thickness and to investigate the variability of T_2^B in smaller structures. As shown previously (Sled et al., 2004), f also appears to vary according to the white matter region where it is measured, an effect thought to be related to axonal density. Consistent with this

hypothesis, my results show that the highest values of f are in the genu of the corpus callosum, where fibres are thin and most densely packed (Aboitiz et al., 1992). Interestingly, the sharp white-to-grey matter contrast that characterises f maps is not observed on T_2^B maps. This finding is unexpected, as it would indicate that the mechanisms responsible of changes in relaxation time are unrelated to the relative density of macromolecular protons in a given tissue. An alternative explanation is that f is identifying only a portion of bound water species. Further investigations are needed to clarify this issue.

The MT parameters I obtained *in vivo* compare well with those measured *in vitro* at body temperature at 3.0 T (Stanisz et al., 2005). In that report (Stanisz et al., 2005), M_0^A is assumed to be equal to 1, and therefore the reported values of R correspond to RM_0^A in Table 4.3, while, M_0^B corresponds to $f/(1-f)$. The white matter sample used by Stanisz et al. was taken from the corpus callosum, and the corresponding MT parameters are in agreement with the values of RM_0^A, T_2^B, and f I measured in both the genu and the splenium of the corpus callosum. The value of R reported for grey matter by Stanisz et al. is larger than the average RM_0^A I measured in grey matter at 3.0 T, but it is also larger than the values reported by others at 1.5 T (Sled et al., 2004). The explanation for this is unclear; however, one possible reason is that the sample of grey matter used by Stanisz et al. was taken from the cortex, while I (and others) sampled subcortical grey matter regions, less likely to be contaminated by partial volume effects than those in the cortex. Different subcortical grey matter regions have different neuronal density. For example, neurons in the caudate and putamen are densely packed, while less so in the pallidum. The MT characteristics of different grey matter regions have not been studied as extensively as those of white matter and little is known about their variability. Even within the cortex, the number of neuronal layers varies greatly, depending on location and function. Given this structural diversity, it is conceivable that magnetization exchange occurs at variable rates in different grey matter regions.

One of the main disadvantages of moving to higher field strengths is the increase in the amount of radio-frequency energy patients are exposed to. This has safety implications that should not be overlooked. For this reason, the amplitude of the equivalent on-resonance maximum flip angle used for the measurement of MT parameters at 3.0 T had to be reduced compared to that at 1.5 T. The protocol was also modified by introducing the measurement of B_1 inhomogeneity *in vivo*, at the

acquisition time, as opposed to the use of calibration scans (Barker et al., 1998). The double angle method is relatively easy to implement, and due to the use of a FR-FSE pulse sequence, an efficient 3D acquisition scheme was set up for these experiments, giving a B_1 map scan time of approximately 2 minutes.

4.4 Optimisation of qMT acquisition schemes

4.4.1 Introduction

For all quantitative techniques based on model fitting, the precision and accuracy of the parameter estimates depend on the choice of the sampling points; in MT, these are the settings of ω_1 and Δf in the MT-weighted images. In most published MT protocols, the set of sampling points has been selected empirically. Sled and Pike (2000, 2001), while not performing a formal analysis, explored different sampling schemes with 60 sample points. They reported little benefits in using more than two values of ω_1 each with a range of Δf. The choice of points is particularly critical for *in-vivo* imaging where time limits the number of images we can acquire. In this chapter, I explore the use of optimal configurations of sample points for *in-vivo* quantitative MT, where the number of acquisitions is typically limited by time constraints.

The issue of optimising sampling strategies are similar for all quantitative MRI and other model fitting techniques. Several approaches are possible. For simple models, where the parameter of interest can be expressed directly as a function of measurements with known variance, error propagation provides an estimate of the parameter variance which can be optimised with respect to the sample points. For example, error propagation provides optimal b-values in a basic *apparent diffusion coefficient* measurement (Xing et al., 1997). Numerical simulations also provide insight into the dependence of parameter estimates on sample points and can help find optimal configurations (see Alexander and Barker, 2005 as an example). For more complex models, such as quantitative MT models, the theory of Cramer-Rao lower bounds (CRLB) provides a useful analogue to error propagation. The CRLB (Kay, 1993) sets a lower bound on the variance of any unbiased estimate. In other words, the variance of any parameter estimate obtained by fitting a model to noisy measurements cannot be lower than the CRLB. Good sampling configurations

can be found by minimizing the CRLB (instead of the parameter variance) with respect to the sample points. In quantitative MRI, this method has been used to optimize sampling configurations for measuring T_2 relaxation time (Jones et al., 1997), diffusion coefficients (Brihuega-Moreno et al., 2003), and for the decomposition of water and fat signals in Dixon imaging (Pineda et al., 2005). Samson et al. (2005) reported a preliminary use of the CRLB to optimize MT acquisition. They optimized the sampling for measuring a single parameter of the MT model and showed, using numerical simulations, that an optimised scheme with six-points estimates the macromolecular proton fraction as precisely as the ten-point scheme used by Ramani et al. (2002). However, their method sets all the other parameters to fixed values, which is unrealistic for heterogeneous samples, such as the human brain.

All the applications of the CRLB above optimise the sampling configuration for estimating a single parameter. However, in quantitative MT, several fitted parameters are of interest. The aim of the work here reported is the optimisation of sampling strategies for multiple parameters simultaneously. I used this approach to obtain optimal acquisition schemes for *in-vivo* quantitative MT imaging, although the method can be applied to any multi-parametric MRI technique. Experiments compare optimal schemes derived for quantitative MT in human white matter at 1.5 T to previous ones (see section 4.2.4), using both synthetic and human-brain data. All the simulations and optimisation routines described in this section were run on computers at the Department of Computer Science, UCL, London.

4.4.2 The Cramer-Rao lower bound and application to MT

The theory behind the CRLB has been detailed elsewhere, (see Kay, 1993), and only the concepts required for the present application will be reviewed here. If one considers a model S with Q unknown parameters p_1, ..., p_Q fitted to $N \geq Q$ measurements $A(\mathbf{x}_1)$, ..., $A(\mathbf{x}_N)$ acquired with different known settings $\mathbf{x}_1$, ..., $\mathbf{x}_N$, the Cramer-Rao inequality states that $\boldsymbol{\Xi} \geq \mathbf{J}^{-1}$, i.e. that the difference $\boldsymbol{\Xi}$-$\mathbf{J}^{-1}$ is a positive semi-definite matrix, where $\boldsymbol{\Xi}$ is the covariance matrix of an unbiased estimate of p_1, ..., p_Q, $\mathbf{J}$ is the Fisher information matrix, which has ij^{th} element

$$J_{ij} = \frac{1}{\sigma^2} \sum_{n=1}^{N} \frac{\partial S(p_1,\ldots,p_Q;\mathbf{x}_n)}{\partial p_i} \frac{\partial S(p_1,\ldots,p_Q;\mathbf{x}_n)}{\partial p_j}, \qquad [4.8]$$

and σ is the standard deviation of the noise, which I assume is independent of $\mathbf{x}$. Specifically, the variance of any unbiased estimator of p_i cannot be smaller than the i^{th} diagonal element $[\mathbf{J}^{-1}]_{ii}$ of $\mathbf{J}^{-1}$.

To find a set of sample points $\mathbf{x}_1, \ldots, \mathbf{x}_N$ that minimise the variance σ_i^2 of a particular p_i, the standard approach in the absence of a direct estimate of σ_i^2 is to instead minimise the lower bound $[\mathbf{J}^{-1}]_{ii}$ with respect to $\mathbf{x}_1, \ldots, \mathbf{x}_N$. To maximise the precision of multiple parameter estimates, the sample points that minimise several diagonal elements of $\mathbf{J}^{-1}$ simultaneously must be found. To ensure that the relative precision of each parameter is similar, the variance of each parameter can be weighted by the inverse square of the parameter's value and the value of $\sum_{i=1}^{Q} p_i^{-2}\sigma_i^2$ minimised. However, since the variances are unknown, in the work described below, the CRLB is used instead for each parameter to obtain the objective function

$$V = \sum_{i=1}^{Q} p_i^{-2}\left[\mathbf{J}^{-1}\right]_{ii} \qquad [4.9]$$

for any particular set of p_i.

It should be emphasized here that Eq. [4.9] requires the choice of a particular set of values for $p_1, \ldots, p_Q$. In a heterogeneous sample, such as the human brain, the p_i can assume a range of values. Here, therefore, an alternative to V that considers a range of settings of the p_i is considered:

$$V_{\max} = \max_k \left\{ \sum_{i=1}^{Q} p_{ik}^{-2}\left[\mathbf{J}_k^{-1}\right]_{ii} \right\}, \qquad [4.10]$$

where k ranges over K combinations of p_i, p_{ik} is the value of p_i in combination k and $\mathbf{J}_k$ is the Fisher information matrix for combination k. Minimizing $V_{\max}$ maximises the precision of the parameters for the worst case in the K combinations of settings. Examples of suitable combinations of settings are provided below.

In quantitative MT, the acquisition variables that define the sampling points are ω_1 and Δf, so $\mathbf{x}_n=(\omega_{1n}, \Delta f_n)$. keeping in mind the time limitations of clinical MT imaging, I set N=10, as in previously published acquisition protocols (Ramani et al., 2002) and in all the experiments described in this chapter. In each voxel, I fixed R_B at $1s^{-1}$ and estimated the remaining parameters by fitting the model in Eq. [4.2] to the measurements using a Levenberg-Marquardt algorithm, as described in section 4.2.

Four terms (Q=4) are included in the sum in Eqs [4.9] and [4.10] (corresponding to the parameters RM_0^A, $f/[(1-f)R_A]$, T_2^B, and $1/R_AT_2^A$) while terms for R_B (which is fixed), and gM_0 (which is of little interest) are excluded.

4.4.3 Optimisation

To optimize the sampling points for quantitative MT, I considered the minimization of both V and V_{max} from Eqs [4.9] and [4.10]. This was done in order to establish whether a substantial advantage is provided by the more time consuming optimization of V_{max}. The global minima of these cost functions are hard to find because of local minima. Thus, I used a minimization technique which combines simulated annealing with the downhill simplex method (Press et al., 1992). The routine makes 100 evaluations of the cost function at each temperature T, using expansions, contractions and reflections of the simplex to reach a local minimum. The cost-function value is randomly perturbed by a quantity proportional to $\log(T)$ to allow occasional uphill transitions, which increase the probability of finding a global minimum. The temperature T decreases according to the annealing schedule

$$T(n+1) = (1-\varepsilon)T(n), \qquad [4.11]$$

where $1 >> \varepsilon > 0$, until it reaches a pre-specified final temperature. The initial temperature was 100, above which perturbations were empirically found to be too large to be useful, and the final temperature was 0.001, below which perturbations to the results were smaller than the accuracy with which the scanner allows setting of ω_1 and Δf.

To further reduce the effects of local minima in the objective function, the optimization was repeated from a number of different starting points. In each optimization, six unique starting points were used and the final configuration with minimum value of the cost function was selected. This procedure does not guarantee finding the global-minimum configuration, but in practice gives good results which are not expect to improve on dramatically with more starting points or a slower annealing schedule. From Eq. [4.2], it can be seen that $S(\omega_1, \Delta f) = S(\pm\omega_1, \pm\Delta f)$ so two final configurations were considered identical if their points differ only in sign. It should be noted that the MT effect has been observed to be slightly asymmetric about the Larmor frequency (Pekar et al., 1996), and that such asymmetry could be

caused by a chemical shift centre mismatch between bulk water and macromolecules. This effect, however, is not accounted for in Eq [4.2].

Off-resonance irradiation inevitably produces some direct saturation of the liquid pool (see Chapter 3), which rapidly increases as the offset frequency of MT pulse is reduced and eventually suppresses any MR signal when Δf becomes small compared to the MT pulse bandwidth. Values of Δf close to zero thus result in dramatic signal loss, particularly in the presence of static field inhomogeneities, where the actual offset frequency can deviate slightly from its nominal value and vary across the sample. Moreover, safety issues associated with the deposition of radio-frequency energy into the patient, measured by the specific absorption rate (SAR), impose some restrictions on the maximum value of ω_1. Due to these practical limitations on the combinations of ω_1 and Δf, I applied constraints of $\omega_1<950$ rad s^{-1} and $|\Delta f|>0.15$ kHz. The value of 0.15 kHz was determined empirically by selecting the minimum offset frequency that does not result in macroscopic areas of signal loss in the image at the median value of ω_1 ($\omega_1\approx450$ rad s^{-1}); the most appropriate choice may vary depending on the MT pulse bandwidth and on the static field strength.

I computed and tested optimal parameters for three different situations, and compared them to the standard configuration used at 1.5 T, which I labelled scheme 1. Scheme 2 minimises V for a set of typical MT parameters measured in white matter at 1.5 T; specifically I set $RM_0^A=25$ s^{-1}, $f/[R_A(1-f)]$ $=0.08$ s^{-1}, $T_2^B=10$ μs, $1/R_AT_2^A=10$, $R_B=1$ s^{-1}, and $gM_0=1000$ (arbitrary), which are typical measured values from previous experiments at 1.5 T. Schemes 3 and 4 minimise V_{max} for different combinations of settings. For scheme 3, I used the values measured in the $K=15$ regions of interest from table 4.2. For scheme 4, I defined a range of values typical for the human brain at 1.5 T, and take the $K = 33$ combinations from the centre and the 32 vertices of the "hypercube" (i.e. the five-dimensional geometrical shape obtained by including a range of realistic values on each axes of the space defined by the five parameters of the MT model) spanning all the ranges. I estimated the ranges from previous measurements; specifically $RM_0^A\in[25, 35]$ s^{-1}, $f/[R_A(1-f)]$ $/R_A\in[0.05, 0.1]$ s^{-1}, $T_2^B\in[7, 15]$ μs, $1/R_AT_2^A\in[10, 20]$, and $gM_0\in[700, 1300]$, $R_B=1$ s^{-1}. In the minimization of V I set $\varepsilon = 0.0001$, but for V_{max} ε was increased to 0.001, since computation of the cost function is more expensive.

4.4.4 Experiments and Results

Two main hypotheses are tested. The first is that little improvement comes from optimizing V_{max} for many combinations of parameter settings over the simpler optimization of V for a single well chosen set. The second is that all the optimal point sets produce more precise maps of the MT parameters than the standard acquisition scheme used for previous measurements.

4.4.4.1 Optimal configurations

Table 4.4. Standard and optimised MT acquisition schemes.

1) Standard (see ref 18)		**2) Optimised for a single set**		**3) Optimised for 15 ROIs**		**4) Optimised for the hypercube**	
$V = 7.0$		$V = 2.2$		$V = 2.3$		$V = 3.1$	
$V_{max}^{hypercube} = 48.1$		$V_{max}^{hypercube} = 11.8$		$V_{max}^{hypercube} = 12.3$		$V_{max}^{hypercube} = 11.3$	
$V_{max}^{15\ ROIs} = 12.4$		$V_{max}^{15\ ROIs} = 3.5$		$V_{max}^{15\ ROIs} = 3.5$		$V_{max}^{15\ ROIs} = 4.9$	
$\omega[rads^{-1}]$	$\Delta f[kHz]$	$\omega[rads^{-1}]$	$\Delta f[kHz]$	$\omega[rads^{-1}]$	$\Delta f[kHz]$	$\omega[rads^{-1}]$	$\Delta f[kHz]$
222	**0.4**	**37**	**42**	**12**	**14.84**	**217**	**0.15**
222	**1**	**128**	**100**	**255**	**0.15**	**310**	**0.26**
222	**3**	**265**	**0.15**	**365**	**100**	**400**	**1.13**
222	**7.5**	**397**	**1.38**	**398**	**1.28**	**444**	**1.74**
222	**20**	**405**	**1.48**	**465**	**2.05**	**495**	**2.34**
885	**0.4**	**405**	**1.48**	**483**	**2.36**	**522**	**82.26**
885	**1**	**950**	**0.97**	**950**	**0.88**	**950**	**1.28**
885	**3**	**950**	**0.98**	**950**	**1.02**	**950**	**1.30**
885	**7.5**	**950**	**0.98**	**950**	**1.04**	**950**	**13.62**
885	**20**	**950**	**11.6**	**950**	**11.15**	**950**	**56.79**

Table 4.4 compares the three optimised sampling schemes with the standard ten-point scheme used for the experiments in section 4.2. The table shows the values of V and V_{max} for every scheme in order to provide a theoretical comparison of their performances. The minimum V_{max} was 11.3 for the hypercube (scheme 4) and 3.5 for the regions of interest (scheme 3). When using the optimal sampling scheme returned for a single setting (scheme 2), V_{max} was 11.8 for the hypercube and 3.5 for the regions of interest, supporting the first hypothesis that the optimal sampling is fairly insensitive to the exact p_i used in the optimization. With the standard scheme (scheme 1), V_{max} was 48.1 for the hypercube and 12.4 for the regions of interest, which suggests large improvements in precision with the optimal configuration compared to standard one. Table 4.4 shows similar reductions for V when comparing scheme 1 (V = 7.0) with scheme 2 (V = 2.2), scheme 3 (V = 2.3) and scheme 4 (V = 3.1).

4.4.4.2 Simulations

I used Monte Carlo simulations at various noise levels to measure the error in the parameters from the different acquisition schemes. First, four noise-free synthetic sets of ten MT-weighted signal intensities (one for each scheme) were generated by substituting the MT parameters used for the optimisation of V into Eq [4.2], and complex noise is added as described in 4.1. For each level of noise, 10000 independent samples were generated and Eq [4.2] was fitted to every synthetic dataset.

For all four parameters (RM_0^A, F/R_A, T_2^B, and $1/R_AT_2^A$), the estimates obtained using schemes 2-4 were more precise than those obtained with scheme 1, with standard deviations smaller by a factor of at least 1.5. Accuracy was also increased, particularly at low SNR (≤50). Schemes 2 and 3 produce similar performance, while scheme 4 produces slightly larger standard deviations for the estimates of T_2^B and $1/R_AT_2^A$.

Figure 4.8 compares the estimates of the MT parameters from schemes 1 and 2 and confirms an improvement in both precision and accuracy for all four parameters at all SNR levels when using the optimized scheme. For clarity, the

results for schemes 3 and 4 are omitted from Figure 4.8, since they are almost indistinguishable from the scheme 2 results.

To confirm the near equivalence in performance of the three optimized schemes, I repeated the simulation experiments using the worst-case combinations of parameters from both the hypercube and 15-region sets of combinations. The set of MT parameter values giving the worst V among the 15 regions of interest was $\{RM_0^A=33.2s^{-1}$; $F/R_A=0.07s$; $T_2^B=12.3\mu s$; $1/R_AT_2^A=11.4$ and $gM_0=804\}$. Using these values for the simulations, scheme 2 and 3 performed similarly in terms of precision, with slightly lower variance from scheme 3 at very low SNR (≤50) for T_2^B. The estimates obtained using scheme 4 were more precise than those obtained using scheme 1, but less precise than those obtained using scheme 2 and 3.

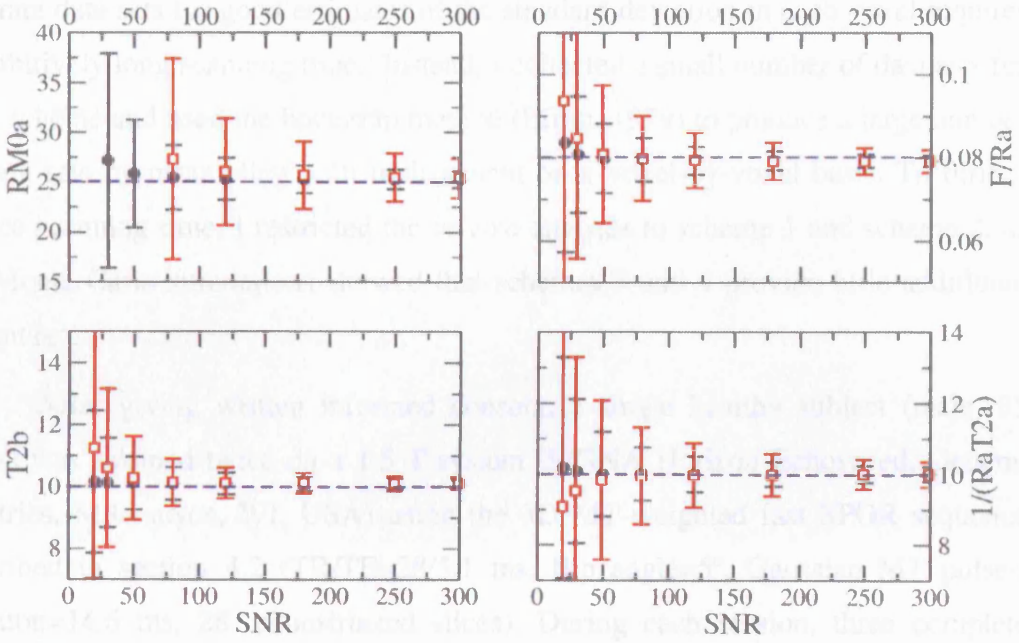

Fig 4.8. Plot of mean MT parameters from 10000 Monte Carlo simulations against SNR in the unweighted image.

The figure shows the mean values for the standard scheme 1 (red) and optimised (black) scheme 2. The error bars show the standard deviation. The dashed blue line shows the value of parameter used to create the simulation. No symbols are present for RM_0^A from scheme 1 at SNR≤50 as the mean value was too large to be displayed at the chosen y-axis scale.

The set of MT parameter values giving the worst V among the 33 vertices-and-centre of the hypercube was $\{RM_0^A=35.0s^{-1}$; $F/R_A=0.05s$; $T_2^B=7.0\mu s$; $1/R_AT_2^A=20.0$ and $gM_0=700\}$. Schemes 2 and 3 perform similarly, with slightly larger variances than scheme 4 for all four parameter estimates. The standard deviation of RM_0^A estimated using scheme 1 is larger than using any other scheme at all SNR levels, while all four schemes behave similarly for estimates of $f/[(1-f)R_A]$, T_2^B, and $1/R_AT_2^A$ at SNR>120.

4.4.4.3 MRI acquisition and analysis

In vivo data were collected to assess the precision of MT parametric maps in order to confirm the conclusions from the simulation experiments. To this aim, an estimation of the standard deviation of each MT parameter in several regions of interest from different acquisition schemes was required. To acquire enough separate data sets for good estimates of the standard deviation in each voxel requires prohibitively long scanning time. Instead, I collected a small number of data sets for each scheme and used the bootstrap method (Efron, 1979) to produce a large number of data sets by resampling with replacement on a voxel-by-voxel basis. To further reduce scanning time, I restricted the *in-vivo* analysis to scheme 1 and scheme 2, as the Monte Carlo simulations showed that schemes 3 and 4 provide little additional advantage.

After giving written informed consent, a single healthy subject (male, 35 years) was scanned twice on a 1.5 T system (SIGNA Horizon Echospeed, General Electrics, Milwaukee, WI, USA) using the 3D MT-weighted fast SPGR sequence described in section 4.2 (TR/TE=28/5.1 ms, flip angle=5°, Gaussian MT pulses, duration=14.6 ms, 28 reconstructed slices). During each session, three complete datasets were obtained using either scheme 1 or 2 in Table 4.4. In addition to the MT data, two four-shot spin-echo echo planar imaging sequences (EPI) (TR/TE=15000/13.6 ms, flip angles=60° and 120°, matrix 64x64) were collected for B_1 mapping. The total scan time for each session was just under an hour. The body coil was used for signal transmission and the eight-channel head coil was used for reception. After image co-registration (Symms et al., 2003), B_1 maps were obtained from the multi-shot EPI data using the double angle method (Stollberger et al., 1996) and smoothed using a third-order polynomial fitting.

In order to compare *in vivo* results with numerical simulations, I measured the SNR of the MT-SPGR data in white matter. SNR is hard to measure precisely because it is not uniform in images obtained with multi-channel coils. However, a good local estimate (SNR_{ROI}) can be obtained using two images I_1 and I_2 with the same weighting, as described by Firbank et al. (1999):

$$SNR_{ROI} = \sqrt{2}\frac{mean_{ROI}\left(\frac{I_1(r)+I_2(r)}{2}\right)}{std_{ROI}(I_1(r)-I_2(r))} \qquad [4.12]$$

where r is the spatial coordinate, $mean_{ROI}$ and std_{ROI} are the average and the standard deviation, respectively, calculated across a region of interest placed on the image obtained by performing the operations in parentheses on a voxel-by-voxel basis.

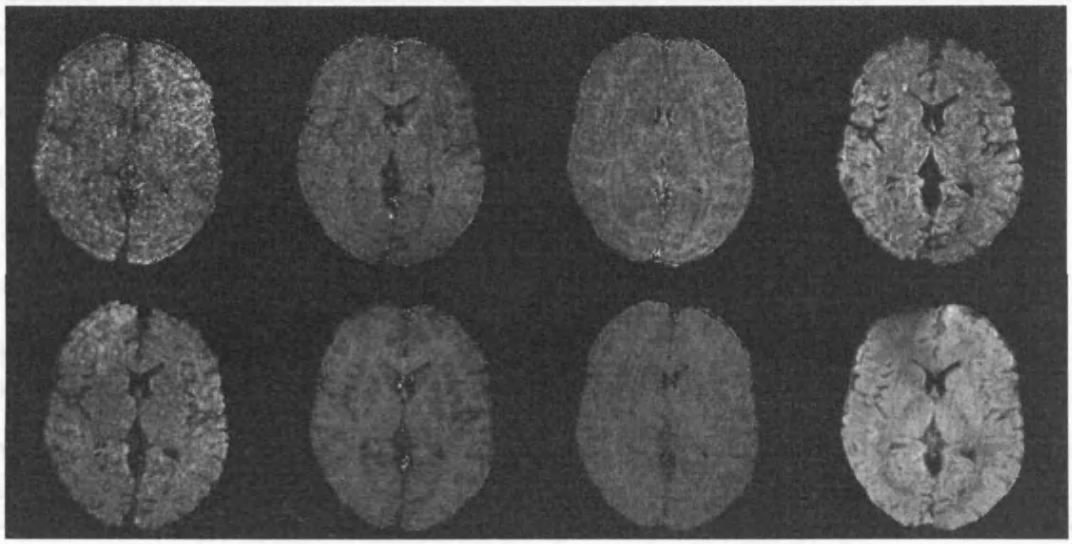

Fig 4.9. MT parametric maps obtained with the standard (top) and the optimized (bottom) sampling schemes.

From left to right: RM_0^A, $f/[(1-f)R_A]$, T_2^B, $1/R_AT_2^A$. Spatial homogeneity and white-to-grey matter contrast appear increased in all maps, but particularly in the RM_0^A map.

Using this method, I estimated the following values of SNR in four white matter regions on the least saturated image. SNR values were: 86 in the anterior periventricular white matter, 123 in the posterior periventricular white matter, 112 in the corona radiata, and 64 in the frontal white matter. The MT model in Eq [4.2] was

fitted as previously described (section 4.2.2) to the first repeat from each acquisition scheme to obtain an initial qualitative comparison of the two schemes. During the fitting, B_1 maps were used to correct for any deviation from the nominal values of ω_1. Figure 4.9 shows the MT parametric maps from the first repeat from each scheme. Maps from the optimized scheme show clear improvements in spatial homogeneity and grey-to-white-matter contrast.

Table 4.5. Mean parameter COV [p.u.] across 1000 bootstrapped samples for schemes 1 (standard) and 2 (optimised).

	RM_0^A		$f/[R_A(1-f)]$		T_2^B		$1/(R_AT_2^A)$	
SCHEME	1	2	1	2	1	2	1	2
putamen	**31**	**11**	**16**	**6**	**18**	**5**	**15**	**3**
thalamus	**23**	**8**	**10**	**4**	**10**	**2**	**10**	**3**
Corpus callosum	**28**	**11**	**12**	**5**	**8**	**4**	**10**	**4**
Anterior periv. WM	**27**	**13**	**12**	**7**	**10**	**4**	**11**	**4**
Posterior periv. WM	**21**	**9**	**10**	**5**	**9**	**3**	**10**	**5**

For bilateral structures, the value is the average of left and right.

Next, with the three repeats, 1000 MT raw data sets for each scheme were generated by bootstrapping. The model was fitted to each of the 1000 bootstrapped samples, providing 1000 estimates of RM_0^A, $f/[R_A(1-f)]$, T_2^B, $1/R_AT_2^A$, and gM_0. Table 4.5 compares the coefficient of variance (COV) of the MT parameters (defined as standard deviation divided by mean (expressed in percentage units) across the 1000 bootstrapped samples). Results were averaged over 2 grey matter regions (putamen and thalamus) and 3 white matter regions (genu of corpus callosum, anterior periventricular and posterior periventricular), with regions of interest outlined by

hand on the least saturated image of each set. The COV for optimized scheme 2 is consistently less than half that for the standard scheme (1) and is improved by a factor of up to 5 in some regions. This shows dramatic improvements in parameter estimation and confirms the observations from Fig. 4.9.

4.4.5 Discussion

I have presented a method based on the theory of CRLB for optimizing the sample positions for any multi-parametric quantitative MRI technique. I used this method to optimize an *in-vivo* quantitative magnetization transfer acquisition, which collects a series of MT weighted images and estimates a number of parameters by fitting a non-linear model to the measurements. I have shown at the beginning of this chapter that the uncertainty associated with the estimate of RM_0^A is particularly large (Graham and Henkelman, 1997), with some studies based on Ramani's model having failed to estimate this parameter entirely (Davies et al., 2004). Monte-Carlo simulations and *in-vivo* results showed that selecting appropriate sampling schemes greatly enhances both precision and accuracy of MT parametric maps. In particular, the optimized acquisitions reduced the error in parameter estimates by factors around 2 or 3 and allowed RM_0^A to be estimated with similar accuracy and precision to the other parameters. Simulations also showed that, even at low SNR, the optimal scheme provides more consistent estimates, thus confirming the validity of CRLB theory for this type of application.

The sampling-scheme optimisation requires prior knowledge of the values of the MT parameters in the sample. To allow for this, two types of objective function can be used. First, I used Eq [4.9] to select the optimal sampling points for measuring a single set of MT parameters. Second, I used Eq [4.10] to account for the variability of MT parameters within the brain (demonstrated by Sled and Pike, 2004; Tables 4.2 and 4.3). The results showed that the optimal schemes are robust to these settings within the range of MT parameter values observed in the brain. Although each optimization (single set, multiple sets, and hypercube) returned a different set of points, the values of V and V_{max} estimated for schemes 2-4 in Table 4.4 are sufficiently similar (and improved with respect to scheme 1) to conclude that the optimal sampling depends only weakly on the exact parameter settings in the

optimization. Monte Carlo simulations suggest that schemes 2 and 3 provide parameter estimates of very similar precision. Scheme 4, optimized over the hypercube of MT parameter values, provides slightly lower precisions, probably because, although the hypercube covers the range of possible parameter values, the vertices themselves are not necessarily realistic combinations.

It is difficult to be certain whether the optimization found the global minimum configurations for each optimization set. Minimisation of Eqs [4.9] and [4.10] is complicated by the presence of local minima. To reduce the effects of local minima, I used six unique starting points and a method based on simulated annealing, which is particularly suitable for this type of problem. The improvement in the quality of the parametric maps is evident in Figure 4.9, and scheme 2 clearly provides substantial advantages compared to scheme 1. Little further practical improvement is expected from more careful optimization that gets closer to the global minimum, although this may be required for larger N.

The three optimal schemes (2-4) in Table 4.4 include 6 to 7 unique points, while sampling some positions twice. They all include 4 points at high power (of which 3 are unique), and one measurement very close to the Larmor frequency. These results are in contrast with the experimental observations of Sled and Pike (2000), who suggested a regular sampling at constant logarithmic frequency step using only two values of ω_1. Here, however, I restricted my analysis to ten-point acquisition schemes, while Sled and Pike used a different model (Pike, 1996) and a larger number of points. From my experiments it seems likely that, for N>>10, the configuration of ω_1 and Δf that minimises the variance of MT parameters is substantially different from the two-ω_1 scheme they suggest.

It would be interesting to use this method to investigate the dependency of V and V_{max} on N, in order to establish if there is cut-off above which the benefit added by increasing the number of points is small compared to the cost in terms of increased scan time. Using an approach similar to this, although limited to the measurement of a single MT parameter while keeping the rest fixed, Samson et al. (2005) attempted to identify optimal combinations of ω_1 and Δf with small N, demonstrating that N can be reduced to 3 without compromising the standard deviation of the estimated T_2^B, or to 6 without compromising the standard deviation of the estimated f.

The optimization procedure introduced here can be applied equally to alternative more complex models of MT.

4.5 Further improvements to the qMT protocol

In this chapter I have described the work carried out to obtain reliable estimates of MT parameters at both 1.5 T and 3.0 T. The use of a 3D acquisition allows the whole brain to be imaged in clinically acceptable scanning times, while further improvements in terms of SNR were obtained when moving to higher field strength, and when using a multi-channel coil for signal reception. As the precision and the accuracy of the estimated parameters depend on the sampling scheme, i.e. on the selected combinations of ω_1 and Δf used to measure the signal intensities to be fitted by the model, such sampling scheme can be optimized to minimise the variance of the fitted parameters.

A number of additional improvements can be considered. Firstly, since any deviation of the B_0 field from its nominal value results in a deviation from the nominal value of Δf, an *in vivo* B_0 map should also be collected at the scan time and used to correct for this bias (Sled and Pike, 2000). Typically, B_0 mapping is achieved by taking the difference of two phase images collected at different echo times (see Chapter 5). One problem with this approach is in the inability to provide an "absolute" measure of B_0. Accounting for the relative variation is, however, an important preliminary step that allows the quantitative comparison bewteen MT parameters measured in different areas of the brain. More experiments designed for the investigation of the effects of both B_1 and B_0 inhomogeneity on MT parameter estimates are described in the next chapter.

Secondly, as the Marquardt-Levenberg algorithm does not guarantee to find the global minimum of the objective function, a better fit can be obtained by running the fitting several times after perturbing the starting point (Nedjati-Gilani et al., 2005). This clearly comes at the price of increased processing time, however.

Finally, further experiments should be carried out to determine the trade off between the number of points and the minimum SNR in the raw data. This becomes relevant when trying to increase the resolution of qMT data.

4.6 Summary

- Good signal-to-noise in the acquired MT-weighted images is essential for a reliable quantification of MT parameters, with consequences on the minimal scan time.
- The use of a 3D spoiled gradient recalled echo acquisition provides higher signal-to-noise ratio than 2D acquisitions, and can achieve whole brain coverage in clinically acceptable scan times.
- The comparison between *in vivo* normative quantitative MT parameters at 1.5 T and 3.0 T reported here supports the hypothesis that MT parameters are field-independent.
- The large variability in MT parameters within white and grey matter of the brain is consistent with variation in axonal and myelin density in different brain regions.
- Preliminary observations suggest that some dependency of T_2^B on the orientation of a structure with respect to the direction of the B_0 field might exist.
- The precision and the accuracy of MT parameter estimates depend on the sampling points used for the measurements, and can be largely improved by the selection of appropriate schemes.

Chapter 5

Static Magnetic Field (B_0) Inhomogeneities and field mapping

Introduction

When a sample is comprised of different components (e.g. tissue, air and bone), each characterized by a different magnetic *susceptibility* (χ), the magnetic induction, B, is locally altered according to the equation $B = \mu(x,y,z) \cdot H_0$, where H_0 is the magnetic field strenght[1], which remains constant, and μ is the tissue permeability, defined as $\mu=\mu_0 \cdot (1+\chi)$, and μ_0 being the permeability of free space. As a consequence, B shows discontinuities at the tissue interfaces. These phenomena, in combination with imperfect shimming, result in magnetic field inhomogeneity. Field inhomogeneity behaves like a 'background gradient' that affects the phase of the measured signal in an unpredictable fashion. In "conventional" spin-warp imaging, this leads to two types of artefacts: image distortion (i.e. an image of spin density that is spatially different from the physical spin density) and, in gradient echo acquisitions, echo shifting (i.e. a shift of the maximum signal away from the theoretical echo time, which causes signal loss, or signal "drop-out"). Echo-planar imaging (EPI) sequences, which are widely used for diffusion-weighted imaging and functional MRI, are more sensitive than spin warp MRI to these types of artefact. In quantitative magnetization transfer (see Chapters 3 and 4), B_0 inhomogeneities also result in a deviation from the nominal offset frequency of MT pulses. The estimation of the B_0 field is thus important in the context of quantitative MRI.

In this chapter, some of the effects of field inhomogeneities (5.1) and some of the possible solutions (5.2) are reviewed. Next, the effects of field inhomogeneity on qMT are quantified (5.3). The use of fast but undistorted imaging techniques for field mapping is evaluated (5.4), and the effects of undistorting EPI using B_0 mapping on diffusion tensor MRI are investigated (5.5).

---

[1] The magnetic field is usually denoted by the symbol B, although B indicates the magnetic flux density or magnetic induction (measured in Tesla). H is the magnetic field (strength), measured in Ampere/metre. The distinction is often ignored, and both quantities are frequently referred to as "the magnetic field", except in the context of magnetic materials.

5.1 Image Distortion

Image distortion induced by B_0 inhomogeneities varies according to the type of acquisition. The effects are small for a conventional spin-warp experiment, where a line of *k*-space is collected every TR, and they manifest themselves only in the readout direction, as the bandwidth in the phase-encoding direction is effectively infinite. Larger distortions can occur in EPI, particularly in the phase-encoding direction.

Signal drop out typically occurs only in gradient echo imaging, and again the effect is more severe for EPI readout; here I will consider image distortion only. Reviews of off-resonance artefacts both in conventional imaging and in EPI can be found in (Yablonskiy and Haacke, 1994; Reichenbach et al., 1997; Schmitt et al., 1998).

5.1.1 Distortions in spin-warp imaging

As seen in Chapter 2, conventional two-dimensional (2D) MRI is based on the 2D Fourier Transform. From now on it will be assumed that x corresponds to the read-out (RO), or frequency-encoding direction; and y corresponds to the phase-encoding (PE) direction.

Leaving aside T_1 and T_2 effects, the measured signal can be described as:

$$S(k_x, k_y, z) = \iint \rho(x, y, z) \exp\left[i(k_x x + k_y y)\right] dx dy, \qquad [5.1]$$

where we assume standard slice-selection along z, and

$$k_x = \gamma \int G_x dt, \quad k_y = \gamma \int G_y dt, \qquad [5.2]$$

$\rho(x,y,z)$ is the spin density of the sample and γ is the gyromagnetic ratio. k_x and k_y define the spatial frequency domain, or *k*-space. In standard 2D MRI, The RO gradient is typically held constant during the sampling of a line of *k*-space, while the PE gradient is varied, stepwise, for each repetition time (TR), defining the start of the each successive line of *k*-space. Exploiting this formalism, an image of the spin density of the sample can be easily reconstructed by taking the inverse Fourier Transform of $S(k_x, k_y, z)$. In practice *k*-space is sampled discretely and thus Eq 5.2 assumes a discrete form, with summations instead of integrals.

The effects of susceptibility can be represented by $\Delta B\ (x,y,z)$, where $\Delta B(x,y,z)$ is a spatially varying, non-linear function of x, y and z. $\Delta B(x,y,z)$ behaves like a

'background' gradient superimposed onto the linear gradient used for spatial encoding. As a consequence, any field variation beyond the assumed applied linear gradient causes the spins to be spatially encoded at the wrong position. Image distortion is related to the phase evolution of the spins during readout and therefore, in conventional imaging, it only affects the readout direction of the image.

Assuming that locally linear (to a first approximation) background gradients are present in all directions (G'_x, G'_y, G'_z), the phase behaviour during readout can be defined as

$$\phi(t') = -2\pi\gamma(G_x x + G'_x x + G'_y y + G'_z z)t' = -2\pi k_x\left(x + \frac{G'_x}{G_x}x + \frac{G'_y}{G_x}y + \frac{G'_z}{G_x}z\right)t' \quad [5.3].$$

Equation [5.3] implies that spins sitting at position x will be encoded at position x', with

$$x' = x\left(1 + \frac{G'_x}{G_x}\right) + \frac{G'_y}{G_x}y + \frac{G'_z}{G_x}z. \quad [5.4]$$

The effects of background gradients can be made smaller by increasing G_x, To maintain the same field of view, however, this necessitates increasing the bandwidth per voxel, which causes a decrease in signal to noise ratio. Distortions in spin warp imaging are generally small, of the order of sub-voxel shifts after first-order shimming.

5.1.2 Distortions in echo-planar imaging

In EPI, the whole k-space is sampled after a single excitation. In order to achieve this, the G_x gradient varies throughout time in a bipolar fashion, with as many lobes as there are lines in k-space, thus forcing the formation of a series of echoes, or *echo train*. In the most common case, G_y simply consists of very short blips (Doyle et al., 1986), whose duration and amplitude determine the step from one k-space line to the next (δk_y):

$$k_x(epi) = \gamma\int G_x(t)dt, \text{ with } \delta k_x(epi) = \frac{\Delta k_x}{N_x} \quad [5.5]$$

$$\delta k_y(epi) = \gamma\int G_{blip}(t)dt = \frac{\Delta k_y}{N_y}, \quad [5.6]$$

where Δk_y, Δk_y are the total k-space coverage in the frequency and phase encoding direction, and N_x, N_y are the total number of steps. The measured signal is, ideally

$$S(m,n,z) = \iint \rho(x,y,z)\exp\left(-i\frac{m\delta k_x x}{\Delta k_x}\right)\exp\left(-i\frac{n\delta k_y y}{\Delta k_y}\right)dxdy\,. \qquad [5.7]$$

where $-N_y/2<n<N_y/2$ is the line of k-space being sampled, and $-N_x/2<m<N_x/2$ is the current readout step. In the presence of field inhomogeneity, the measured signal becomes

$$S(m,n,z) = \iint \rho(x,y,z)\exp\left(-i\frac{m\delta k_x x}{\Delta k_x}\right)\exp\left(-i\frac{n\delta k_y y}{\Delta k_y}\right)\exp\left\{-i\gamma\int \Delta B(x,y,z)dt\right\}dxdy\,. \qquad [5.8]$$

As k-space is sampled discretely, every readout step is separated by an interval Δt (dwell time), while every PE step is separated by an interval *esp* (echo spacing). Thus, following Jezzard and Balaban (1995) and Jenkinson (2001), we can set in Eq [5.8]

$$\Delta B(x,y,z)\int dt = \Delta B\cdot(TE + n\cdot esp + m\Delta t), \qquad [5.9]$$

where *TE* is the echo time. Since Δt is very small compared to *esp*, the gradient step experienced by successive sampled points in the RO direction is also small, and the effects of susceptibility can be ignored in this direction (they are negligible to the same extent they are in conventional imaging), thus reducing to a one-dimensional problem. *TE* can also be ignored, as it only gives rise to constant phase terms that do not affect the magnitude of the image.

The measured signal can thus be written as

$$S(m,n,z) = \iint \rho(x,y,z)\exp\left(-i\frac{m\delta k_x x}{\Delta k_x}\right)\exp\left(-i\frac{n\delta k_y y}{\Delta k_y}\right)\exp\{-i\gamma n\cdot esp\Delta B(x,y,z)\}dxdy \qquad [5.10]$$

which is equivalent to

$$S(k_x, n\delta k_y, z) = \iint \rho(x,y,z)\exp\left(-i\frac{m\delta k_x x}{\Delta k_x}\right)\exp\left(-in\delta k_y\left(\frac{y}{\Delta k_y} - \frac{\gamma esp\Delta B(x,y,z)}{\delta k_y}\right)\right)dxdy \qquad [5.11]$$

using Eq [5.6] we obtain

$$S(k_x, n\delta k_y, z) =$$

$$y = \iint \rho(x,y,z)\exp\left(-i\frac{m\delta k_x x}{\Delta k_x}\right)\exp\left\{-i\frac{n\delta k_y}{\Delta k_y}\left(y + \gamma N_y esp\Delta B(x,y,z)\right)\right\}dxdy \qquad [5.12]$$

Now, setting

$$y' = y + \gamma N_y esp \Delta B(x,y,z) y' \quad [5.13]$$

$$y = y' - \gamma N_y esp \Delta B(x,y,z), \quad dy = dy'\left(1 - \gamma N_y esp \frac{\partial \Delta B}{\partial y}\right) \quad [5.14], [5.15]$$

where $\left(\frac{\partial \Delta B}{\partial y}\right)$ is the derivative of $\Delta B(x,y,z)$ with respect to y, we obtain

$$S(k_x, n\delta k_y) = \iint \frac{\rho(x, y' - \gamma N_y esp \Delta B)}{\left(1 - \frac{\gamma N_y esp}{\Delta k_y} \frac{\partial \Delta B}{\partial y}\left(x, y' - \frac{\gamma N_y esp \Delta B}{\Delta k_y}\right)\right)} \exp(-ik_x x)\exp(-in\delta k_y y')dxdy' \quad [5.16]$$

showing that the measured k-space represents the Fourier transform of an image where pixels are displaced (in voxel units) by a quantity (y-$\gamma N esp \Delta B$), and modulated by the term $\frac{1}{\left(1 - \gamma N_y esp \frac{\partial \Delta B}{\partial y}\right)}$ (Jezzard and Balaban, 1995; Jenkinson, 2001).

5.2 Basic concept of B_0 field mapping

Different strategies for correcting signal displacement have been proposed. Ideally, the phase error should be measured and corrected for. However, since the susceptibility varies *with spatial location*, the phase error is position dependent, and a single reference scan (i.e. an acquisition with no PE) is insufficient for correcting the geometric distortion. Multi-reference scans, however, can be more effective (Chen et al., 1999). This approach involves the acquisition of a number of reference scans equal to the number of phase-encodings in the image, whose combination allows a k-space filter to be computed which can be used to correct subsequent acquisitions. The obvious disadvantage is the longer acquisition time required for the reference scans. Alternatively, the combination of two magnitude images with orthogonal PE (Chiou and Nalcioglu, 2000) or with opposite PE step (Cordes et al., 2000) can lead to the construction of an undistorted image. However, these methods require the collection of twice as many data as those required by the experiment.

A more elegant approach uses the measurement of the point spread function (PSF), which describes the spatial mapping of an object into an image (Rossman, 1969). In EPI, the PSF is complicated by the effects of relaxation, blurring and

geometric distortions. A general description of the theory and of a pulse sequence for measuring it can be found in Robson et al. (1997). This method is, however, time-consuming and requires specially designed pulse sequences. The most commonly adopted solution for image distortion consists of the measure of the B_0 field (Jezzard and Balaban, 1995) and in the retrospective correction of the distorted data.

5.2.1 B_0 mapping

The direct measurement of the B_0 field can be achieved through an additional standard acquisition (Jezzard and Balaban, 1995), typically an asymmetric spin-echo or a gradient-echo, which can be used retrospectively to correct the image for signal intensity misplacement, according to the equation $y = y' + d$, with $d = \gamma N \cdot esp \Delta B$ (from Eq [5.14]). For example, in a gradient echo experiment, the phase evolution is proportional to $\gamma \Omega TE$, where $\Omega = (\omega + \gamma \Delta B)TE$. Therefore, by acquiring two scans with different echo times, and then taking the difference of their phases, we obtain

$$\Delta\phi = \Omega TE_1 - \Omega TE_2 = \gamma 2\pi \Delta B(TE_1 - TE_2). \qquad [5.17]$$

from which a field-map can be easily derived (Glover and Schneider, 1991) as

$$\Delta B(x,y,z) = \frac{\Delta\phi(x,y,z)}{2\pi\gamma(TE_1 - TE_2)}. \qquad [5.18]$$

Such a field-map allows the shift, $d(x,y,z) = \gamma N \cdot esp \Delta B(x,y,z)$, to be calculated pixel-by-pixel, and EPI images to be corrected. Note that image correction can also be performed directly on the phase in the k-space domain (e.g.: Kadah and Hu, 1997).

One of the major limitations of field mapping consists of the need for "phase-unwrapping". The phase of the MR signal is defined within the range $(-\pi,\pi)$, and any value outside this range will be 'wrapped around'. When calculating the field inhomogeneity it is necessary to retrieve the information about this phase offset, and to minimize discontinuities within the field, through a phase-unwrapping algorithm. Due to the presence of noise, this operation can be quite delicate. This problem is well known also in fields other than MRI (for example in interferometric synthetic aperture RADAR), where the phase is generally measured in a single dimension. Some software packages for field-mapping correction of EPI provide unwrapping algorithms specifically designed for this purpose. Mark Jenkinson's software (Jenkinson, 2003), available at http://www.fsl.ax.ac.uk, allows arbitrary N-

dimensional phase maps to be unwrapped, and provides very good results with phase maps deriving from asymmetric spin-echo based acquisitions (i.e. smooth variations). For gradient-echo based phase-maps, a better approach consists of directly unwrapping the phase difference, $\Delta\phi$, rather than the single phases, since, if the difference in echo time is not too large, many of the discontinuities will be present in both images and therefore will cancel out. This is the strategy used by the algorithm provided by Cusak et al. (2002), available at http://www.mrc-cbu.cam.ac.uk/Imaging/.

Although theoretically it is possible to use the field-map to estimate the derivative of $\Delta B(x,y,z)$ (see 5.1.2), and therefore to correct image intensity as well as distortion, in practice this often leads to worse artifacts, as such estimates are generally much noisier than the original images (Jenkinson, 2001).

5.3 Effects of field inhomogeneities on quantitative MT imaging

The correction of off-resonance artifacts in EPI is currently the main application of static field mapping. However, it may also be useful for other quantitative applications. Since quantitative MT (see Chapter 4) relies on fitting a non-linear model to a series of MT weighted images collected using MT pulses of variable amplitude (ω_1) and offset frequency (Δf), any imperfection in the time-varying magnetic field (B_1) will result in a deviation from the nominal flip angle and ω_1, while any imperfection in the B_0 field will result in a deviation from the nominal value of Δf. Both effects can introduce a spatially variable bias in the estimated parameters, and both are likely to be more pronounced at 3.0 T than at 1.5 T. I discussed the effects of B_1 inhomogeneities on qMT (Chapter 4); here I present an experiment designed to quantify the errors introduced by both B_1 and B_0 field inhomogeneities into qMT parameters measured at 3.0 T.

5.3.1 Materials and Methods

The same MT model (Henkelman et al., 1993; Ramani et al., 2002) and the same notation introduced in Chapter 4, and briefly summarized here, will be used in the following paragraphs. From the Henkelman-Ramani model 6 independent quantities can be derived: RM_0^A, $f/R_A(1-f)$, T_2^B, $1/R_AT_2^A$, R_B, and gM_0^A. A and B label

respectively the liquid and the semisolid pools, and f represents the bound proton fraction (Ramani et al., 2002).

A single subject (male, 39 years) was scanned on a 3.0 T system using the 3D MT-weighted fast spoiled gradient recalled echo (SPGR) sequence described in Chapter 4 (TR/TE=25.8/2.7 ms, flip angle=5°, Gaussian MT pulses, duration=14.6 ms) (**A**). The sequence collects 10 volumes with 2 values of ω_1 and 5 values of Δf for each ω_1. In addition to the MT data, (**B**) two 4-shot spin-echo EPIs (TR/TE=15000/20 ms, flip angles=60° and 120°, matrix 64x64), (**C**) 2 fast 3D SPGRs (TR/TE1/TE2=25.8/2.7/5.4 ms, flip angle 5°) and (**D**) 3 fast 3D SPGRs (TR/TE=6.0/2.8 ms, flip angles 15°, 7°,and 3°) were collected. Acquisition matrix (256x96), FoV (24x18 cm^2) and number of slices (28) were the same for all sequences unless otherwise specified. Slice thickness was 5 mm for all the SPGR sequences and 4 mm with 1 mm gap for the EPI. The body coil was used for signal transmission and the 8 channel head coil was used for reception, with the exception of sequence C, where the body coil was used for reception as well as transmission. This was done in order to preserve the complex data and avoid the reconstruction automatically done on the scanner when using multi-channel receiver coils.

After image co-registration, B_1 maps were obtained from sequence B using the double angle method (Stollberger and Wach, 1996; outlined in Chapter 4) and the resulting maps were smoothed using a 3rd order polynomial fitting routine. Maps of the B_0 deviation from the value in the centre of the head were calculated from the phase images obtained from sequence C, using Cusack's software (Cusack and Papadakis, 2002), including phase-unwrapping. This algorithm was chosen because it performs better than others such as "*Prelude*" (Phase Region Expanding Labeller for Unwrapping Discrete Estimates, Jenkinson et al., 2003) with phase maps obtained from gradient echo acquisitions. T_1 maps were calculated by fitting the signal in sequence D as a function of the flip angle, after it was corrected on a pixel-by-pixel basis for B_1 inhomogeneities (see Chapter 4 for details on processing). Finally, since B_0 and both transmit and receive B_1 inhomogeneities also cause the signal intensity (and therefore the SNR) in the MT weighted images to vary with position, the least MT-weighted volume (from sequence A) was convolved with a Gaussian low-pass filter to produce a map of the slowly varying signal intensity (independent of the anatomy). Assuming such an image to be directly correlated to the SNR in the raw data, and the SNR to be inversely correlated to the standard

deviation (SD) of the measured signal in a given voxel, a relative SD map was obtained by taking the inverse of this image. The local SD values can then be used to compute the chi-square merit function during the voxel-by-voxel fitting of the model to the data, as opposed to the "standard" procedure, where the SD is assumed to be the same throughout the brain. The Henkelman-Ramani model was then fitted to the data 5 times using the Marquardt-Levenverg algorithm (keeping R_B fixed and equal to 1, and modelling the semisolid pool absorption lineshape with a superlorentzian, as described in Chapter 4): 1) without any correction; 2) correcting ω_1 only for B_1 inhomogeneities; 3) correcting Δf only (for B_0); 4) correcting both ω_1 (for B_1) and Δf (for B_0); and 5) finally, correcting both ω_1 and Δf and accounting for the pixel-by-pixel varying SNR in the fitting algorithm. f maps were extracted from the fitted data as described in Chapter 4.

5.3.2 Results

Typical B_1, B_0 and SD maps are shown in Fig 5.1.

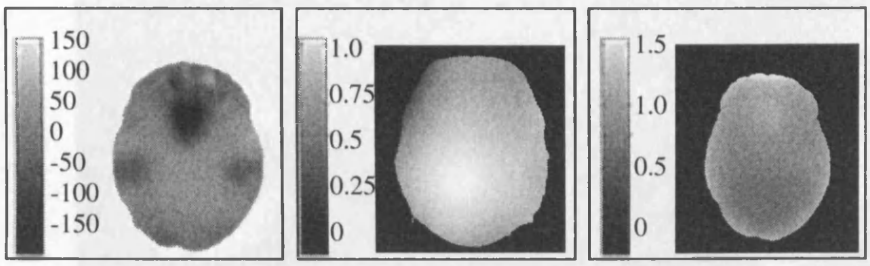

Fig 5.1 B_0 (left, in Hz), B_1 (centre, relative to nominal value) and SD (right, relative to average value) maps of the same slices.
(Note that B_0 and B_1 maps extend to the skull, while SD mapsis masked to include the brain only, hence the difference in size).

The parameters estimated by the fifth fitting procedure (including all three corrections) were used as a reference to calculate the pixel-by-pixel percentage difference in MT parameters (RM_0^A, T_2^B, $1/R_AT_2^A$, and f) estimated by the other three procedures. The exclusion of the information on the local SD did not result in changes of more than 1% in any of the parameters. f estimates appeared particularly robust to B_0 field inhomogeneities, showing minimal errors only in areas where the change in magnetic susceptibility is abrupt. Conversely, B_1 field variations resulted

in differences in f values as large as 50% or more. An opposite pattern characterised T_2^B estimates, which appeared more sensitive to B_0 than to B_1 field inhomogeneities. For T_2^B, the error was always within 10% in most areas of the brain. Both B_0 and B_1 field inhomogeneities appeared to affect the estimates of RM_0^A and $1/R_AT_2^A$ (see Fig 5.2).

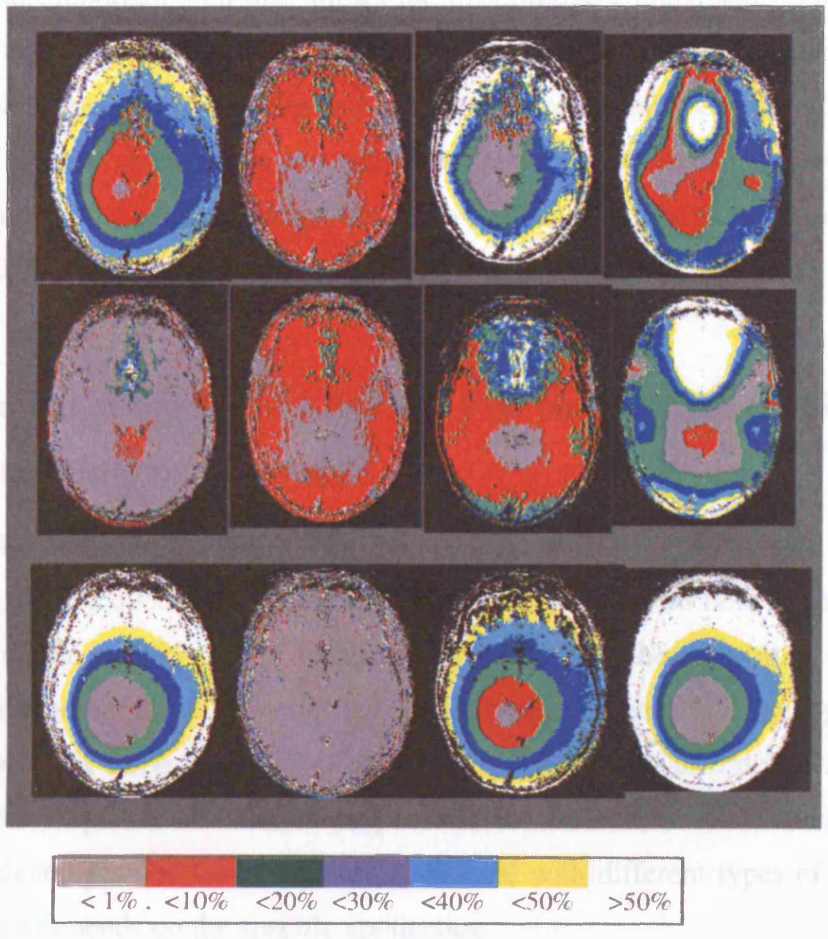

Fig 5.2. Maps of the percentage difference in the estimated MT parameters compared to the fully corrected values.

From left to right: f, T_2^B, RM_0^A, and $1/(R_AT_2^A)$. Top row: no correction is performed; Middle row: B_1 correction is performed, but no B_0 correction is performed; Bottom row: B_0 correction is performed, but no B_1 correction is performed.

5.3.3 Conclusions

I have shown here that accounting for both static and RF magnetic field inhomogeneities is essential to obtain reliable estimates of MT parameters at 3.0 T. If

only f is estimated, however, B_0 field mapping can be skipped in the interest of time. It is not surprising that a shift of few fractions of *ppm* in the frequency offset does not significantly affect the estimate of f, given the broad spectrum of the macromolecular pool (see Fig 5.1). RF absorption, on the other hand, is very sensitive even to small changes in T_2^B, particularly in the range of frequency offsets used for this experiment, as reflected by these results. Accounting for the field variation is an important step that allows the quantitative comparison between MT parameters measured in different areas of the brain. One remaining question is whether any B_0 mapping sequence can be used to represent the field under MT saturation. In some cases, when large crusher gradients are used in the MT pulse sequence, the effect of eddy currents on the B_0 profile should be taken into account (Sled and Pike, 2000).

5.4 Evaluation of the use of Ultra low Flip angle RARE (U-FLARE) for rapid acquisition of B_0 maps

5.4.1 Introduction

Any pulse sequence where the image phase is sensitive to field variation can be used to obtain a field map. I have already mentioned the possibility of using conventional gradient-echo or asymmetric spin-echo acquisitions. For the experiment described in 5.3, a three-dimensional gradient-echo was used, in order to keep the timing of the sequence as similar as possible to those of the MT acquisition. However, advantages and limitations are associated with different types of readout, and the choice depends on the specific application.

One of the major applications of EPI is functional MRI (fMRI), where scanning time is often an issue, and the duration of any additional acquisition should be minimised. For this reason, the use of EPI field-maps has been proposed (Reber et al., 1998; Gruetter and Tkac, 2000; Hutton et al., 2002). Beside the advantage of acquisition speed, fMRI and field-map acquisition can be combined in a single, double echo acquisition, where the longer echo is also used for encoding the fMRI experiment (Hutton et al., 2002), while the shorter echo is chosen to be as short as possible. This approach has the double advantage of producing a field-map for every time point of the fMRI series, with the same spatial characteristics of the images to

be corrected and inherently coregistered to such images. By contrast, gradient-echo or spin-echo based field-maps (which I will call *conventional* field-maps, for the sake of brevity), require longer acquisition times, and generally need to be coregistered with the EPI volumes to be corrected. However, since they do not share the same geometric properties of EPI, an accurate registration can only be achieved if the magnitude of the field-maps is distorted on a pixel-by-pixel basis by an amount $d(x,y) = \gamma N \cdot esp \Delta B(x,y,z)$. Once distorted, it can be matched to the EPI volume to be corrected, the registration parameters can then be applied to the field-map, and the distortion can finally be compensated. As geometric distortion has been shown to be modulated by motion (Jezzard and Clare, 1999; Andersson, 2003), this latter approach is likely to neglect the 'time-varying' component of field-dependent distortions. On the other hand, although EPI field-maps have several advantages over conventional field-map, they have a major disadvantage - if the field-maps are distorted, as they are if created using EPI, the measured field needs to be inverted in order to estimate the actual field. Paradoxically, information is lacking (i.e. signal intensity is low) exactly where it is most needed, i.e., where the field inhomogeneities show the steepest variation. In these regions, some kind of interpolation is needed to retrieve the information lost. Furthermore, it has been shown (Hutton et al., 2002) that for small movement, the residual variation in the serial field-maps are of the same order in uniform as well as non-uniform regions of the fields, and that time-varying distortion correction adds variance to the time series rather than reducing it. In practice, it seems that there is too much variability between successive EPI field-maps to use this method to correct for time-varying distortions. An alternative pulse sequence, also characterised by high acquisition speed, is ultra-fast low angle RARE, or U-FLARE (Norris, 1991). U-FLARE has the advantage over EPI of being less sensitive to field inhomogeneities and therefore it is an ideal candidate for field-map acquisition. Here I present a series of experiments to evaluate the feasibility of B_0 field-mapping using U-FLARE.

5.4.2 The U-FLARE sequence

5.4.2.1 Basic Principles

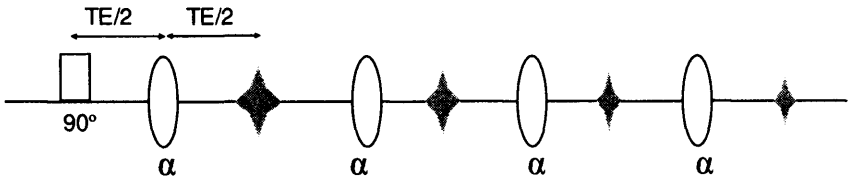

Fig 5.3. The U-FLARE sequence. Modified from Norris (1991).

The original rapid acquisition with relaxation enhancement (RARE) (Hennig et al., 1986) pulse sequence is a multi-echo spin-echo experiment, where each phase encoding step is acquired using a different echo (see also Chapter 2). The T_2 contrast in this type of sequence is controlled by shifting the echoes corresponding to the desired echo time to the centre of *k*-space. While being efficient, single-shot RARE has two major disadvantages: the mixture of T_2-weightings due to different TEs (which vary between lines of *k*-space (Hennig et al., 1986)), and the amount of power deposition due to the 180° pulses used to refocus the signal a sufficient number of times. Ultra-fast low-angle RARE, or U-FLARE (Norris, 1991), is a variant of single-shot RARE where refocusing angles smaller than 180° are used to mitigate the latter problem. The basic U-FLARE pulse sequence diagram is shown in Fig 5.3. A 90° pulse is used to generate magnetization in the transverse plane. Typically Gaussian refocusing pulses of amplitude α are used. Gaussian pulses are preferable to sinc pulses because of the shorter duration required to obtain a particular flip angle at a particular maximum amplitude. The use of this type of pulses can result in a variable flip angle through the slice, whose effects should thus be considered.

Since refocusing angles smaller then 180° also generate a longitudinal component that is brought into the transverse plane by the following pulses, the effective decay of the transverse magnetisation is a complicated function of T_1, T_2, α, and TE. Angles smaller than 180° can generate a very large number of coherence pathways (Hennig et al., 1988), i.e. following each pulse, the magnetisation is transformed into a number of components which are again decomposed at the next pulse. Although the number of coherence pathways is large, they can be divided into two families, according to their parity: odd and even parity pathways have

respectively spent an odd or an even number of TEs in the transverse plane (Norris and Börnert, 1993). Even and odd echoes can add coherently (maximising the signal) or incoherently (destroying the signal). The first condition for coherent addition is that the two echoes occur simultaneously. This can only be achieved by the use of perfectly balanced read out gradient (coherent U-FLARE). The phase relationship between the two families also affects the amplitude of the measured signal, which is maximal when the transverse magnetization vector occurring TE/2 prior to the first refocusing pulse and the B_1 vector associated with such a refocusing pulse are parallel, i.e. when the Carr-Purcell-Meiboom-Gill (CPMG) condition is satisfied. In situations of poor B_0 homogeneity the degree of coherent addition can be spatially variable. Possible solutions consider shifting the one echo group out of the acquisition window by the use of spoiler gradients (displaced U-FLARE); or the use of an imbalanced read dephase gradient (split-echo U-FLARE). Both of these solutions imply the loss of half the signal compared to coherent U-FLARE. In multi-shot experiments, phase cycling schemes can also be used (Zur and Stokar 1987) to eliminate either family of echoes.

5.4.2.2 Application to field-mapping

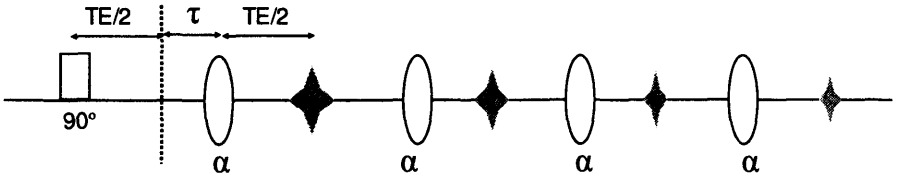

Fig 5.4. Susceptibility-weighted U-FLARE. Modified from Niendorf (1999).

In order to measure the B_0 field through the MR signal, the phase accumulated at the echo time in at least one of the two images collected (see above) must vary linearly with the frequency and therefore with B_0. In a regular spin-echo experiment this is not the case, as the phase accumulated during the first TE/2 is perfectly balanced by that accumulated during the second TE/2. A dependency on B_0 can be achieved by shifting the centre of the gradient echo with respect to the centre of the spin echo (for a theoretical description of the asymmetric spin echo sequence, see Stables et al., 1998). A similar approach can be implemented in U-FLARE by

shifting the first refocusing pulse by an evolution time τ with respect to TE/2. A schematic representation is shown in Fig 5.4. This variant of the sequence has been used for susceptibility-weighted imaging (Niendorf, 1999) and chemical shift phase encoding (Dreher and Leibfritz, 1999). The use of coherent U-FLARE is incompatible with the use of an evolution time greater than zero, as this introduces some T_2* weighting. However, both displaced and split-echo U-FLARE acquisitions can be used in this case, and the displaced version was used for the experiments described below. The calculation of a B_0 map thus require the acquisition of two images, with differing evolution times, in the work described here $\tau_1=0$ and $\tau_2\neq0$, as explained below.

The use of this acquisition for field-mapping was first validated using a chemical-shift phantom, and then used *in vivo* to correct fMRI data. fMRI is a technique aiming at detecting changes in magnetic susceptibility due to changes in oxygenation of haemoglobin. An overview of fMRI concepts can be found in Appendix A, but in brief: an increase in neuronal activity causes an *increase* in blood flow. This results in an *excess* of oxygenated haemoglobin beyond the metabolic need, thus *reducing* the proportion of paramagnetic deoxyhemoglobin in the vasculature, and therefore the susceptibility differences in the vicinity of veins and capillaries. The consequent increase of MR signal, called blood oxygenation level dependent (BOLD) contrast, can be used to detect human brain activation. Because the effect is very small, fMRI experiments require the collection of several images in a short time, which are then processed using statistical models. Gradient echo EPI is therefore the ideal acquisition sequence for this type of experiment.

5.4.3 Validation using a chemical-shift phantom

5.4.3.1 Phantom description

The pixel shift in the PE direction due to susceptibility distortions is proportional to the local frequency offset $\Delta\nu$ where

$$\Delta\nu = \gamma\Delta B(x, y, z). \qquad [5.19]$$

A similar signal displacement can occur in EPI whenever there is a difference in resonance frequency between objects in the image, for instance due to the *chemical shift*.

The chemical shift offset manifests itself most commonly in MRI data between water and fat and is due to a frequency offset $\Delta\nu_{cs}$ between water and fat signals. The offset mimics a susceptibility induced offset, with the same sensitivity to acquisition parameters as the susceptibility induced distortions, but is spatially constant, measurable, and well defined. For an EPI-based sequence, the total number of pixels by which signal from two species differing in resonant frequency by $\Delta\nu_{cs}$ are shifted relative to each other is given by

$$N_{shift} = \Delta\nu_{cs} N_y/BW_y \quad = \Delta\nu_{cs} N_y \, esp \qquad [5.20]$$

Where N_y and BW_y are respectively the total number of pixels and the bandwidth in the PE direction. Using a phantom consisting of two bottles, one filled with water and one filled with oil, (shown in Fig 5.5) (Boulby et al., 2004) the pixel shift on EPI can be measured and compared to that predicted by different field-mapping sequences, thus providing an evaluation of their performance.

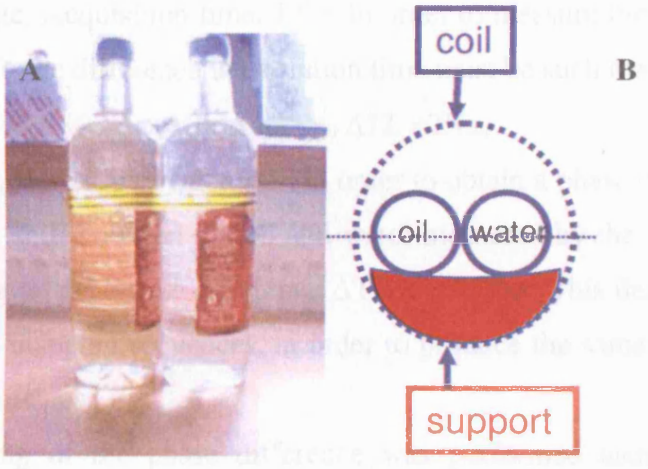

Fig 5.5. Chemical-shift phantom consisting of two identical bottles, one filled with water and the other filled with oil (A). Position in the scanner (B).
If positioned in the scanner using a support to achieve perfect alignment, the shift measured on the images quantifies the frequency shift between the two samples.

5.4.3.2 Materials and Methods

All measurements were obtained at 1.5 T (SIGNA Horizon Echospeed, General Electric, Milwaukee, USA). The resonant frequency difference between the oil and water was first measured using a localized short-TE point-resolved

spectroscopy (PRESS) sequence (TE/TR=30/3000 ms) in a large voxel covering both the oil and water bottles. The spectroscopic chemical shift value acts as a "gold standard" against which to compare the image-derived chemical shift value which in turn is found by imaging the adjacent oil and water phantoms, and calculating the chemical shift from the measured shift (in pixels) and from the knowledge of the image's bandwidth. The same phantom was also imaged using a single-shot spin-echo EPI (TE/TR=40/6000, esp=832 μs, matrix=64x64, FOV=24x24 cm^2) and three different types of field-mapping sequences: a spin-echo repeated twice, once with a symmetric echo (SSE) and once with an asymmetric echo (ASE) (SSE TE= 20 ms, ASE TE = 23.75 ms (evolution time= 3.75 ms), TR: 1000 ms, FoV: 240x180 mm, matrix: 256x128; Acquisition time: 3' 36"); a 2D gradient-echo (TE1: 20 ms – TE2: 23.75 ms, TR: 1000 ms, FoV: 240x180 mm, matrix: 256x128, Acquisition time: 3' 20"); and a displaced U-FLARE retaining only the even echoes (TE1:35 ms, TE2:38.75 with evolution time of 3.75 ms, TR: 6000 ms, FoV: 240x180 mm, matrix: 128x96; refocusing pulses angle 135°, 6 dummy cycles discarded in order to reach pseudo steady state, Acquisition time: 12"). In order to measure the phase difference due chemical shift, the difference in evolution time must be such that

$$\Delta\varphi = 2\pi\, \Delta\nu_{oil\text{-}water}\, \Delta TE \neq 2N\pi, \qquad [5.21]$$

for any integer N. Here it was calculated in order to obtain a phase difference of $3/4\pi$ for the frequency shift between the oil and water measured by the MRS experiment (≈200 Hz), giving an echo time difference ΔTE = 3.75 ms. This delay was the same for all three field-mapping sequences, in order to produce the same phase difference between pairs of images.

Unwrapping of the phase difference was performed using the procedure described by Cusack and Papadakis (2002), and maps of the voxel shift were created as described by Cusack et al. (2003) (http://www.mrc-cbu.cam.ac.uk/Imaging/field-map_undistort). This software was chosen because its unwrapping algorithm performs well with gradient echo phase maps. The actual voxel shift measured on the EPI images was then compared with the expected shift calculated from the frequency difference, and with the average voxel displacement estimated by the three field-maps.

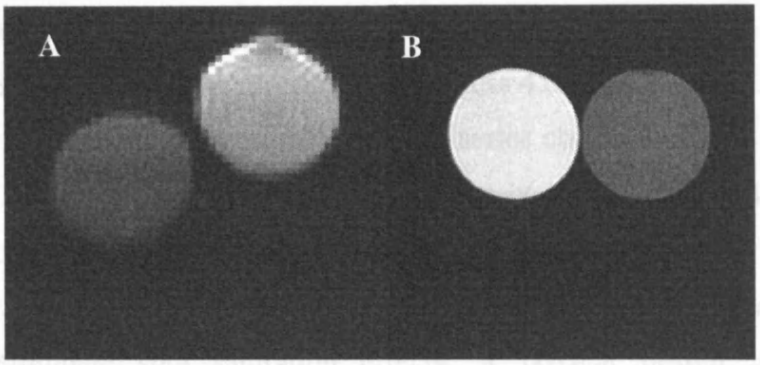

Fig 5.6. Typical EPI (A) and spin-echo (B) images of the chemical shift phantom.

The voxel displacement caused by chemical shift is evident on the EPI scan. Note that the spin-echo image is T_1-weighted, hence the different contrast between the two acquisitions.

An example EPI image of the phantom is shown in Fig 5.6 A, while a conventional spin-echo image of the same slice (demonstrating that the samples are aligned) is shown in Fig 5.6B.

5.4.3.3 Results and Conclusions

The difference between resonant frequencies of the water and lipid lines, measured on the spectrum, was $\Delta\nu \approx 200$ Hz. The expected voxel shift, according to $\Delta\nu$ is thus $\Delta\nu \cdot esp \cdot N_y \approx$ **10.5** voxels. The voxel shift actually measured on EPI was, consistent for all 5 slices, approximately **11** voxels. The pixel shift predicted using the field-maps (averaging across the three central slices) was 10 for the spin-echo acquisition, 11 for the gradient-echo acquisition and 10.1 for the U-FLARE acquisition.

Experiments on the chemical-shift phantom demonstrated that the pixel shift estimated by the U-FLARE field-map is in good agreement with that predicted theoretically and comparable with that estimated by SE and GE field-maps.

5.4.4 In vivo experiments and application to functional MRI

5.4.4.1 Subject and MRI

A single 37 year old male healthy subject was scanned using:

a) An oblique-axial spin-echo EPI (TE/TR=40/6000, echo-spacing=1536 μs, matrix=128x128, 24 slice locations, slice thickness 4.6mm, FOV=24x24 cm^2).

b) A similarly orientated functional MRI (fMRI) series obtained using a gradient-echo EPI (TE =40 ms, echo-spacing=832 μs, matrix=64x64, FOV=24^2 cm^2, 30 scan locations, slice thickness 4.6 mm, interscan interval=4.5 s). The acquisition consisted of 69 repetitions, with the first 9 volumes discarded in order to eliminate spin saturation effects. A box-car design was used alternating two conditions: the subject was asked to perform a finger-tapping task alternating left and right hand with timing controlled by the operator (allowing 27 seconds for each condition).

c) The 3 field-mapping pulse sequences described in 5.4.3. In this case, a ΔTE (evolution time) of 4.54 ms was chosen in order to minimise the chemical shift between water and lipids. The acquisition parameters were the same as in the phantom with the exception of the number of slices (30), the slice thickness (4.6 mm), and the second TE (24.54 ms). In order to cover the whole brain, the number of acquisitions for the U-FLARE field-map was increased to 4, with a consequent increase of the scan time to 42 sec.

d) A coronal inversion-recovery 3D-SPGR (TE/TR/TI=4.3/15.5/450, matrix=256x192x124, in-plane FOV=240x180, slice thickness 1.5mm).

5.4.4.2 Image Analysis

All images obtained with sequences a) and c) were skull-stripped using the brain extraction tool (BET) (Smith, 2002), a freely available tool part of the fMRIB software library (FSL) (http://www.fmrib.ox.ac.uk/fsl). The *in-vivo* field-maps were calculated from the 3 sets of images from c) with the same software package used for the phantom data. The magnitude data from the field-mapping sequences were distorted according to Eq [5.14] and co-registered to the distorted EPI using a rigid-body transformation (Smith, 2002). The transformation was then applied to the field-maps and EPI images were corrected on a voxel-by-voxel level.

The fMRI analysis was done in SPM2 (Wellcome Dept of Cognitive Neurology, http://www.fil.ion.ucl.ac.uk/spm). Motion correction was performed by aligning all the EPIs in the fMRI series to the first volume, saving the realignment parameters. The mean image was unwarped using the U-FLARE field-map, and the correction was applied to all the realigned volumes. Then both the corrected and the

uncorrected mean images were normalised to the space defined by the Montreal Neurological Institute (MNI) template using the EPI template in SPM. The transformation parameters were applied to all the realigned images (before and after correction) which were then resampled to a resolution of $2 \times 2 \times 2$ mm^3. Normalisation in SPM2 is achieved by an affine transformation followed by 16 non-linear iterations. Data sets were smoothed with an 8-mm Gaussian isotropic kernel. Finally, statistical parametric maps were generated using the general linear model and the theory of the Gaussian random fields (Friston et al., 2005). The analysis was done in normalised space. The expected responses were modelled in an experimental design matrix by convolving a box-car function with a standard haemodynamic response function (HRF). The realignment parameters were entered as regressors in the design matrix. A 128 sec high pass filter was used to remove physiological noise. A first order autoregressive model was used to account for temporal autocorrelation. Two T contrasts were used (left>right and right>left). The family-wise (FWE) error correction was applied to reduce type I error due to multiple comparisons. Only activations exceeding a significant threshold $P < 0.05$ after FWE correction were considered significant.

5.4.4.3 Results

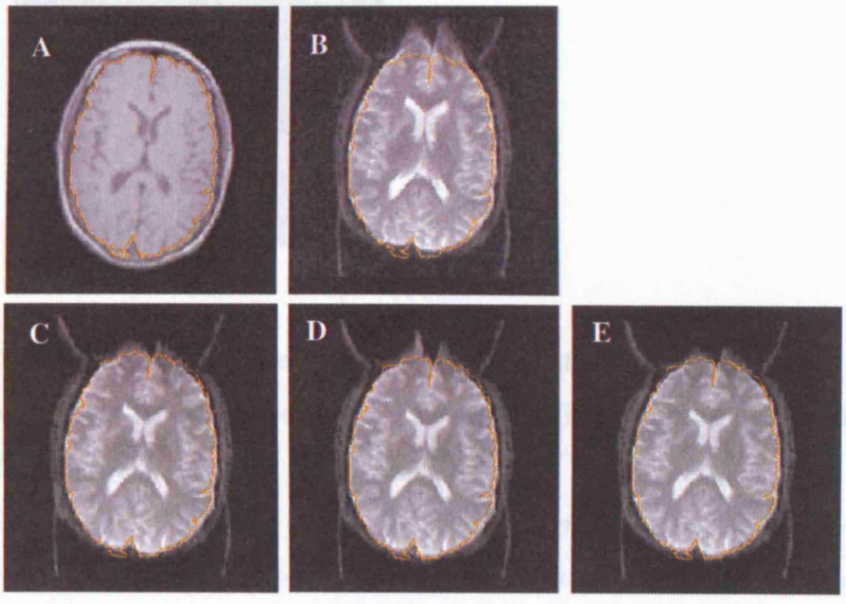

Fig 5.7. Top row: Spin-echo (A) and distorted EPI (B) of the same slice. On the bottom raw: EPI corrected using a spin-echo field-map (C), EPI corrected using a gradient-echo field-map (D) and EPI corrected using a U-FLARE field-map (E).

Figure 5.7 shows a conventional spin-echo (A) and EPI image from sequence a) (B) before correction. On the bottom row, the same figure shows the EPI corrected using a SE field-map (C), the EPI corrected using a GE field-map (D), and the EPI corrected using a U-FLARE field-map (E). The outline of the brain was taken from the anatomical images and is superimposed on the EPIs to show the improvement in shape match.

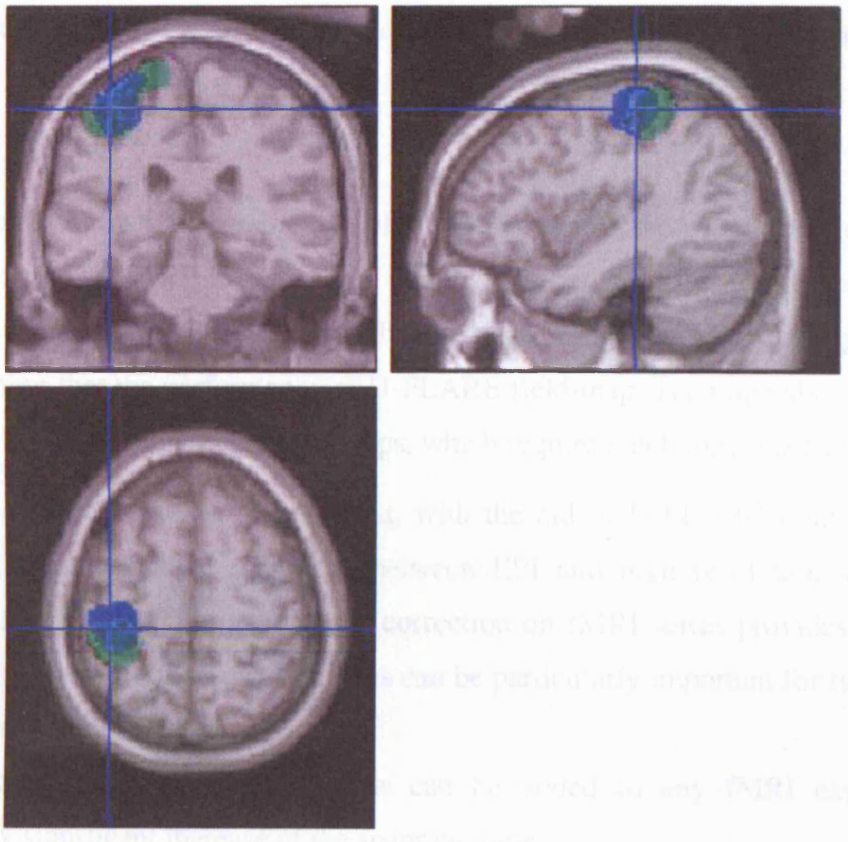

Fig 5.8. fMRI activations obtained for the contrast 'left>right' estimated before (greeen) and after (blue) correcting EPI data for field inhomogeneity using a U-FLARE field-map.

The overlap is indicated by the shaded area. The opposite contrast (right>left) gave similar results on the contralateral side. Activations are superimposed on a normalized 3D IR-SPGR.

The fMRI analysis showed significant activations for both contrasts. Significant activations were found in the ipsilateral cerebellum, in the contralateral

primary and sensory motor cortex (Broadman areas 3 and 4), and in the contralateral medial frontal gyrus (Broadman areas 6 and 31). The clusters of activation were similar for distortion-corrected and uncorrected data. However, when activations are superimposed on the normalized 3D SPGR, it appears that the after-correction activations in the primary motor cortex are located in the pre-central gyrus, while the before-correction activations appear slightly shifted towards the post-central gyrus (Fig 5.8). This suggests that normalization works better when EPIs are corrected for geometric distortions, resulting in a more reliable localization of functional activity even when the active areas are far from regions sensitive to magnetic susceptibility.

5.4.5 Conclusions

I have shown that reliable field-maps covering the whole brain can be acquired using U-FLARE in less than a minute, without the distortion typical of EPI field-maps. The validity of this approach was tested using a chemical shift phantom, demonstrating that the performance of U-FLARE field-maps is comparable with that of spin-echo and gradient-echo field-maps, which require much longer scan times.

In vivo experiments showed that, with the aid of U-FLARE field-mapping correction, the anatomical mismatch between EPI and high resolution structural images is minimized. The use of such correction on fMRI series provides a better anatomic localization of activations. This can be particularly important for functional mapping of cognitive tasks.

Such field-mapping acquisitions can be added to any fMRI experiment without any significant increase of the scanning time.

5.5 Evaluation of the use of B_0 maps to correct diffusion-tensor data

A full overview of diffusion-weighted (DW) MRI principles can be found in Appendix B, and only a brief introduction is given here. DW MRI permits the measurement of water self-diffusivity and, as a consequence of the interactions between water molecules and obstacles that hinder their motion, gives information about the size, orientation and shape of brain structures in vivo. The measurement of the water diffusion coefficient has proven useful in the study of both normal and diseased brain, particularly after the introduction of diffusion tensor (DT) MRI

(Basser et al., 1994). Furthermore, the ability of DT-MRI to reflect the underlying tissue structures leads to the possibility of tracing fibre tracts in white matter (*diffusion tractography*), based on the assumption that the principal direction of diffusion is parallel to the main fibre direction in every voxel.

DT MRI is both time-consuming, as it requires the collection of several images with diffusion gradients applied along several directions, and highly susceptible to bulk motion, resulting in ghost artefacts in the phase-encoding direction. For these reasons, the acquisition of DT MRI data is usually performed by using a rapid, single-shot technique such as EPI, and therefore it is prone to susceptibility artifacts. In principle a field-map-based correction should be applicable to DT-MRI data. As discussed in the previous sections of this chapter, the use of field-maps allows the geometric properties of the imaged object to be restored. When dealing with quantitative MRI techniques such as DT MRI, however, the effects of susceptibility on signal intensity must also be considered. Although in theory it is possible to retrieve the original signal intensity distribution, in practice this is problematic due to the rapid susceptibility variation across the object. In some cases inappropriate assignments of intensity values to image voxels can lead to severe artifacts, particularly when the signal arising from different anatomical locations collapses into a single image voxel. The aim of the experiment described below was to evaluate the use of field-mapping for correcting DT MRI data.

5.5.1 Methods

5.5.1.1 MRI

A single subject (a 37 year old male) was scanned on a 1.5 T SIGNA Horizon Echospeed scanner (General Electric, Milwaukee, USA). Diffusion weighted echo planar images (DW-EPI) were acquired in the axial plane (TE=96 ms, matrix=96x96, echo-spacing=704 μs, field of view=22x22 cm^2, slice thickness=2.3mm, Δ=40 ms, δ=34 ms, resulting in a maximum b factor of 1000 s/mm^2). The acquisition of diffusion tensor images was gated to the cardiac cycle using a pulse oxymeter (Wheeler-Kingshott et al., 2002). Gradients for diffusion sensitisation were applied in 54 non-collinear directions (Jones et al., 1999), and six images with no diffusion weighting (b_0) were collected for each slice, giving a total of sixty images per slice. Images were interpolated to a 128x128 matrix by zero filling during reconstruction. The total number of slices was 60.

Two field-mapping displaced U-FLARE sequences with different TEs (TE_1=36ms, TE_2= 40.54ms, evolution time=4.54ms, TR=6000ms, matrix 128x96, FoV=240x190 mm, slice thickness 4.6mm, number of slices = 30) were also collected during the same scanning session.

5.5.1.2 Image processing

Diffusion weighting usually results in significant eddy currents induced by the strong gradient pulses applied. The eddy currents produce an additional type of geometric distortions with different characteristics to those caused by susceptibility changes, which affect images with different diffusion-weightings differently. This type of distortion can be approximated as the superimposition of a translation (caused by a residual gradient in the slice-selection direction and B_0 shift), a shear (caused by a residual gradient in the frequency encoding direction), and a scaling (due a residual gradient in the phase-encoding direction). In order to remove these effects and any misalignment due to involuntary motion between different diffusion weightings, all the DW-EPI images were first co-registered to the corresponding b_0 images using a 2D affine transformation (Symms et al., 1997). Next, the diffusion tensor was estimated from the raw data (both before and after field-map correction), according to Basser et al. (1994). The eigenvalues and eigenvectors were obtained by matrix diagonalisation, and maps of the mean diffusivity (MD) and fractional anisotropy (FA) were derived. All diffusion processing was performed using the Camino software package (Cook et al., 2006; available at www.cs.ucl.ac.uk/reseach/medic/camino).

The U-FLARE images were resampled to the same resolution as the DW-EPI scans. Maps of $\Delta B(x,y,z)$ were obtained from the U-FLARE phase images after unwrapping using the FSL software (Jenkinson, 2003). The information available from these maps was used to warp the magnitude images from the U-FLARE scan to match an EPI scan (after correction for eddy current effects). By co-registering these warped scans to the b_0 images of the DW-EPI (which have a similar T_2 weighted image contrast), the transformation mapping the field-map to the same space as the DW-EPI was obtained. Every diffusion weighted volume was then unwarped using the shift map calculated for the b_0 images.

5.5.1.3 Tractography algorithms

In order to estimate the effects of the intensity modulation on tractography (see Appendix B), the inferior longitudinal fasciculus was reconstructed from the corrected DW-EPI data only. Two different algorithms, both implemented in Camino, were used. Firstly, a deterministic approach was used to derive the streamlines passing through a seed region, comprising a number of seed points (see below). Second, the Probabilistic Index of Connectivity (PICo) algorithm (Parker et al., 2003) was used to derive maps of probability of connection of the same seed points to the rest of the brain. PICo considers multiple pathways emanating from a seed region (i.e. a group of voxels in a region of interest) and from each point along the reconstructed trajectories. Due to the presence of noise in the data, there is some uncertainty associated with the determination of the principal direction of diffusion. The algorithm accounts for this limitation by generating a probability distribution function (PDF) from the diffusion tensor of each voxel, which provides voxel-wise estimates of confidence in fibre tract alignment and uses these in tract formation. Streamline-based tracking iterations using the PDFs from a chosen seed point are then performed and repeated in a Monte Carlo fashion to produce tract maps that estimate the probability of connection (or 'connectivity') of every voxel in the brain to a given seed point (Parker and Alexander, 2005).

For seed region placement, the b_0 images were normalised to a T_1-weighted template in MNI coordinates using the algorithm FLIRT (FMRIB's Linear Image Registration Tool, Jenkinson and Smith, 2001; Jenkinson et al., 2002), part of FSL. To improve the result of registration between images with different contrast, normalized mutual information was used as cost function. FLIRT has been extensively tested for registering to MNI standard brain images. The normalisation parameters were then applied to the fractional anisotropy maps. The seed regions were defined on the normalised fractional anisotropy maps. The spatial transformation was then reversed, and the seed regions were mapped to the original space of the DW-EPI images. The tracking algorithm was run in native space, and the output was transformed to normalised space. This procedure was chosen because the spatial transformation of non-scalar data (such as the tensor) is more complex than the transformation of scalar images (such as the seed point masks or the output probability images) (Alexander et al., 2001).

5.5.2 Results

5.5.2.1 Diffusion Maps

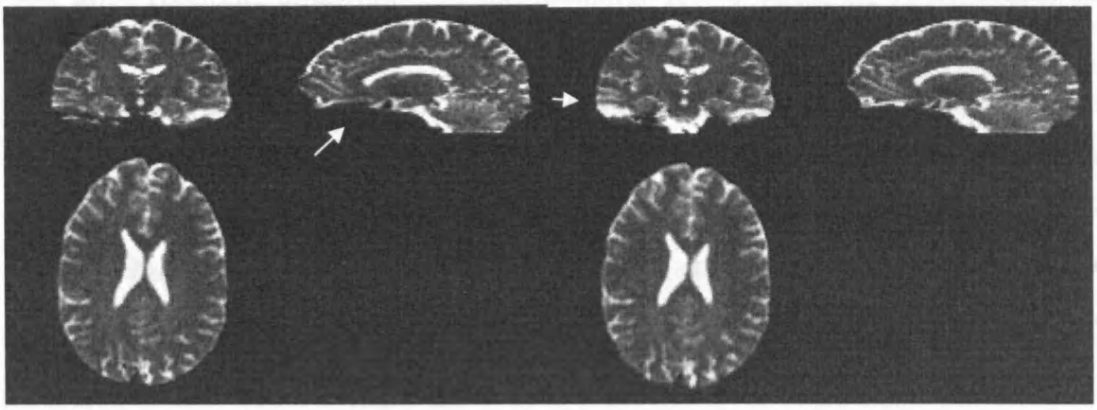

Fig 5.9. b_0 maps before (left) and after (right) correction for geometric distortions.

Although the amount of distortions is mild, some improvement in the overall brain shape can be observed after correction.

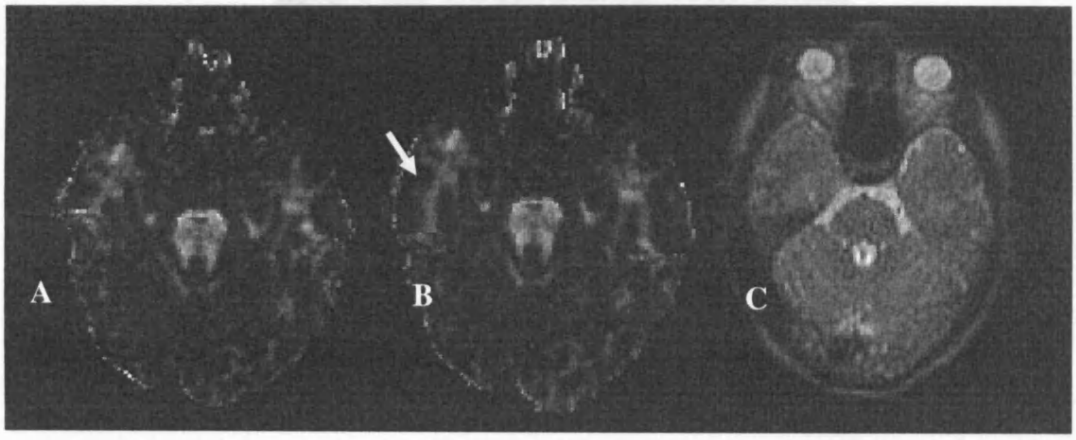

Fig 5.10. Fractional anisotropy maps obtained before (A) and after (B) correction for geometric distortions.

A T2-weighted anatomical image of the same slice is also shown for comparison purposes (C).

The geometric properties of the sample were improved by the correction, as expected from previous experiments. Fig 5.9 shows b_0 maps obtained before (top) and after (bottom) unwarping. In the temporal lobes, however, some artifactual results were observed on quantitative maps.

Fig 5.10 shows images of FA for the same slice location, obtained (A) before unwarping, and (B) after unwarping. A T_2-weighted anatomical image of the same slice is also shown for comparison purposes (C). The regions indicated by the arrows, characterised by relatively high anisotropy, are unlikely to correspond to real anatomical structures. More plausibly, the signal collapsed in a single voxel due to field inhomogeneity during the acquisition, was "smeared out" by unwarping.

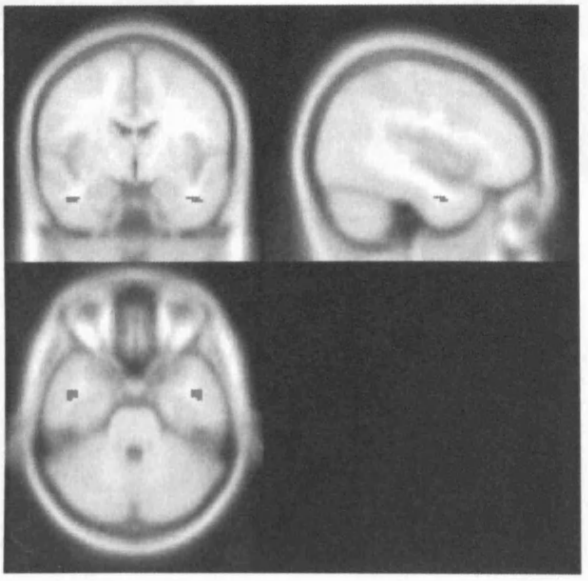

Fig 5.11. Position of the seed points in both hemispheres (in green).
The seed regions are overlaid onto a T1-weighed template.

5.5.2.2 Deterministic Tractography

Fig 5.11 shows the position of the seed regions in the temporal lobes, placed bilaterally in the inferior longitudinal fasciculus, in the location of the fusiform gyrus. A three-dimensional view of the tract generated from this seed point is shown in Fig 5.12. Most of the streamlines reconstructed by the tracking algorithm connect

the temporal lobe with the occipital lobe, consistent with the shape and the orientation of the inferior longitudinal fasciculus. However, some false positive are present. In particular, one of the streamlines originating from the temporal lobe is directed towards the cerebellum and might be the result of the artifact observed on the fractional anisotropy maps in Fig 5.10. There was no corresponding streamline on the contralateral side.

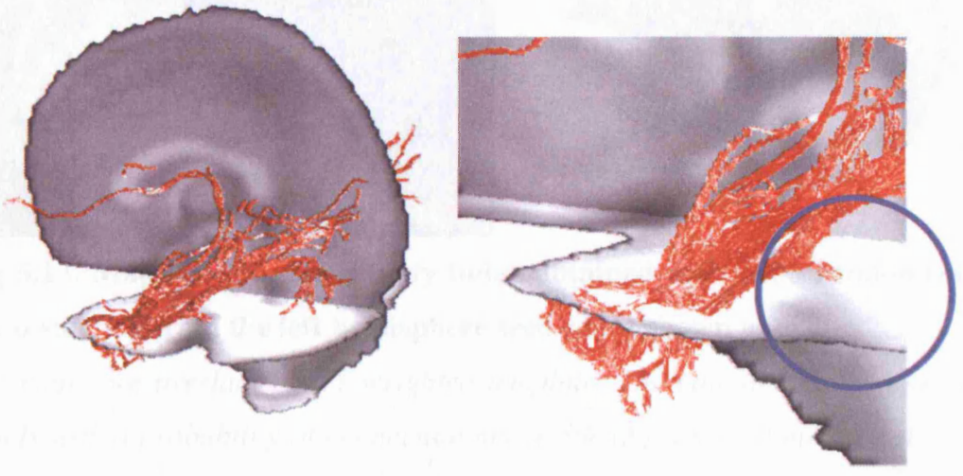

Fig 5.12. Reconstructed inferior longitudinal fasciculus.

Normal view (left) and enlarged view (right). The circle highlights the area of interest.

5.5.2.3 ProbabilisticTractography

PICo estimates the probability of connection between each voxel in a seed point region (shown in Fig 5.11) and the rest of the brain, thus producing a map of connectivity for every voxel in seed region. A convenient way of displaying a global map of the tract is by taking at each voxel the maximum probability value across the connectivity images obtained from each seed point. Fig 5.13A shows a map of the probability of connection for the left inferior longitudinal fasciculus overlaid onto a T_1-weighted template in MNI coordinates (only probabilities higher than 3% are displayed). A three-dimensional isosurface plot of the voxels with probability higher than 5% of connection to the seed point is also shown (Fig 5.13B). While the overall reconstruction is consistent with known shape and location of the inferior longitudinal fasciculus, the tract appears "stretched" on the axial section

corresponding to the area of the artefact. A pattern similar to that identified using deterministic tracking algorithm can be seen on Fig 5.13B.

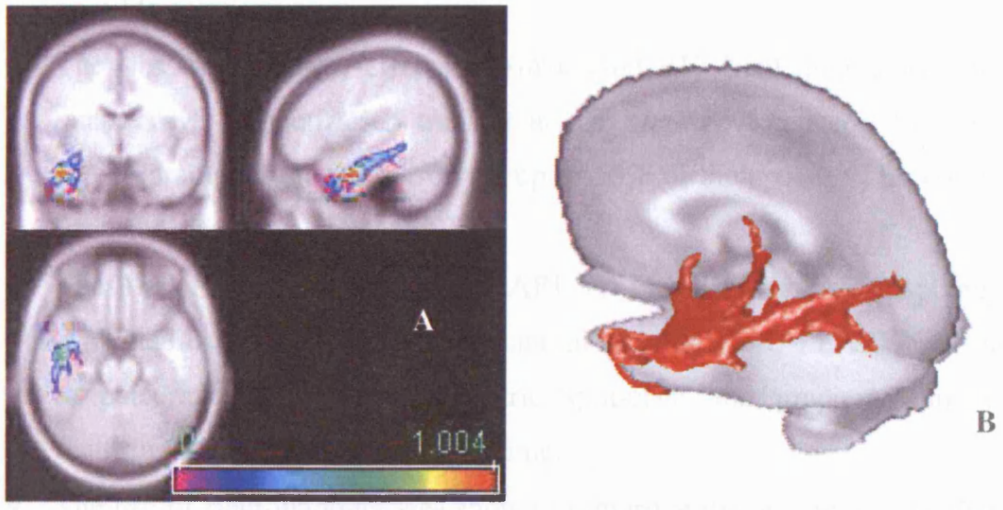

Fig 5.13. Maps of the connectivity index obtained with 1000 randomization of PICo starting from the left hemisphere seed-point shown above.

The maps are overlaid on T1-weighted template. The coloured area represents all voxels with a probability of connection above 3% (A). Three-dimensional isosurface plot of voxels with probability of connection > 5% to the seed-point (B).

5.5.3 Conclusions

I have shown that field-mapping correction can produce an artifactual result when applied to quantitative MR techniques such as DT-MRI. In particular, when the mapping between the original and the distorted space is 'many-to-one', intensity correction is not always able to retrieve the missing information.

Although in the present case I could not clearly demonstrate the failure of the tracking algorithm, part of the identified tract is unlikely to correspond to a real anatomical structure. The use of a simple field-map correction could have important consequences for fibre tracking applications of DT-MRI (depending on the original orientation of the eigenvectors). A more reliable correction could be obtained by collecting additional images reversing the polarity of the phase encoding gradient (Chang and Fitzpatrick, 1992; Andersson et al., 2003).

5.6 Summary

- The well-known effects of static field inhomogeneity on EPI, and their possible solutions were reviewed.
- The (less-well-known) effects of static (and RF) field inhomogeneities on quantitative magnetization transfer at 3 T were investigated. Some of the fitted parameters showed errors of up to 50% of their value if no correction for these effects was performed.
- The use of ultra-fast low angle RARE (U-FLARE) for field-mapping was evaluated using a chemical shift phantom and in-vivo. U-FLARE was shown to perform as well as asymmetric spin-echo and gradient-echo, while requiring a much shorter scanning time.
- The use of field-mapping was shown to improve the anatomical localization of functional MRI activations, due to the improved registration between EPI data and high-resolution anatomical data.
- The use of field-mapping for correcting diffusion data was less successful. In areas particularly sensitive to field inhomogeneities, where signal arising from different voxels collapses into a single one, regions of high anisotropy, unlikely to be anatomical, appeared after unwarping.
- These artefacts did not appear to change the results of tractography algorithms in this example. However, some non-anatomical connections between the temporal lobe and the cerebellum were found which might be the consequence of "tract stretching" due to field-map correction. In conclusion, alternative, more reliable, correction methods should be used when dealing with diffusion data.

Chapter 6

Analysis of Multivariate Data

Introduction

Different MRI parameters can provide information about different biological characteristics of a given tissue (e.g. Bernarding et al., 2000; Confort-Gouny et al., 1993), and, combined with clinical variables, improve detection and understanding of pathological conditions. The most informative way of combining these variables is not immediately obvious, but multivariate analysis provides a statistical tool able to reduce the dimensionality of data and to extract from those data some 'latent variables' that better represent the characteristics of the object under study. Several multivariate methods exist and in this chapter, I summarize some of the basic concepts of principal component analysis (PCA), and I show some preliminary results obtained on quantitative MT data. PCA was chosen because it does not only provide information on the pattern of association between variables, which can be achieved using other methods, such as cluster analysis, but it also yields a new set of variables, of reduced dimensionality, which can be analysed in place of the original set. For details on alternative multivariate methods, the reader is referred to Lattin et al. (2003) or similar specialized text books.

6.1 Overview of principal component analysis

Multivariate analysis is concerned with the study of association among sets of measurements. PCA can be used essentially for two purposes: to investigate any association existing among variables (exploratory analysis), and to reduce the dimensionality of data by reorienting them so that the first few dimensions account for as much of the available information as possible. The latter application can only be accomplished when the data under analysis are sufficiently correlated to justify the reduction.

6.1.1 Principal Component Analysis: the methods

PCA is a method for re-expressing multivariate data. The solution has the property that each component is uncorrelated with all others, and each component is an exact linear combination of the original variables. There is no *a priori* model of the data, nor of the parameters underlying them.

Given a vector matrix **X** (assumed to be standardized, i.e. each column is normalised to zero mean and unit standard deviation), whose columns represent the original *p* variables

$$\mathbf{X} = \left[\mathbf{x}_1, \mathbf{x}_2, ..., \mathbf{x}_p\right], \qquad [6.1]$$

the goal of PCA is to find a linear combination $\mathbf{u}=(u_1,u_2,\ldots u_p)'$ (where the symbol "'" represents the transpose matrix) that maximises the variance of the elements of **z**, defined as

$$\mathbf{z} = \mathbf{Xu}. \qquad [6.2]$$

The variance of **z** can be expressed as

$$\mathrm{var}(\mathbf{z}) = \frac{1}{(n-1)}\mathbf{u'X'Xu} = \mathbf{u'Ru} \qquad [6.3]$$

where **R** is the sample correlation matrix, and the equality is justified by the assumption that **X** is standardised. Equation [6.3] must be maximised under the constraint **u'u** = 1, to avoid driving var(**z**) to infinity by making **u** arbitrarily large.

The solution to the problem is found by setting to zero the derivative of the Lagrangian

$$L = \mathbf{u'Ru} - \lambda(\mathbf{uu'} - 1). \qquad [6.4]$$

In Eq [6.4], the first term on the right hand side represents the quantity to be maximised, while the second term accounts for the imposed constraint.

Taking the derivative of Eq [6.4] with respect to **u** and setting it to zero leads to the solution of the eigenvalue-eigenvector problem (where **I** is the identity matrix)

$$(\mathbf{R} - \lambda\mathbf{I})\mathbf{u} = 0, \qquad [6.5]$$

which is a set of *p* eigenvalues (λ_i) with an associated set of *p* eigenvectors ($\mathbf{u_i}$) satisfying Eq [6.5]. The matrix of principal components, **Z,** is given by the product of **X** and $\mathbf{U}=[\mathbf{u_1}, \mathbf{u_2}, .., \mathbf{u_p}]$:

$$\mathbf{Z} = \mathbf{XU}. \qquad [6.6]$$

The solution of an eigenvalue-eigenvector problem is also called *spectral decomposition* and is obtained by finding the roots of a polynomial equation.

From Eqs [6.3] and [6.5] it follows that

$$\mathrm{var}(\mathbf{z}) = \mathbf{u}'\mathbf{R}\mathbf{u} = \mathbf{u}'\lambda\mathbf{u} = \lambda\mathbf{u}'\mathbf{u} = \lambda, \qquad [6.7]$$

i.e. the eigenvalues of **R** are the variances associated with each principal component. As a consequence, from Eq [6.6] we can obtain the standardized matrix of principal components, $\mathbf{Z}_S$ as

$$\mathbf{Z}_s = \mathbf{XUD}^{-1/2}, \qquad [6.8]$$

where **D** is a diagonal matrix, whose elements are the eigenvalues λ_i. Rearranging Eq [6.8] and recalling that $\mathbf{u}_i$ are mutually orthogonal, we also obtain

$$\mathbf{X} = \mathbf{Z}_s\mathbf{D}^{1/2}\mathbf{U}'. \qquad [6.9]$$

Equation [6.9] states that the PCA of **X** can be done by singular value decomposition (SVD).

An additional useful quantity is the correlation matrix (**F**) of the principal component scores (**Z**) with the original data (**X**), which is referred to as the principal component loadings:

$$\mathbf{F} = \frac{1}{(n-1)}\mathbf{X}'\mathbf{Z}_s = \frac{1}{(n-1)}\mathbf{X}'\mathbf{XUD}^{-1/2} = (\mathbf{UDU}')\mathbf{UD}^{-1/2} = \mathbf{UD}^{1/2}, \qquad [6.10]$$

where Eq [6.8] and the property **UU'=I** (identity matrix) were used.

From the principal component loadings, we can determine the amount of variance accounted for in each original variable by any number of principal components.

The interpretation of each component is easier when the loadings take on values close to either zero or one. PCA has a unique solution determined by the rule that the first component must be the linear combination of the input variables with the greatest variance, while the second component must be the linear combination uncorrelated with the first with next greatest variance, and so on. This rule, however, is based on an arbitrary criterion, and therefore an equally valid, but easier to

interpret, solution can be found by rotating the components extracted by PCA. Discussing the many different ways of determining the rotation matrix which gives the most suitable solution is beyond the scope of this thesis (see Lattin et al., 2003 for review).

6.1.2 Criteria to determine the number of components to retain

There are a number of heuristic methods of establishing how many components should be retained. A simple criterion involves retaining a sufficient number of components to adequately reconstruct the original data set. In practice this is equivalent of imposing a threshold on the percentage variance in each original variable accounted for by the number of components retained. This can be calculated by reconstructing the original variables using a reduced number of components:

$$\mathbf{X} \approx [\mathbf{z}_{1s}, \mathbf{z}_{2s}, \ldots \mathbf{z}_{cs}]\mathbf{D}^{1/2}\mathbf{U}', \qquad [6.11]$$

where $c<p$.

In other cases, it is more important to consider the amount of variance across all variables, rather than in each of them individually. A helpful graphical approach is the *scree plot* (Cattel, 1966). This involves plotting the variance accounted for by each principal component in descending order. If the curve shows a bend after which the remaining eigenvalues decline in a linear fashion, it is sufficient to retain the components corresponding to the eigenvalues before the bending point only.

6.2 Application to MRI data

The variables of interest in MR data of the type described here are MRI parameters measured in a group of subjects. The parameters might be the calculated measure from different modalities (e.g. MTR, fractional anisotropy, T_1), or they can be the outcome measure of a multi-parametric technique, such as quantitative MT. It should be recalled that the use of PCA for reducing data dimensionality is only justified if the variables under analysis are highly enough correlated with each other. While this is almost certainly the case when dealing with quantities derived from the same MRI experiment, this hypothesis might be worth testing in other cases. However, in addition to reducing dimensionality, PCA is also useful for gaining insight into patterns of association between variables. This second property is

particularly interesting in the context of multi-parametric MRI, where it might help in relating a combination of MRI parameters with a given tissue characteristic. In addition, it could help elucidating the amount of overlapping information provided by two or more MRI parameters, measured to answer a specific clinical question. This could be very important to reduce scan times in clinical settings.

Another important consideration is how to draw the observations from the available images. The simpler approach is based on regions of interest (ROIs), i.e. involves obtaining the average parametric values for one or more given ROIs, and the extraction of the principal components. Given the nature of MRI data, however, a voxel-by-voxel analysis is more attractive. Image coregistration is of course a fundamental requirement in this context. While very sophisticated algorithms for the registration of images collected using spin-warp acquisitions are available, combining such images with EPI-based maps can be problematic. It was shown in the previous chapter that the use of field-map correction may fail, while the use of non-linear registration algorithms does not always produce ideal results.

Finally, it must also be considered that, since the aim of PCA is to reduce the dimensionality of the data by identifying latent variables that capture most of the variance, choices such as including or excluding CSF, or analyzing separately different tissues may give different results.

6.2.1 Implementation

An algorithm for PCA analysis of image data was implemented in Matlab (The Mathworks, MA, USA). The data matrix, **X**, has p columns, corresponding to the number of variables, i.e. to the number of MRI parameters entered. The number of lines of **X** is the number of observations, N. In this 'voxel-by-voxel' implementation, N is equal to the number of subjects times the number of *voxels of interest*, in the example below those from white and grey matter. The algorithm is designed to consider only voxels whose value is above zero, so that background voxels can be automatically identified and excluded from the analysis.

After standardizing every column of the Nxp matrix by subtracting the mean and dividing by the standard deviation, the covariance matrix, **R**, is calculated as

$$\mathbf{R} = \frac{1}{N-1}\mathbf{X}'\mathbf{X} \qquad [6.12]$$

Next, **R** undergoes spectral decomposition, producing **U** and **D**, as described in section 6.1. The component scores and the component loadings are calculated according to Eqs [6.6] and [6.10], respectively. This leads to p images of the principal components for each subject. The eigenvalues can be used to determine how many components should be retained, and the loadings can be used to investigate which parameters are weighted more in each component, and therefore speculate on the biological meaning of each component.

6.2.2 Example: quantitative MT imaging from a single subject

6.2.2.1 Input data

As an example application of the algorithm, I used the set of parameters obtained from quantitative MT from a single subject. This simplifies the analysis, as these images are inherently co-registered and therefore require minimum pre-processing.

The data were collected as part of the optimisation experiments described in Chapter 4, section 4.4. Briefly, images were obtained from a male healthy subject (35 years old), using a fast SPGR MT-weighted pulse sequence (TR/TE=28/5.1 ms, flip angle=5°, Gaussian MT pulses, duration=14.6 ms, 28 reconstructed slices), with 10 different MT-weightings, according to the optimised scheme 2 in Chapter 4. B_1 and T_1 mapping data were also acquired. The MT model in Eq [4.2] was fitted as described in section 4.2.2 to the data providing estimates of RM_0^A, $f/[(1-f)R_A]$, T_2^B, and $1/R_AT_2^A$, accounting for B_1 inhomogeneity based on the acquired map. Maps of the macromolecular fraction, f, liquid pool longitudinal (T_1^A) and transverse (T_2^A) relaxation times were obtained as described in Chapter 4. See Chapter 4 for more details on the acquisition and processing. Five variables were considered for PCA: f, RM_0^A, T_1^A, T_2^A, and T_2^B.

6.2.2.2 Image segmentation

The fast SPGR volume part of the T_1-mapping protocol (TR=13.1 ms, TE=4.2 ms, flip angle = 25°) was segmented into white matter, grey matter and CSF using SPM99 (www.fil.ion.ucl.ac.uk/spm/). White and grey matter segments were then combined to produce a brain mask using the routine *spm_xbrain*. Spm_xbrain uses iterative erosions and dilations to remove pixels outside the brain, and combines

grey and white matter. The brain mask was used to remove background and CSF pixels from all MT maps.

The brain-extracted maps were then processed using the algorithm described above, producing maps of the principal components, eigenvalues, and component loadings for the system.

6.2.2.3 Results

The eigenvalues of the system were, in descending order, diag(**D**) = [2.06, 1.06, 1.01, 0.58, 0.29]. Fig 6.1 shows the input parametric maps, and the five principal components.

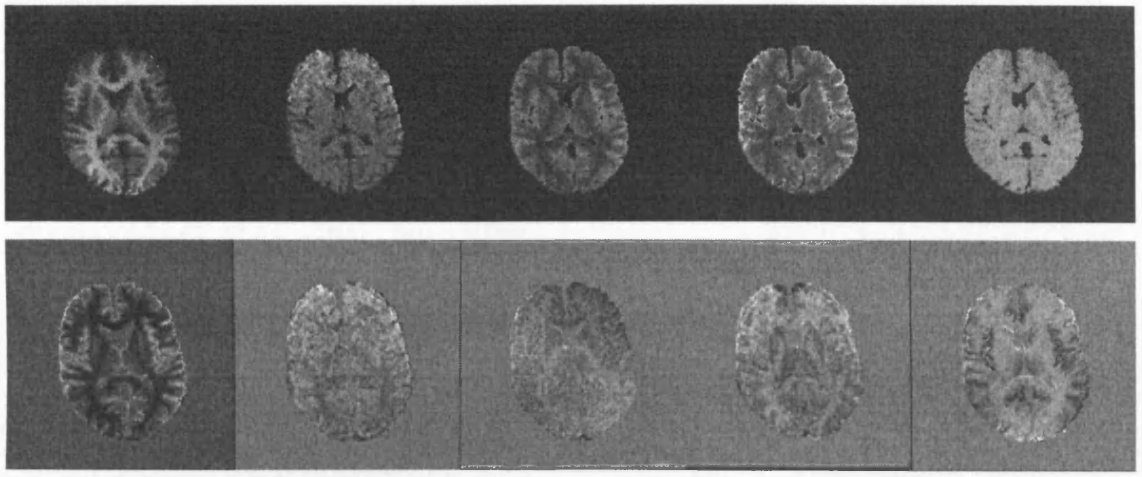

Fig 6.1. MT parametric maps (top) and principal component maps (bottom).

MT maps are, from left to right, f, RM_0^A, T_1^A, T_2^A, and T_2^B. The principal component maps are shown in descending order.

Fig 6.2 shows the scree plot for the MT data. From the plot it appears that the first three components should be retained. The variance accounted by the first three components is 83% of the total variance, obtained from

$$\mathrm{var}_{3PC} = \frac{\sum_{i=1}^{3} \lambda_i}{\sum_{i=1}^{5} \lambda_i} = 0.83. \qquad [6.13]$$

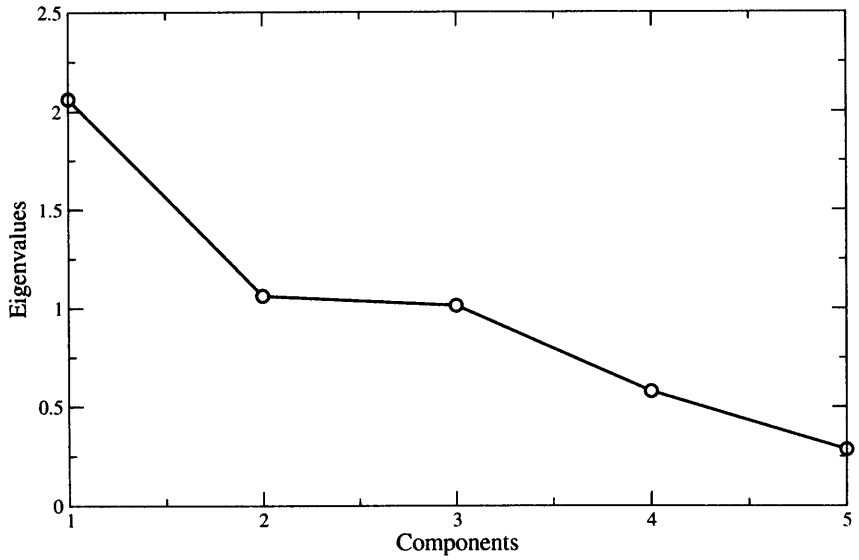

Fig 6.2. Scree plot for the MT data.

The loadings for the first three components are reported in Table 6.1, and summarized in the bar plot in Fig 6.3.

Table 6.1. Principal component loadings for the MT data.

	PC1	PC2	PC3
f	**-0.70**	**-0.53**	-0.07
RM_0^A	-0.34	**0.86**	0.09
T_1^A	**0.90**	0.08	-0.08
T_2^A	**0.79**	-0.17	0.17
T_2^B	-0.14	0.08	**0.98**

Only the loadings from the first 3 components are shown. The loadings larger than 0.5 (in absolute value) are highlighted in order to ease the interpretation.

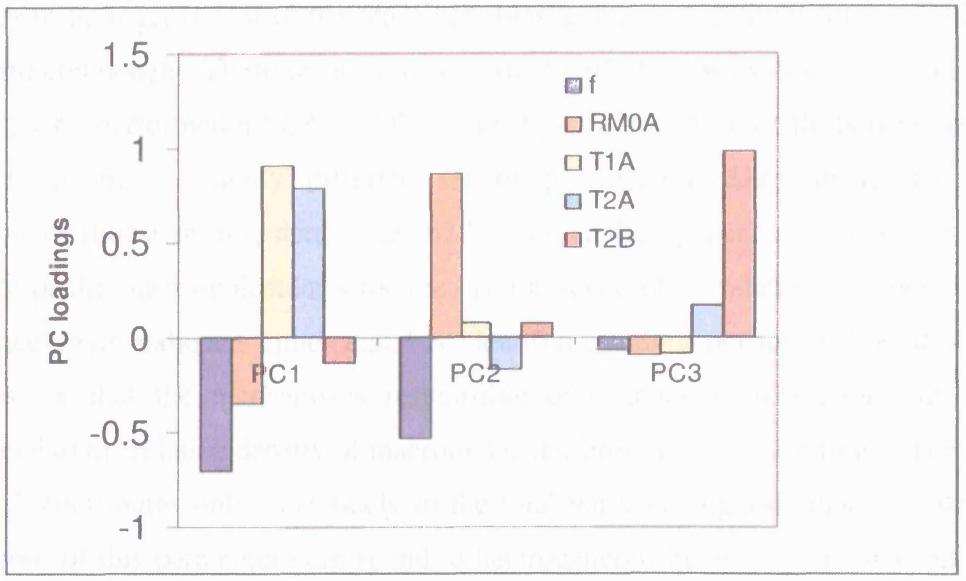

Fig 6.3. Principal component loadings.

Fig 6.3 suggests that the first component is highly correlated with T_1^A, T_2^A, and f; the second component is highly correlated with RM_0^A and f; the third component is highly correlated with T_2^B.

6.2.2.4 Interpretation and conclusions

The main results of this analysis are summarized in Table 6.1 and Fig 6.3. The principal component loadings suggest that T_1^A and T_2^A are highly correlated (and their variability can be captured by the same component). RM_0^A is mainly weighted in the second component, with f being correlated with both the first and the second components. T_1 is known to be affected by the presence of myelin in white matter (Koenig et al., 1990; Koenig, 1991), and f is believed to reflect the myelin content. Consequently, some (inverse) correlation between f and T_1 is to be expected and has been previously observed (see also Chapter 4). The first component thus could be reflecting myelination. It is also unsurprising that the first component, i.e. the one with the greatest variance across the images, reflects white-to-grey matter contrast. The second component, however, also has a high loading in f, thus suggesting that this parameter conveys more information than T_1 alone. The loadings of the second component also indicate a relationship between f and RM_0^A. Again, this can be understood by recalling that both these quantities (and therefore the second component) are related to the relative spin density of the two pools. Finally, T_2^B

appears to be independent of the other variables and almost entirely summarized by the third component. These results are consistent with the observations of Sled et al. (2004), who performed a PCA of MT parameters measured in 12 ROIs from seven subjects (using a slightly different set of parameters). They interpreted the component almost entirely determined by T_2^B ($T_{2,r}$ in their paper) as a measure of the rigidity of the macromolecular structure. The absence of correlation between f and T_2^B once again indicates either that f is identifying only a portion of bound water species, or that the mechanisms responsible of changes in relaxation time are unrelated to the relative density of macromolecular protons in a given tissue. The fact that T_2^B contributes only moderately to the total variance suggests that only subtle variations of this parameter correspond to heterogeneous healthy tissue. It would be interesting to repeat the analysis in the presence of pathology, to ascertain whether these results would change.

It must be noted, however, that PCA is not able to distinguish between the intrinsic variability of a parameter due to the underlying structure, and the variability dependent on measurement error and image inhomogeneity. Looking at Fig 6.1, for example, it seems evident than the second and the third components also reflect the low frequency variation due to field inhomogeneity in the input parametric maps. Although not part of this experiment, it would be interesting to investigate whether the rotation of the solution could lead to a set of components which clearly separates the variability originating from image artifacts from the variability reflecting genuine tissue structure characteristics.

The use of data from a single subject clearly limits the validity of these results; nevertheless, the experiments described in this chapter provide some basis for interpreting combinations of MT parameters of human brain tissue. They also show the applicability and the implementation of multivariate techniques to multi-parametric MRI.

6.3 Summary

- Principal component analysis (PCA) can be used to reorient the data so that the first few dimensions account for as much information as possible. It can

also be used to identify patterns of association between variables, and thus help the interpretation of the data.

- Multi-parametric MRI data are an ideal candidate for PCA as several MRI parameters are likely to be correlated, and the interpretation of their inter-dependence is not always straightforward. When combining parameters measured with different techniques (e.g. diffusion and MT data), registration issues must be carefully considered.
- An exploratory PCA carried out on five MT parameters measured in a single subject, showed a relationship between T_1^A, T_2^A, and f, as well as a relationship between RM_0^A and f. T_2^B appears not to be correlated with the other parameters.
- A limitation of this type of analysis is the inability to separate variance components genuinely related to the underlying tissue structure from those due to image artefacts. A rotated solution might help in removing this ambiguity.

Conclusions and Future Work

The experiments described in this thesis generated a number of results, as well as some ground for further investigations. Here the main findings are briefly summarized.

Magnetization Transfer Ratio

MTR has become a well-established MRI technique for tissue characterization, thanks to its sensitivity to the properties of macromolecules. Another reason for its success is that acquisition and image processing for this technique are not particularly demanding. A limitation is, however, the fact that the MTR values depend on a complicated combination of sequence and relaxation parameters. In Chapter 3, the interaction between T_1 and MT has been investigated, confirming that MTR acquisition protocols should be designed to minimize T_1-weighting. The experiments here described also suggest that the interaction between MT and T_1 relaxation may limit the sensitivity of MTR, thus prompting the introduction of alternative measurements which isolate MT effects from T_1 effects. Future work should concentrate in identifying quantities with these characteristics, whose measurement is feasible within the limitations of a clinical setting (both in terms of scan time and facilities required for their computation).

An alternative option is the use of quantitative model of MT to maximize the contrast between specific tissues and therefore improve the sensitivity of MTR to a given pathological change. Such an optimisation of MTR sequences is possible, and an example of such optimisation in terms of white-to-grey matter contrast-to-noise ratio was given in Chapter 3. The optimisation was carried out at both 1.5 T and 3.0 T, showing also that *in vivo* MTR acquisition at the higher field strength is safe and provides advantages in terms of both signal and contrast to noise ratio. This conclusion is important, as with the increasingly widespread use of 3.0 T clinical scanners, it is desirable to design a suitable protocol for MTR acquisition at high field. Future work will focus in validating these results.

Quantitative Magnetization Transfer

Quantitative measurement of MT model parameters is likely to become increasingly popular, thanks to its potentially increased specificity. The main factors limiting its spread to date have been the long scan times, which prevent its use for clinical applications, and the technical demands in terms of image processing. In general, quantitative MT models require the collection of a series of MT-weighted images and the estimation of a number of parameters by non-linear fitting. This has important consequences for its sensitivity to background noise. The work presented in Chapter 4 of this thesis was mainly focussed on improving the robustness of clinically feasible quantitative MT protocols. The use of a 3D acquisition sequence, the implementation of quantitative MT at higher field strength, and finally the investigation of optimal sampling strategies of quantitative MT showed that, while this technique is still in its infancy, dramatic improvements can be achieved. Future work should concentrate on selecting the most suitable MT model, among the ones available, and then optimising the acquisition for such a model. Optimisation techniques can also be used to derive the optimal number of measurements, compromising between scan time and quality of the calculated maps.

A fundamental aspect to be considered is the effect of B_1 and B_0 field inhomogeneity of quantitative MT. The simple experiment described in Chapter 5 demonstrates that this issue should not be overlooked, and quicker and more reliable methods of measuring the fields should be pursued.

An additional interesting area of investigation concerns the biological meaning of the MT parameters measured. The multivariate analysis described in Chapter 6 suggests that f, RM_0^A and T_2^B convey complementary information, which makes this technique even more interesting. Further work is warranted in this area, and correlations with post-mortem data might help in understanding the substrate of changes in these parameters.

B_0 Field Mapping

The main reasons for exploring B_0 mapping as part of this project were, on one hand, its importance for quantitative MT, on the other, its application to the correction of geometric distortions in EPI. This is a major issue in the context of multi-parametric MRI, where the achievement of a near perfect co-registration

between quantitative maps is necessary. The experiments described in Chapter 5 were focused on this subject. The use of novel acquisition sequences, such as U-FLARE, was investigated, giving promising results. The use of field-map based correction for fMRI data was shown to allow a better registration of EPI images with the standard space template, thus providing a better anatomic localisation of activations. This can be particularly important for functional mapping of cognitive tasks, typically located in smaller and less well-known structures.

The application of field-map correction to DT-MRI data was less successful. I have shown in Chapter 5 that its use can produce artifactual results when applied to DT-MRI. In particular, when the mapping between the original and the distorted space is 'many-to-one'-like, intensity correction is not able to retrieve the missing information. This result is disappointing, as the inability to spatially match EPI-based maps and spin-warp based maps constitutes a challenge for the researcher aiming at combining quantitative maps on a voxel-by-voxel basis. Alternative types of correction should be considered for these data, for example those based on the collection of additional images with the polarity of the phase encoding gradient reversed. It would also be interesting to investigate the effect such corrections have on the reproducibility of tractography, in areas where susceptibility is likely to have an effect.

Combining all the available information

The final goal of this project was identifying a way of combining different MRI parametric maps in order to provide information about different aspects of biology. This is clearly an ambitious aim, which was not fully achieved. Nevertheless, an attempt to combine different parameters through multivariate analysis was made, and the results of these efforts are summarized in Chapter 6. Principal component analysis was used to identify patterns of association between MT parameters, and the results, despite being drawn from a single subject, and therefore of limited value, appear promising. One of the problems identified with this type of analysis is the inability to distinguish between intrinsic variability of a parameter due to the underlying structure, and variability dependent on measurement error and image inhomogeneity. This observation has two main consequences. On one hand it supports the importance of improving image quality and field mapping

techniques, thus providing a binding element for the contents of this thesis. On the other, it suggests that further manipulation of the data by means of multivariate tools could help in removing this ambiguity. This subject (with many others) is confined to future work.

Appendix A

Functional MRI

Introduction

Functional MRI (fMRI) is a general term used to describe MRI-based techniques aiming to assess human brain function. The most common way of accessing this information is the use of blood-oxygenation level dependent (BOLD) contrast. Alternative approaches to fMRI are based on the measure of changes in the local cerebral blood flow, or volume (Kwong et al., 1992; Rosen et al., 1991). More recently, methods to detect the neuronal currents using the time-varying magnetic field that developes with their passage have been proposed (Bodurka and Bandettini, 2002). Here only the basic principles of BOLD fMRI will be briefly summarised.

A.1 Basic Principles

During neuronal activation, the energy required by the metabolic changes occurring at synaptic level is supplied in the form of adenosine tri-phosphate (ATP), which is formed via aerobic glycolysis, thus requiring oxygen and glucose to be supplied by blood. The BOLD effect is based on the different magnetic properties of oxygenated haemoglobin (oxyhaemoglobin) and haemoglobin with no oxygen attached to it (deoxyhaemoglobin). In particular, deoxyhaemoglobin is paramagnetic, while oxyhaemoglobin is not (Pauling and Coryell, 1936). Capillary and venous vessels containing deoxygenated blood thus cause a distortion of the magnetic field, and ultimately a change in the measured MRI signal.

A.1.1 The BOLD signal

In 1990 Ogawa et al. described the first BOLD contrast imaging experiment reporting a loss of signal around blood vessels in a rat that was made hypoxic (Ogawa et al., 1990). The authors interpreted these changes as a consequence of the magnetic properties of deoxyhaemoglobin. Similar experiments were carried out in other animals (Turner et al., 1991) and humans (Kwong et al., 1992) confirming the relationship between BOLD contrast and oxygenation.

The mechanisms underlying BOLD contrast are not fully understood, and the most common interpretation is the following: increased neuronal activity induces local vasodilation, and consequently increased cerebral blood flow and volume. Cerebral blood flow increases more than blood volume, and oxygen delivery quickly exceeds the local demand. The net effect is therefore a larger ratio of oxygenated to deoxygenated haemoglobin in the venous than in the arterial system, which leads to a longer regional T_2* compared to the surrounding tissue, thus causing an *increase* of MRI signal. The increase in blood flow is often attributed to energy consumption, although others (Attwell and Iadecola, 2002) have suggested an alternative explanation of the BOLD effect as a reflection of neuronal signaling.

A.1.1.1 The haemodynamic response

The BOLD response after a stimulus varies between subjects; although it has some common features. After an initial "dip", which is not always observed (Ernst and Hennig, 1994), there is progressive increase in the signal. The time to peak is of the order of seconds but it is variable and depends on several factors, including the characteristics of the stimulus and the anatomical region (Bandettini et al., 1997). After the end of the stimulus, the curve decreases in few seconds to a level below the initial baseline, from which it recovers slowly over further few seconds. Overall, the total duration of the response to an "impulse" stimulus is between 10 and 20 seconds, with consequences on the temporal resolution of fMRI. By modelling the vascular bed within a small volume as a balloon, i.e. as an expandable venous compartment fed by the output of the capillary bed, Buxton et al. (1998) proposed a physiological interpretation of the curve, suggesting that the transient features of the BOLD effect result from differences in the time courses of flow and volume changes.

A.1.2 fMRI Acquisition

A.1.2.1 Pulse sequence

In a typical fMRI experiment a large number of images are collected under varying stimulus conditions. In the simplest case, the same number of images is collected in two conditions, and voxel-by-voxel statistical analysis reveals the location of the brain response to the stimulus. This statistical approach is necessary due the small magnitude of the BOLD effect. As T_2* is more sensitive than T_2 to this effect, gradient echo acquisitions are more often used, although the use of spin-

echoes is also possible (see Kennan et al., 1994 for a theoretical description of T_2 and T_2* responses). Typically gradient-echo EPI (see Chapter 2) is used due to its speed (whole brain coverage in a couple of seconds) and its natural sensitivity to T_2*. The echo time must be chosen to match the T_2* of tissue to optimise the BOLD contrast. Typical TEs are of the order of 50 ms at 1.5 T and 30 ms at 3.0 T.

A.1.2.2 Experimental design

The type of experimental design varies with the aim of the study (Jezzard and Ramsey, 2003). The simplest experiment (*block design*) consists of alternating periods (epochs) of two experimental conditions. One of the two conditions typically represents the "baseline" condition, which can be rest, or, in other cases, a combination of functions present in the "on" condition, but not relevant to the brain function of interest and which therefore need to be controlled for. Block designs are very effective and robust, but have limited temporal resolution.

In a *parametric design*, the same task is repeated but with different levels of difficulty, which can be modelled using some parameter. This design is mainly used with cognitive tasks.

In an *event-related design*, the response to a single short stimulus or an event is recorded, thus allowing the BOLD response to be better characterised in terms of its temporal evolution.

A.2 Image analysis

Several statistical methods for the analysis of fMRI data have been proposed and no general agreement on the "gold standard" system exists. Several image analysis methods have been developed by different groups which are now regarded as standard fMRI analysis.

A.2.1 Spatial pre-processing

Any misalignment between scans due to motion must be corrected for, by means of image registration (Hajnal et al., 1994). The motion parameters determined during registration can also be recorded to be later used as regressors in the statistical analysis (Friston et al., 1996). This is advisable as in some cases involuntary motion might be correlated with the stimulus. After image registration, images are often spatially normalised to a template. This step is necessary in multi-subject studies, but

may also be useful in single-subject studies in order to better identify the anatomical location of the activation. Issues concerning the choice of the template might arise when the fMRI series is recorded using EPI. More details on geometric distortions and their consequences can be found in Chapter 5.

Often images are smoothed, in order to reduce high frequency noise, and to reduce inter-subject anatomical variability. The size of the smoothing kernel should be chosen to match the expected size of regions activated by the stimulus (Worsley et al., 1996).

A.2.2 Statistical analysis

The most commonly used analyses are based on multiple regression or equivalent methods (Friston et al., 1995) followed by some test of significance. Most image analysis programs utilize parametric tests, although non-parametric methods are also available (e.g. Bullmore et al., 1996). Here the basic principles of the statistical tool for fMRI used in Chapter 5 i.e. SPM will be described. Statistical Parametric Mapping, or SPM (www.fil.ion.ucl.ac.uk) is one of the most popular fMRI packages and was developed at the Wellcome Department of Imaging Neuroscience, London, UK.

In SPM, the general linear model is used to estimate a set of parameters that explain the MRI time series in each voxel of the brain. In matrix terms, the general linear model is written as

$$\mathbf{Y} = \mathbf{X}\boldsymbol{\beta} + \boldsymbol{\varepsilon}, \qquad [A.2]$$

where $\mathbf{Y}$ is the vector of data, $\mathbf{X}$ is the *design matrix*, i.e. a collection of factors (experimental conditions and confounding effects) which might explain the data, and $\boldsymbol{\varepsilon}$ is the error vector. The error terms are assumed to be independent and normally distributed (although more recent algorithms use restricted maximum likelihood estimates of the variance components to allow for non-sphericity). The vector $\boldsymbol{\beta}$ contains the unknown model parameters, which can be estimated by least squares.

Inferences about the parameter estimates can be made at every voxel using either F or T statistics by comparing the observed data with the null distribution. A correction for multiple comparisons is then required in order to reduce type I error due to the very large number of tests made (over all voxels in the brain). In SPM the

p values can be corrected using a method based on the Gaussian random field theory (Worsley et al., 1992), known as family-wise error (FWE) correction. An alternative type of correction, the false discovery rate (FDR) (Genovese et al., 2002), is also available; instead of controlling the chance of *any* false positives (as Bonferroni or random field methods do), this controls the expected *proportion* of false positives among suprathreshold voxels. A FDR threshold is determined from the observed p-value distribution, and hence is adaptive to the degree of signal in the data.

A.2.3 Between-subject analysis

When interested in combining data from a group of subjects, a random-effect analysis, or second-level analysis can be performed, after performing a fixed-effect or first level analysis on each subject. A first level design uses within-subject variance, thus providing results which cannot be generalised outside the sample. In order to make broader inferences or conclusions about the general population from which the subjects were drawn, the contrast images estimated from a fixed-effect analysis have to be entered into a design matrix at the second level analysis. The contrast images represent spatially distributed images of the weighted sum of the parameter estimates for a particular contrast, thus the image-to-image residual variability represents the between subject variance. This ensures that assumptions underlying the use of the Gaussian random fields theory (i.e. that the errors are independently distributed) are respected.

Appendix B

Diffusion Weighted MRI

Introduction

Diffusion-weighted (DW) MRI permits the measurement of water self-diffusivity and, as a consequence of the interactions between water molecules and obstacles that hinder their motion. DW MRI gives information about the size, orientation and shape of cellular tissue structures *in vivo*. The measurement of the water diffusion coefficient *in vivo* has proven useful in the study of normal and pathological brain, particularly after the introduction of diffusion tensor (DT) MRI (Basser et al., 1994). Several reviews (LeBihan et al., 2001; Schaefer, 2001; Bammer, 2003; Sundgren et al., 2004) have described in detail the clinical applications of DW and DT MRI.

B.1 Basic Principles

Diffusion phenomena are the consequences of a microscopic random motion, known as Brownian motion. As an effect of thermal agitation, every particle in a fluid is constantly moving and subject to random collisions with other particles. With every collision a particle changes direction randomly, so that, over time, its path can be described by a random walk. When there is a gradient in the concentration of a diffusing fluid (e.g. the mixing of two different liquids), diffusion results in a macroscopic flux of the fluid. When the concentration is stable, diffusion can only be described statistically, i.e. by measuring the probability that a molecule travels a given distance in a given time. This is the case for the motion of water molecules within water (water self-diffusion) in biological tissues. Water self-diffusion is the underlying principle of DW MRI.

B.1.1 Einstein Equation, free and restricted diffusion

In a homogeneous fluid at the equilibrium, no macroscopic flux can be observed and the mean net displacement remains zero. At microscopic level, in the simplest case of an isotropic medium, the probability that a certain molecule travels a

distance r during a time t has a Gaussian distribution with zero mean (as the probability of moving in one direction or the opposite is the same) and variance described by Einstein's equation:

$$\langle r^2 \rangle = 2NDt, \qquad [B.1]$$

where N represents the number of spatial dimensions over which diffusion distances are measured (typically 3).

This relationship states that the root mean squared displacement distance from the origin ($\sqrt{\langle r^2 \rangle}$) is proportional to the square root of time through the diffusion coefficient D. D characterises the mobility of molecules in a given fluid at a given temperature.

Two extreme cases can be imagined: in a simple bulk fluid with no limiting boundaries molecules are free to diffuse in any direction, with the diffusion distances increasing indefinitely in proportion to the square root of time (free diffusion). If molecules are confined to a finite region of space by impermeable barriers, however, they are reflected back when they collide with these barriers and in this situation, the diffusion distance increases linearly with the square root of time only for short diffusion times. As time increases, more and more molecules reach the barriers and the diffusion distance would eventually saturate reaching a plateau and the diffusion coefficient would drop. This process is called restricted diffusion.

In biological tissues, membranes and organelles form the partially permeable barriers which hinder diffusion, thus leading to an intermediate situation. The complex interaction with tissue microstructure causes the diffusion coefficient measured in biological tissues to be always lower than that of free water.

B.1.2 Diffusion and MRI

In the presence of a magnetic field gradient, spins undergoing a random diffusional motion accumulate different phase shifts. This results in a loss of phase coherence and therefore in attenuation of the MR signal. The amount of diffusion attenuation depends on two factors: the diffusion properties of the sample in the direction of the applied gradient, and the strength and duration of the magnetic field gradients present during the measurement. In practice these effects are extremely small, and very difficult to measure. However, sensitivity to motion can be increased

by adding strong magnetic field gradients to a pulse sequence. The so-called pulsed field gradient (PFG) method was introduced by Stejskal and Tanner in 1965 and it is still widely used as a way to increase the diffusion weighting of a pulse sequence.

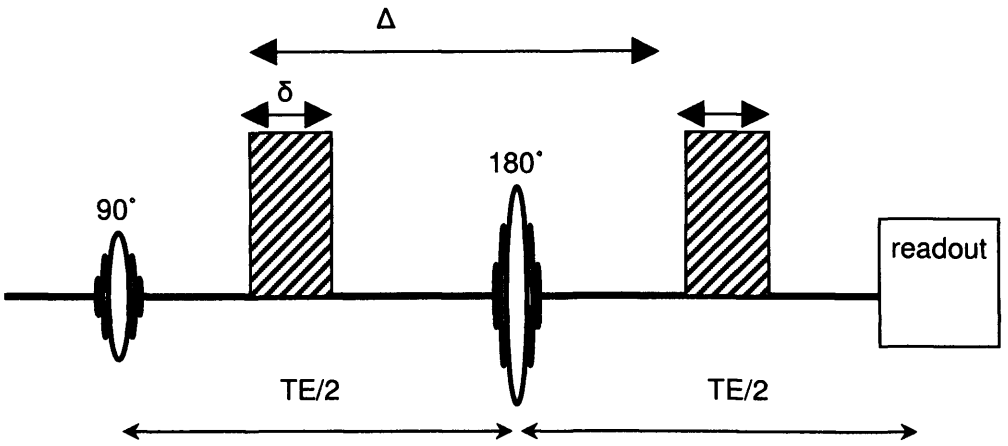

Fig B.1. A schematic representation of the Stejskal-Tanner (1965) pulsed-field gradient sequence.

The basic idea behind PFG is the introduction of a pulsed gradient on either side of the 180° refocusing pulse of a spin echo (See Fig B.1). During the application of the first gradient, spins sitting at different positions in the magnet bore experience different magnetic fields (due to the presence of the gradient) and accumulate different phase shifts. The 180° pulse reverses the phase of the spins, while the second gradient pulse causes a phase accumulation equivalent to the first one. If the spins remained stationary, these two phase shifts would cancel each other out. However, since the spins are moving randomly due to diffusion, they do not experience the same gradient field during the two pulses, and, at the echo time, the phase shifts will be randomly distributed, resulting in an imperfect refocusing of the spin echo and hence signal attenuation.

The Bloch equations were extended to include the diffusion mechanism by Torrey (1956) by introducing a diffusion term to the description of the transverse magnetization (M_{xy}) (Bloch-Torrey equation):

$$\frac{\partial M_{xy}}{\partial t} = -i\omega_0 M_{xy} - \frac{M_{xy}}{T_2} - i\gamma(\vec{G}\cdot\vec{r})M_{xy} + D\nabla^2 M_{xy} \qquad [B.2]$$

In Eq [B.2] ω_0 represents the Larmor frequency (see Chapter 1), T_2 is the transverse relaxation time, γ is the gyromagnetic ratio, and $(\vec{G}\cdot\vec{r})$ represents the dot product of the field gradient G and the spin position r.

Eq [B.2] can be solved with respect to M_{xy} (Stejskal and Tanner, 1965; LeBihan, 1995) giving

$$M_{xy} = M_0 e^{-bD} e^{-ir\cdot k} e^{-i\omega_0 t} e^{-t/T_2}, \qquad [B.3]$$

where M_0 represents the equilibrium magnetization, and the b-factor is defined as

$$b(t) = \int_0^t k(t')^2 dt', \qquad [B.4]$$

with

$$k(t) = \int_0^t G(t')dt'. \qquad [B.5]$$

In the rotating frame, if the applied gradients are balanced, the signal (S) measured at the echo time (TE) will be

$$S(b,TE) = S(0,0)e^{-bD} e^{-TE/T_2}. \qquad [B.6]$$

B.1.3 Measuring diffusion properties

From Eq [B.6], it is clear that a minimum of two acquisitions with different b factors (b_1, b_2) are needed in order to measure D. In this simple case (2 acquisitions) D is given by

$$D = \frac{1}{(b_1 - b_2)} \ln\left[\frac{S(TE,b_2)}{S(TE,b_1)}\right] \qquad [B.7]$$

The lowest b value is often approximately zero (i.e. no extra gradients applied, with the exception of the imaging ones), and it is often referred to as b_0.

In order to achieve significant, measurable, signal attenuation, on clinical MR scanners, either the pulses must be strong (placing strong demands on the gradient hardware) or the gradient must be applied for a long time (leading to extended echo times and poor SNR in the resulting images).

B.2 Diffusion anisotropy

B.2.1 The diffusion tensor

The PFG method introduces diffusion weighting along the specific direction along which the gradients are applied. In many biological tissues, particularly those

with a regular, ordered microstructure, the diffusion coefficient may vary with direction of measurement. With diffusion weighting applied in a single direction, this diffusion anisotropy may lead to difficulties when trying to interpret DW images, with hyperintensities indicating either focal abnormalities or the particular alignment of tissue structures. Although the exact mechanism of diffusion anisotropy is not fully understood, it is known that anisotropy reflects the presence of spatially oriented structures in the tissue. Assuming that the probability of molecular displacement follows a multivariate Gaussian distribution over the observed diffusion time, the diffusion process can be characterised by a 3x3 tensor matrix, **D** (Basser et al., 1994):

$$\mathbf{D} = \begin{bmatrix} D_{xx} & D_{xy} & D_{xz} \\ D_{yx} & D_{yy} & D_{yz} \\ D_{zx} & D_{zy} & D_{zz} \end{bmatrix}. \qquad [B.8]$$

Measuring the diffusion tensor must account for the interactions between imaging and diffusion gradients applied in all directions. Since **D** is symmetric, the measured signal is given by

$$S(TE,\mathbf{b}) = S(0,0)\exp\{-\mathbf{b}:\mathbf{D}\} = S(0,0)\exp\{-b_{xx}D_{xx} - b_{yy}D_{yy} - b_{zz}D_{zz} - 2b_{xy}D_{xy} - 2b_{xz}D_{xz} - 2b_{yz}D_{yz}\} \qquad [B.9]$$

where the symbol : indicates the general tensor product.

In Eq [B.9], **b** is a 3x3 matrix defined by

$$b_{ij} = \gamma^2 \int_0^{TE} k_i(t)k_j(t)dt, \qquad [B.10]$$

and k_i, k_j, represent any two components of **k**(t), the k-space trajectory vector, with $i, j \in [x, y, z]$.

The elements of the tensor matrix are different for each system of coordinates; however, it is always possible to find a frame where **D** is a diagonal matrix, with on-diagonal elements corresponding to the eigenvalues of the diffusion tensor, λ_1, λ_2, and λ_3, which are the diffusion values along the "principal axes".

Since the diffusion tensor is symmetric and positive definite, its eigenvectors ($\mathbf{e}_1$,$\mathbf{e}_2$,$\mathbf{e}_3$) are orthogonal and the matrix formed by them, $\mathbf{E}=[\mathbf{e}_1|\mathbf{e}_2|\mathbf{e}_3]$, is such that $\mathbf{E}'=\mathbf{E}^{-1}$, where the apostrophe indicates the transpose. The tensor can be diagonalised by

$$\mathbf{\Lambda} = \mathbf{E}'\mathbf{D}\mathbf{E}. \qquad [B.11]$$

B.2.2 Scalar Invariants of the tensor

For each diffusion tensor the combination of eigenvalues and eigenvectors is unique and reflects the microscopic diffusion properties of the sample. The eigenvector associated with the maximum eigenvalue represents the principal direction of diffusion. All the quantities obtained by combining the eigenvalues are rotationally invariant, i.e. their values do not depend on the way the tensor is measured. Several parameters have been proposed to represent the most characteristic properties of the tensor. The most commonly used, however, reflect either the magnitude of diffusivity, or the amount of anisotropy.

The simplest way of measuring the magnitude of diffusion is the trace of the tensor matrix:

$$tr(\mathbf{D}) = \lambda_1 + \lambda_2 + \lambda_3 \qquad [B.12]$$

Commonly, one third of the trace is reported, which is equivalent to the average of the eigenvalues, normally referred to as the mean diffusivity (MD):

$$MD = \frac{\lambda_1 + \lambda_2 + \lambda_3}{3} = \frac{tr(\mathbf{D})}{3} \qquad [B.13]$$

Several anisotropy indices have been proposed, with particular attention to their sensitivity to noise. The most commonly used is fractional anisotropy, or FA (Pierpaoli and Basser, 1996):

$$FA = \frac{\sqrt{(\lambda_1 - \langle \mathbf{D} \rangle)^2 + (\lambda_2 - \langle \mathbf{D} \rangle)^2 + (\lambda_3 - \langle \mathbf{D} \rangle)^2}}{\sqrt{\lambda_1^{\,2} + \lambda_2^{\,2} + \lambda_3^{\,2}}} \qquad [B.14].$$

Other indices often used are the relative anisotropy (Pierpaoli and Basser, 1996) and the lattice index (Pierpaoli and Basser, 1996).

B.2.3 Estimation of the diffusion tensor

In the absence of noise, the six independent elements of **D** and the amplitude of the unweighted signal could be derived by simply inverting the matrix obtained by performing one measurement without diffusion weighting and six measurements with the diffusion gradients lying in six non collinear directions. However, since data are contaminated by noise, a larger number of measurements are needed in order to estimate **D** reliably. The components of **D** can be assessed for every voxel either by a

non-linear fitting of the measured signal intensities, or, alternatively, by multivariate linear regression, as suggested by Basser et al. (1994).

B.3 Further developments

B.3.1 Tractography

The ability of DT-MRI to reflect the underlying tissue structures leads to the possibility of tracing fibre tracts in white matter. Various algorithms have been developed (Mori et al., 1999; Conturo et al., 1999; Parker et al., 2002; Parker et al., 2003; Berhens et al., 2003). There are two main types of algorithms: deterministic and probabilistic. The basic assumption at the basis of the deterministic algorithms is that the principal eigenvector is parallel to the main direction of fibres in every voxel, and therefore this type of algorithm produces a single trajectory. The main shortcomings of such an approach are the inability to account for fibre branching, and to assess the level of confidence that can be assigned to a reconstructed trajectory (Jones and Pierpaoli, 2005). The probabilistic approach (e.g. Parker et al., 2003; Berhens et al., 2003) aims to address these issues by considering multiple pathways emanating from a single seed-point, and assigning a probability of connection to the seed-point to every voxel in the brain.

B.3.2 Higher order models

While characterizing diffusion using a tensor allows anisotropy and directionality of diffusion to be accounted for at the voxel level, this model is unable to resolve complex intra-voxel structures such as crossing or branching fibres. More complex models have been proposed to resolve this issue. One simple alternative considers the superposition of more than one tensor (Tuch et al., 2002). More information about multiple components can be extracted by looking at the apparent diffusion profile, typically modeled by a set of spherical harmonics (Frank, 2002; Alexander et al., 2002). Finally, some researchers have developed methods based on *q-space* to measure molecular displacements directly. This method requires very high gradient strengths (to satisfy the underlying hypothesis of infinitesimally short gradient duration), and therefore it might not be feasible to implement it on commercial scanners. Intermediate models, which rely on data acquired on clinical

scanners, such as diffusion spectrum imaging (Wedeen et al., 2000) have also been proposed.

List of References

Aboitiz F, Scheibel AB, Fisher RS, Zaidel E. Fiber composition of the human corpus callosum. *Brain Res* 1992; 598: 143-53.

Alexander DC, Pierpaoli C, Basser PJ, Gee JC. Spatial transformations of diffusion tensor magnetic resonance images. *IEEE Trans Med Imaging* 2001; 20: 1131-9.

Alexander DC, Barker GJ, Arridge SR. Detection and modeling of non-Gaussian apparent diffusion coefficient profiles in human brain data. *Magn Reson Med* 2002: 48: 331-40.

Alexander DC, Barker GJ. Optimal imaging parameters for fiber-orientation estimation in diffusion MRI. *NeuroImage* 2005;27:357-67.

Andersson JL, Skare S, Ashburner J. How to correct susceptibility distortions in spin-echo echo-planar images: application to diffusion tensor imaging. *NeuroImage* 2003; 20: 870-88.

Attwell D, Iadecola C. The neuronal basis of functional brain imaging signals. *Trends Neurosci.* 2002; 25: 621-5.

Bagary MS, Symms MR, Barker GJ, Mutsatsa SH, Joyce EM, Ron MA. Gray and white matter brain abnormalities in first-episode schizophrenia inferred from Magnetization transfer imaging. *Arch Gen Psychiatry* 2003; 60, 779-788.

Bammer R. Basic principles of diffusion-weighted imaging. *Eur J Radiol* 2003; 45: 169-84.

Bandettini PA, Kwong KK, Davis TL, Tootell RB, Wong EC, Fox PT, Belliveau JW, Weisskoff RM, Rosen BR. Characterization of cerebral blood oxygenation and flow changes during prolonged brain activation. *Hum Brain Mapp* 1997; 5: 93-109.

Barker GJ, Simmons A, Arridge SR, Tofts PS. A simple method for investigating the effects of non-uniformity of radiofrequency transmission and radiofrequency reception in MRI, *Br J Radiol* 1998; 71: 59–67.

Basser PJ, Mattiello J, LeBihan D. MR diffusion tensor spectroscopy and imaging. *Biophys J* 1994; 66: 259-67.

Behrens TE, Woolrich MW, Jenkinson M, Johansen-Berg H, Nunes RG, Clare S, Matthews PM, Brady JM, Smith SM. Characterization and propagation of uncertainty in diffusion-weighted MR imaging. *Magn Reson Med* 2003; 50:1077-88.

Bernarding J, Braun J, Hohmann J, Mansmann U, Hoehn-Berlage M, Stapf C, Wolf K, Tolxdorff T. Histogram-based characterisation of healthy and ischemic brain tissue using multiparametric MR imaging including apparent diffusion coefficient maps and relaxometry. *Magn Reson Med* 2000; 43: 52-61.

Berry I, Barker GJ, Barkhof F, Campi A, Dousset V, Franconi JM, Gass A, Schreiber W, Miller DH, Tofts PS. A multicenter measurement of magnetization transfer ratio in normal white matter. *J Magn Reson Imaging* 1999; 9:441-6.

Bevington PR, Robinson DK. Chapter 3. *Data reduction and error analysis for the physical sciences*, 2nd edition. New York, McGraw Hill, 1969.

Bloch F, Hansen WW, Packard M. The nuclear induction experiment. *Phys Rev* 1946; 70:474-485.

Bodurka J, Bandettini PA. Toward direct mapping of neuronal activity: MRI detection of ultraweak, transient magnetic field changes. *Magn Reson Med* 2002; 47: 1052-8.

Boulby PA, Symms MR, Barker GJ. A simple method for matching distortions in functional and structural data. In: *Proceedings of the 12th Scientific meeting and exhibition of ISMRM,* 2004, Kyoto, Japan, p. 2196.

Boxerman JL, Hamberg LM, Rosen BR, Weisskoff RM. MR contrast due to intravascular magnetic susceptibility perturbations. *Magn Reson Med* 1995; 34:555-66.

Brihuega-Moreno O, Heese FP, Hall, LD. Optimization of diffusion measurements using Cramer-Rao lower bound theory and its application to articular cartilage. *Magn Reson Med* 2003; 50: 1069-76

Bruno SD, Barker GJ, Cercignani M, Symms MR, Ron MA. A study of bipolar disorder using Magnetization transfer imaging and voxel based morphometry. *Brain* 2004;127, 2433-2440.

Bullmore E, Brammer M, Williams SC, Rabe-Hesketh S, Janot N, David A, Mellers J, Howard R, Sham P. Statistical methods of estimation and inference for functional MR image analysis. *Magn Reson Med* 1996; 35: 261-77.

Buxton RB, Wong EC, Frank LR. Dynamics of blood flow and oxygenation changes during brain activation: the balloon model. *Magn Reson Med* 1998; 39: 855-64.

Cattel RB. The Scree test for the number of factors. *Multivariate Behavioral Research* 1966; 1: 245-276.

Ceckler TL, Balaban RS. HOT studies of water-macromolecular proton cross relaxation. In: *Proceedings of the 9th Annual Meeting of SMRM*, 1990, New York, USA; p. 354.

Chang H, Fitzpatrick JM. A technique for accurate magnetic resonance imaging in the presence of field inhomogeneity. *IEEE Trans Med Imaging* 1992; 11: 319-29

Chen NK, Wyrwicz AM. Correction for EPI distortions using multi-echo gradient-echo imaging. *Magn Reson Med* 1999; 41: 1206-1213.

Chiou JY, Nalcioglu O. A simple method to correct off-resonance related distortion in echo planar imaging. In: *Proceedings of the 8th Scientific meeting and exhibition of ISMRM*, 2000, Denver, Colorado, USA, p.1711.

Clare S, Jezzard P. Rapid T1 mapping using multislice echo planar imaging. *Magn Reson Med* 2001; 45, 630-634.

Confort-Gouny S, Vion-Dury J, Nicoli F, Dano P, Donnet A, Grazziani N, Gastaut JL, Grisoli F, Cozzone PJ. A multiparametric data analysis showing the potential of localized proton MR spectroscopy of the brain in the metabolic characterization of beurological diseases. *J Neurol Sci* 1993; 118: 123-133.

Conturo TE, Lori NF, Cull TS, Akbudak E, Snyder AZ, Shimony JS, McKinstry RC, Burton H, Raichle ME. Tracking neuronal fiber pathways in the living human brain. *Proc Natl Acad Sci U S A* 1999; 96: 10422-7.

Cook PA, Bai Y, Nedjati-Gilani S, Seunarine KK, Hall MG, Parker GJ, Alexander DC. Camino: Open-Source Diffusion-MRI Reconstruction and Processing. In: *Proceedings of the 14th Scientific Meeting and Exhibition of ISMRM*, 2006, Seattle, Washington, USA, p. 2759.

Cordes D, Arfanakis K, Haughton V, Meyerand ME. Geometrical distortion correction in EPI using two images with orthogonal phase-encodings. In: *Proceedings of the 8th Scientific meeting and exhibition of ISMRM*, 2000, Denver, Colorado, USA, p. 1712.

Crawley AP, Henkelman RM. A comparison of one-shot and recovery methods in T1 imaging. *Magn Reson Med* 1988; 7:23-34.

Crawley AP, Wood ML, Henkelman RM. Elimination of transverse coherences in FLASH MRI. *Magn Reson Med* 1988; 8: 248-260.

Cusack R, Papadakis N. New robust 3-D phase unwrapping algorithms: application to magnetic field mapping and undistorting echo-planar images. *NeuroImage* 2002;16:754-64.

Cusack R, Brett M, Osswald K. An evaluation of the use of magnetic field maps to undistort echo-planar images. *NeuroImage* 2003; 18: 127-42.

Davies GR, Tozer DJ, Cercignani M, Ramani A, Dalton CM, Thompson AJ, Barker GJ, Tofts PS, Miller DH. Estimation of the macromolecular proton fraction and bound pool T2 in multiple sclerosis. *Mult Scler* 2004; 10:607-13.

Dixon WT, Engels H, Castillo M, Sardashti M. Incidental magnetization transfer contrast in standard multislice imaging. *Magn Reson Imaging* 1990; 8:417-22.

Dousset V, Grossman RI, Ramer KN, Schnall MD, Young LH, Gonzalez-Scarano F, Lavi E, Cohen JA. Experimental allergic encephalomyelitis and multiple sclerosis:

lesion characterization with magnetization transfer imaging. *Radiology* 1992; 182:483-91.

Doyle M, Chapman B, Turner R, Ordidge RJ, Cawley M, Coxon R, Glover P, Coupland RE, Morris GK, Worthington BS, et al. Real-time cardiac imaging of adults at video frame rates by magnetic resonance imaging. Lancet. 1986; 2:682.

Dreher W, Leibfritz D. Fast proton spectroscopic imaging with high signal-to-noise ratio: spectroscopic RARE. *Magn Reson Med* 2002; 47: 523-8.

Duvvuri U, Roberts DA, Leigh JS, Bolinger L. Magnetization transfer imaging of the brain: a quantitative comparison of results obtained at 1.5 T and 4.0 T, *J Magn Reson Imaging* 1999; 10, 527-532.

Edelstein WA, Hutchinson JMS, Johnson G, Redpath T. Spin warp NMR imaging and applications to humal whole-body imaging. *Phys Med Biol* 1980; 25:751-756.

Edzes HT, Samulski ET. Cross-relaxation and spin-diffusion in proton NMR of hydrated collagen. *Nature* 1977; 265:521-523.

Efron B. Bootstrap methods: another look at the jackknife. *Annals of Statistics* 1979;7;1-16.

Ernst RR, Anderson WA. Application of Fourier transform spectroscopy to magnetic resonance. *Rev Sci Instrum* 1966; 37: 93-102.

Ernst T, Hennig J. Observation of a fast response in functional MR. *Magn Reson Med* 1994; 32: 146-49.

Filippi M, Rocca MA, Martino G, Horsfield MA, Comi G. Magnetization transfer changes in the normal appearing white matter precede the appearance of enhancing lesions in patients with multiple sclerosis. *Ann Neurol* 1998; 43, 809-814.

Finelli DA, Reed DR. Flip angle dependence of experimentally determined T_{1SAT} and apparent Magnetization transfer rate constants. *J Magn Reson Imaging* 1998; 8, 548-553.

Firbank MJ, Coulthard A, Harrison RM, Williams ED. A comparison of two methods for measuring the signal to noise ratio on MR images. *Phys Med Biol* 1999; 44:N261-4.

Foong J, Symms MR, Barker GJ, Maier M, Woermann FG, Ron MA. Neuropathological abnormalities in schizophrenia: evidence from Magnetization transfer imaging. *Brain* 2001; 124, 882-892.

Frank LM. Characterization of anisotropy in high angular resolution diffusion-weighted MRI. *Magn Reson Med* 2002; 47: 1083-99.

Friston KJ, Holmes AP, Worsley KJ, Poline JP, Frith CD, Frackowiak RSJ, Statistical parametric maps in functional imaging: a general linear approach. *Hum Brain Mapp* 1995; 2: 189–210.

Friston KJ, Williams S, Howard R, Frackowiak RS, Turner R. Movement-related effects in fMRI time-series. *Magn Reson Med* 1996; 35: 346-55.

Gadian DG. *Nuclear magnetic resonance and its applications to living systems.* 2nd ed., Oxford University Press, Oxford, 1995.

Genovese CR, Lazar NA, Nichols T. Thresholding of statistical maps in functional neuroimaging using the false discovery rate. *NeuroImage* 2002; 15: 870-8.

Glover GH, Schneider E. Three-point Dixon technique for true water/fat decomposition with B0 inhomogeneity correction. *Magn Reson Med* 1991; 18:371-83.

Grad J, Bryant RJ. Nuclear magnetic cross-relaxation spectroscopy. *J Magn Reson* 1990; 90: 1-8.

Graham SJ, Henkelman RM. Understanding pulsed Magnetization transfer. *J Magn Reson Imaging* 1997; 7, 903-912.

Graham SJ, Henkelman RM. Pulsed Magnetization transfer imaging: evaluation of the technique. *Radiology* 1999; 212, 903-910.

Gruetter R, Tkac I. Field mapping without reference scan using asymmetric echo-planar techniques. *Magn Reson Med* 2000; 43: 319-23.

Haacke EM, Brown RW, Thomson MR, Venkatesan R. *Magnetic Resonance Imaging: physical principles and sequence design.* Wiley, New York, 1999.

Haase A, Frahm J, Matthaei D, Hänicke W, Merboldt K-D. FLASH imaging: rapid NMR imaging using low flip angle pulses. *J Magn Reson* 1986; 67:258-266.

Hahn EL. Spin echoes. *Phys Rev* 1950; 80:580-594.

Hajnal JV, Baudouin CJ, Oatridge A, Young IR, Bydder GM. Design and implementation of magnetization transfer pulse sequences for clinical use. *J Comput Assist Tomogr* 1992; 16:7-18.

Hajnal JV, Myers R, Oatridge A, Schwieso JE, Young IR, Bydder GM. Artifacts due to stimulus correlated motion in functional imaging of the brain. *Magn Reson Med* 1994; 31: 283-91.

Hawkes RC, Patz S. Rapid Fourier imaging using steady-state free precession. *Magn Reson Med* 1987; 4:9-23.

Henkelman, RM. Measurement of signal intensities bin the presence of noise in MR images. *Med Phys* 1985; 12: 232-233.

Henkelman RM, Huang X, Xiang QS, Stanisz GJ, Swanson SD, Bronskill MJ. Quantitative interpretation of Magnetization transfer. *Magn Reson Med* 1993; 29, 759-66.

Henkelman RM, Hardy PA, Bishop JE, Poon CS, Plewes DB. Why fat is bright in RARE and fast spin-echo imaging. J Magn Reson Imaging. 1992; 2:533-40.

Henkelman, R.M., Stanisz, G.J., Graham, S.J. 2001. Magnetization transfer in MRI: a review. *NMR BioMed* 1993; 14, 57-64.

Henkelman RM, Stanisz GJ, Kim JK, Bronskill MJ. Anisotropy of NMR properties of tissues. *Magn Reson Med* 1994; 32:592-601.

Hennig J, Nauerth A, Friedburg H. RARE imaging: a fast imaging method for clinical MR. *Magn Reson Med* 1986; 3: 823-833.

Hennig J. Multiecho imaging sequences with low refocusing flip angles. *J Magn Reson* 1988; 78:397-407.

Hoult DI, Richards RE. The signal to noise ratio of the nuclear magnetic resonance experiment. *J Magn Reson* 1976, 24:71-85.

Hoult DI. Sensitivity and power deposition in a high-field imaging experiment. *J Magn Reson Imaging* 2000; 12: 46-67.

Hutton C, Bork A, Josephs O, Deichmann R, Ashburner J, Turner R. Image distortion correction in fMRI: A quantitative evaluation. *NeuroImage* 2002; 16 :217-40.

Jenkinson, M. Improved Unwarping of EPI Volumes using Regularised B_0 Maps In: *Proceedings of the Int. Conf. on Human Brain Mapping* (HBM), 2001.

Jenkinson, M. and Smith, S. M. A Global Optimisation Method for Robust Affine Registration of Brain Images. *Medical Image Analysis* 2001; 5: 143-156.

Jenkinson M, Bannister PR, Brady JM, Smith SM. Improved optimisation for the robust and accurate linear registration and motion correction of brain images. *NeuroImage* 2002; 17:825-841.

Jenkinson M. Fast, automated, N-dimensional phase-unwrapping algorithm. *Magn Reson Med* 2003; 49: 193-7.

Jezzard P, Balaban RS. Correction for geometric distortion in echo planar images from B0 field variations. *Magn Reson Med* 1995; 34:65-73.

Jezzard P, Clare S. Sources of distortion in functional MRI data. *Hum Brain Mapp* 1999; 8: 80-5.

Jezzard P, Ramsey NF. Functional MRI. In: Tofts P, editor. *Quantitative MRI of the brain.* John Wiley and Sons, Ltd, 2003:414-53.

Jones DK, Horsfield MA, Simmons A. optimal strategies for measuring diffusion in anisotropic systems by magnetic resonance imaging. Mag*n Reson Med* 1999; 42: 515-25.

Jones DK, Pierpaoli C. Confidence mapping in diffusion tensor magnetic resonance imaging tractography using a bootstrap approach. *Magn Reson Med* 2005; 53: 1143-9.

Jones JA. Optimal sampling strategies for the measurement of relaxation times in proteins. *J Magn Reson* 1997; 126: 283-286.

Kadah YM, Hu X. Simulated phase evolution rewinding (SPHERE): a technique for reducing B0 inhomogeneity effects in MR images. *Magn Reson Med* 1997; 38:615-27.

Kay SM. *Fundamentals of statistical signal processing: estimation theory.* Englewood Cliffs, NJ: Prentice Hall. 1993.

Kennan RP, Zhong J, Gore JC. Intravascular susceptibility contrast mechanisms in tissues. *Magn Reson Med* 1994; 31: 9-21.

Koenigh SH. Cholesterol of myelin is the determinant of gray-white contrast in MRI of brain. *Magn Reson Med* 1991; 20: 285-91.

Koenig SH, Brown RD 3rd, Spiller M, Lundbom N. Relaxometry of brain: why white matter appears bright in MRI. *Magn Reson Med* 1990; 14: 482-95.

Kucharczyk W, Crawley AP, Kelly WM, Henkelman RM. Effect of multislice interference on image contrast in T2- and T1-weighted MR images. *Am J Neuroradiol* 1988; 9: 443–451.

Kucharczyk W, Macdonald PM, Stanisz GJ, Henkelman RM. Relaxivity and magnetization transfer of white matter lipids at MR imaging: importance of cerebrosides and pH. *Radiology* 1994;192:521-9.

Kwong KK, Belliveau JW, Chesler DA, Goldberg IE, Weisskoff RM, Poncelet BP, Kennedy DN, Hoppel BE, Cohen MS, Turner R, et al. Dynamic magnetic resonance

imaging of human brain activity during primary sensory stimulation. *Proc Natl Acad Sci U S A* 1992; 89: 5675-9.

Lattin J, Douglas Carroll JD, Green PE. Chapter 4 – Principal Component Analysis. *Analyzing multivariate data.* Thomson Learning 2003.

Lauterbur PC. Magnetic resonance zeugmatography. *Pure Appl Chem* 1974; 40: 149-157.

Le Bihan D, Breton E, Lallemand D, Grenier P, Cabanis E, Laval-Jeanet M . MR imaging of intra-voxel incoherent motions: application to diffusion and perfusion in neurologic disorders. *Radiology* 1986; 161: 401-407.

Le Bihan D. Diffusion, perfusion and functional magnetic resonance. *J Mal Vasc* 1995; 20: 203-214.

Le Bihan D, Mangin JF, Poupon C, Clark CA, Pappata S, Molko N, Chabriat H. Diffusion tensor imaging: concepts and applications. *J Magn Reson Imaging* 2001; 13: 534-46.

Li JG, Graham SJ, Henkelman RM. A flexible Magnetization transfer line shape derived from tissue experimental data. *Mag Reson Med* 1997 37, 866-871.

Mansfield P. Multiplanar image formation using NMR spin echoes. *J Phys C* 1997; 10: L55-L58.

Mori S, Crain BJ, Chacko VP, van Zijl PC. Three-dimensional tracking of axonal projections in the brain by magnetic resonance imaging. *Ann Neurol* 1999; **45**: 265–269.

Nedjati-Gilani S, Cook PA, Parker GJM, Alexander DC. Voxel-based classification of white matter fibre complexity in diffusion MRI. In: *Proceedings of Medical Image Understanding and Analysis*, 2005, Bristol, England, UK; p. 199-202.

Niendorf T. On the application of susceptibility-weighted ultra-fast low-angle RARE experiments in functional MR imaging. *Magn Reson Med* 1999; 41: 1189-98.

Norris DG. Ultrafast low-angle RARE: U-FLARE. *Magn Reson Med* 1991; 17: 539-42.

Norris DG, Börnert P. Coherence and interference in ultrafast RARE experiments. *J Magn Reson A* 1993; 105: 123-127.

Ogawa S, Lee TM, Nayak AS, GlynnP. Oxygenation-sensitive contrast in magnetic resonance image of rodent brain at high magnetic fields. *Magn Reson Med* 1990; 14: 68-78.

Parker GJ, Stephan KE, Barker GJ, Rowe JB, MacManus DG, Wheeler-Kingshott CA, Ciccarelli O, Passingham RE, Spinks RL, Lemon RN, Turner R. Initial demonstration of in vivo tracing of axonal projections in the macaque brain and comparison with the human brain using diffusion tensor imaging and fast marching tractography. *NeuroImage* 2002; 15: 797-809.

Parker GJ, Haroon HA, Wheeler-Kingshott CA. A framework for a streamline-based probabilistic index of connectivity (PICo) using a structural interpretation of MRI diffusion measurements. *J Magn Reson Imaging* 2003; 18: 242-54.

Parker GJ, Alexander DC. Probabilistic anatomical connectivity derived from the microscopic persistent angular structure of cerebral tissue. *Philos Trans R Soc Lond B Biol Sci 2005*; 360: 893-902.

Pauling L, Coryell C. The magnetic properties and structure of hemoglobin, oxyhemoglobin and carbon monoxyhemoglobin. *Proc Natl Acad Sci* USA 1936; 22:210-271.

Pierpaoli C, Basser PJ. Toward a quantitative assessment of diffusion anisotropy. *Magn Reson Med* 1996; 36:893-906.

Pikar J, Jezzard P, Roberts DA, Leigh JS, Frank JF, McLaughlin AC. Perfusion imaging with compensation for asymmetric magnetization transfer effects. *Magn Reson Med* 1996; 35: 70-79.

Pike GB. Pulsed magnetization transfer contrast in gradient echo imaging: a two-pool analytic description of signal response. *Mag Reson Med* 1996; 36: 95-103.

Pineda AR, Reeder SB, Wen Z, Pelc NJ. Cramer-Rao bounds for three-point decomposition of water and fat. *Magn Reson Med* 2005; 54: 625-635.

Portnoy S, Stanisz GJ. Quantitative measure of Magnetization transfer. In: *Proceedings of 13th ISMRM Scientific Meeting and Exhibition*, Miami, Florida, 2005, p 2219.

Press WH, Teukolsky SA, Vettering WT, Flannery BP. Minimization or maximization of functions. *Numerical Recipes in C*. Cambridge University Press, 1992.

Press WH, Teukolsky SA, Vettering WT, Flannery BP. Modeling of data. *Numerical Recipes in C*. Cambridge University Press, 1992.

Purcell EM, Torrey HC, Pound RV. Resonance absorption by nuclear magnetic moments in a solid. *Phys Rev* 1946; 69:37-38.

Ramani A, Dalton C, Miller DH, Tofts PS, Barker GJ. Precise estimate of fundamental in-vivo MT parameters in human brain in clinically feasible times. *Magn Reson Imaging* 2002; 20, 721-731.

Reber PJ, Wong PJ, Buxton RB, Frank LR. Correction of off resonance-related distortion in echo-planar imaging using EPI-based field maps. *Magn Reson Med* 1998; 39:328-330.

Reichenbach JR, Venkatesan R, Yablonskiy DA, Thompson MR, Lai S, Haacke EM. Theory and application of static field inhomogeneity effects in gradient-echo imaging. *J Magn Reson Imaging* 1997;7:266-79.

Robson MD, Gore JC, Constable RT. Measurement of the point spread function in MRI using constant time imaging. *Magn Reson Med* 1997; 38:733-40.

Ropele S, Filippi M, Valsasina P, Korteweg T, Barkhof F, Tofts PS, Samson R, Miller DH, Fazekas F. Assessment and correction of B1-induced errors in magnetization transfer ratio measurements. *Magn Reson Med* 2005;53:134-40.

Rosen BR, Belliveau JW, Aronen HJ, Kennedy D, Buchbinder BR, Fischman A, Gruber M, Glas J, Weisskoff RM, Cohen MS, et al. Susceptibility contrast imaging of cerebral blood volume: human experience. *Magn Reson Med* 1991; 22: 293-9.

Rossman K. Point-spread function, line-spread function, and modulation-transfer function: tools for the study of imaging systems. *Radiology* 1969; 93: 257-72.

Rugg-Gunn FJ, Eriksson SH, Boulby PA, Symms MR, Barker GJ, Duncan JS. Magnetization transfer imaging in focal epilepsy. *Neurology* 2003; 60,1638-1645.

Samson RS, Symms MR, Tofts PS. Optimisation of qMT sequence acquisition parameters. In: *Proceedings of the ESMRMB*, 2005, Basel, Switzerland, n. 417

Schaefer PW. Applications of DWI in clinical neurology. *J Neurol Sci* 2001; 186 Suppl 1: S25-35.

Schmitt F, Stehling MK, Turner R, *Eds. Echo-planar imaging: theory, technique and applications*. Springer; Berlin; 1998.

Silver NC. Magnetization Transfer Imaging to investigate Tissue Structure and optimize Detection of Blood Brain Barrier Leakage in Multiple Sclerosis. *PhD Thesis*, UCL, 2001.

Sled JG, Levesque I, Santos AC, Francis SJ, Narayanan S, Brass SD, Arnold DL, Pike GB. Regional variations in normal brain shown by quantitative Magnetization transfer imaging. *Magn Reson Med* 2004; 51, 299-303.

Sled JG, Pike GB. Quantitative interpretation of magnetization transfer in spoiled gradient echo MRI sequences. *J Magn Reson.* 2000; 145:24-36.

Sled JG, Pike GB. Quantitative imaging of Magnetization transfer exchange and relaxation properties in vivo using MRI. *Magn Reson Med* 2001; 46, 923-31.

Slichter CP. *Principles of magnetic resonance.* Spinger Verlag, III ed., New York, 1990.

Smith SM. Fast robust automated brain extraction. *Hum Brain Mapp* 2002; 17:143-155.

Stables LA, Kennan RP, Gore JC. Asymmetric spin-echo imaging of magnetically inhomogeneous systems: theory, experiment, and numerical studies. *Magn Reson Med* 1998; 40: 432-42.

Stanisz GJ, Odrobina EE, Pun J, Escaravage M, Graham SJ, Bronskill MJ, Henkelman RM. T1, T2 Relaxation and magnetization transfer in tissue at 3.0 T. *Magn Reson Med* 2005; 54: 507-512.

Stejskal EO, Tanner JE. Spin diffusion measurements: spin-echo in the presence of a time dependent field gradient. *J Chem Phys* 1965; 42: 288-292.

Stollberger R, Wach P. Imaging of the active B1 field in vivo. *Magn Reson Med* 1996; 35: 246-251.

Sundgren PC, Dong Q, Gomez-Hassan D, Mukherji SK, Maly P, Welsh R. Diffusion tensor imaging of the brain: review of clinical applications. *Neuroradiology* 2004; 46: 339-50.

Sutherland RJ, Hutchinson JMS. Three-dimensional NMR imaging using selective excitation. *J Phys E, Sci Instrum* 1978; 11: 79-83.

Symms MR, Boulby PA, Barker GJ. Cross-modality registration: validation and application in Magnetisation transfer imaging. In: *Proceedings of the 11th Scientific Meeting and Exhibition of ISMRM*, 2003, Toronto, Canada, p. 1050.

Symms MR, Barker GJ, Franconi F, Clark CA. Correction of eddy-current distortions in diffusion-weighted echo-planar images with a two-dimensional registration technique. In: *Proceedings of the 5th Scientific Meeting and Exhibition of ISMRM*, 1997, Vancouver, Canada, p. 1723.

Tanabe JL, Vermathen M, Miller R, Gelinas D, Weiner MW, Rooney WD. Reduced MTR in the corticospinal tract and normal T2 in amyotrophic lateral sclerosis. *Magn Reson Imaging* 1998;16: 1163-9.

Torrey HC. Bloch equations with diffusion terms. *Phys Rev* 1956; 563-565.

Tozer D, Ramani A, Barker GJ, Davies GR, Miller DH, Tofts PS. Quantitative Magnetization transfer mapping of bound protons in multiple sclerosis. *Magn Reson Med* 2003; 50, 83-91.

Tuch DS, Reese TG, Wiegell MR, Makris N, Belliveau JW, Wedeen VJ. High angular resolution diffusion imaging reveals intravoxel white matter fiber heterogeneity. *Magn Reson Med* 2002; **48**: 577–582.

Turner R, Le Bihan D, Moonen CT, desPres D, Frank J. Echo-planar time course MRI of cat brain oxygenation changes. *Magn Reson Med* 1991; 22:159-166.

Venkatesan R, Lin W, Haacke EM. Accurate determination of spin-density and T1 in the presence of RF-field inhomogeneities and flip-angle miscalibration. *Magn Reson Med* 1998; 40: 592–602.

Xing D, Papadakis NG, Huang CL, Lee VM, Carpenter TA, Hall LD. Optimised diffusion-weighting for measurement of apparent diffusion coefficient (ADC) in human brain. *Magn Reson Imaging*. 1997;15:771-84.

Weeden VJ, Reese TG, Tuch DS, Weigel MR, Dou J-G, Weiskoff RM, Chessler D. Mapping fiber orientation spectra in cerebral white matter with Fourier Transform diffusion MRI. In: *Proceedings of the 8th Scientific Meeting and Exhibition of ISMRM*, 2000, Denver, Colorado, USA, p. 82.

Wheeler-Kingshott CAM, Boulby PA, Symms MR, Barker GJ. Optimised cardiac gating for high-resolution whole brain DTI on a standard scanner. In: *Proceedings of the 10th Scientific meeting and exhibition of ISMRM*, 2002,Honolulu, Hawai'I, USA, p. 1118.

Whittall KP, MacKay AL, Graeb DA, Nugent RA, Li DK, Paty DW. In vivo measurement of T2 distributions and water contents in normal human brain. *Magn Reson Med* 1997; 37:34-43.

Wolff SD, Balaban RS. Magnetization transfer contrast (MTC) and tissue water proton relaxation *in vivo*. *Magn Reson Med* 1989; 10: 135-144.

Woods RP, Grafton ST, Watson JD, Sicotte NL, Mazziotta JC. Automated image registration: I. General methods and intrasubject, intramodality validation. *J Comput Assist Tomogr* 1998; 22, 139-152.

Worsley KJ, Evans AC, Marrett S, Neelin P. A three-dimensional statistical analysis for CBF activation studies in human brain. *J Cereb Blood Flow Metab* 1992; 12: 900-18.

Worsley KJ, Marret S, Neelin P, Vandal AC, Friston KJ, Evans AC. A unified statistical approach for determining significant signal in images of cerebral activation. *Hum Brain Mapp* 1996; 4: 58-73.

Yablonskiy DA, Haacke EM. Theory of NMR signal behavior in magnetically inhomogeneous tissues: the static dephasing regime. *Magn Reson Med* 1994 32:749-63.

Yarnykh VL. Pulsed Z-spectroscopic imaging of cross-relaxation parameters in tissues for human MRI: theory and clinical applications. *Magn Reson Med* 2002; 47:929-39.

Yarnykh VL , Yuan C. Cross-relaxation imaging reveals detailed anatomy of white matter fiber tracts in the human brain. *NeuroImage* 2004; 23:409-24.

Zur Y, Stokar S. A phase-cycling technique for cancelling spurious echoes in NMR imaging. *J Magn Reson* 1987; 71: 212-228.